NTNU – Trondheim
Norwegian University of
Science and Technology

Silicon for silicon nitride based products

Erik Riber Hem

Materials Science and Engineering
Submission date: July 2014
Supervisor: Kjell Wiik, IMTE
Co-supervisor: Johan Päääho Svanem, Elkem Silicon Materials

Norwegian University of Science and Technology
Department of Materials Science and Engineering

Preface

The work of this master thesis has been conducted at the Department of Material Science and Engineering at the Norwegian University of Science and Technology (NTNU) in collaboration with Elkem Silicon Materials and carried out during the spring of 2014. This report presents the suggested growth mechanisms during nitridation of silicon powders of different qualities.

The results in this report has been gathered independently, honestly and in accordance with NTNU regulations.

Trondheim, June 29th 2013

Erik R Hem

Acknowledgements

First and foremost I would like to thank my supervisor prof. Kjell Wiik for always having his door open and giving constructive feedback to my questions and results over the year. The weekly meetings were a great help. I am also really grateful for his advices putting this report together.

Many thanks to Elkem's representative Johan P. Svanem for good feedback on my results and suggestions to improvements and further work.

Thanks also the various people who have given me HSE instructions, training to use different apparatuses and miscellaneous assistances. This include TGA by Eli-Beate Larsen, XRD, EDS and SEM by Julian Tolchard, Yingda Yu for providing FEG-SEM pictures and Marisa Di Sabatino Lundberg for help with interpreting the results.

Abstract

Previous studies have investigated the effect of the oxide layer (Øvregård 2013) and iron content (Hem 2013) on the nitridation of silicon powders. This report will take a closer look into the growth mechanisms of different parameter such as storage conditions, particle size and impurities under different stages of the process.

The main focus was between two samples; Sample B and sample C. Names were given based on a system of purity, worked out by Hem 2013. In short; Sample B has low amount of impurity, while Sample C has higher amount of impurity. Both of these samples have grain sizes of 0.2-0.8mm.

The growth mechanisms change during the nitridation of silicon, depending on temperature and amount of impurity; Sample B forms cavities on the surface before the growth of wool-like, dense, whiskers. Sample C forms the whiskers before cavities. The wool-like whiskers originates from droplets of molten $FeSi_2$ and forms α-Si_3N_4 whiskers, by a VLS process, which are later retarded and thickened by condensation of SiO_2(s). At higher temperatures the whole surface of both samples is covered in β-Si_3N_4 dendrites with trench like cavities to each side, which form by surface diffusion and evaporation of Si to the reaction sites. The nature of the whiskers change in the C sample at elevated temperatures to longer and straighter whiskers, due to the VLS process is moved away from the surface to the $FeSi_2$ beads at the whiskers' terminus. This change is almost not noted in the B sample.

Due to the geometry of the crucible the surface of the sample is soon covered in a cloud of SiO_2(s) condensed on the crucible wall. This phenomenon occurs in all samples, and may hinder the nitrogen gas flow to reach the sample surface. This explains the very low amounts of α-Si_3N_4 but high amounts of cristobalite detected.

Humid storage condition was tested on a pure and fine grained (<75 μm) sample named A and showed that the growth of the protective silica layer retards the nitridation process. The fine grained sample A also beat the coarse grained sample B and C in the amount Si converted, proving how important the grain size is for the nitridation process.

The role of impurities were discovered; Iron catalyses the growth of α-whiskers, aluminum oxidizes and preventing the reestablishment of the protective silica layer and copper acts as a catalyst at very low temperatures. Calcium quantities are too low to give any conclusion.

Sammendrag

Tidligere studier har undersøkt virkningen av oksidlag (Øvregård 2013) og jerninnhold (Hem 2013) på nitrideringen av silisiumpulver. Denne rapporten vil ta en nærmere titt på vekstmekanismene av forskjellige parametre som lagringsforhold, partikkelstørrelse og urenheter under forskjellige stadier av prosessen

Hovedfokuset var mellom to prøver; Prøve B og prøve C. Navn ble gitt basert på et system av renheter, utviklet av Hem 2013. Kort fortalt; Prøve B har mindre mengde urenheter, mens prøve C har større mengde urenheter. Begge disse prøvene har kornstørrelse 0.2-0.8mm.

Vekstmekanismene forandres under nitrideringen av silisium, avhengig av temperature of mengde urenheter; Prøve B danner groper på overflaten før vekst av ullignende, tette, whiskers. Prøve C danner whiskers før groper. De ullignende whiskerne oppstår fra mindre dråper av smeltet $FeSi_2$ og danner α-Si_3N_4 whiskers, ved en VLS prosess, som senere blir forhindred og fortykket ved kondensering av SiO_2(s). Ved høyere temperaturer er hele overflaten av begge prøvene dekket av β-Si_3N_4 dendriter med groper på begge sider, som dannes av overflate diffusion of avdamping av Si til reacsjonspunktene. Opphavet til whiskerne forandres i prøve C ved høyere temperaturer til lengre og rettere whiskers, på grunn av VLS prosessen er flyttet fra overflaten til $FeSi_2$ perler på endene til whiskerne. Denne forandringen er nesten ikke merkbar i prøve B.

På grunn av geometrien til digelen så blir overflaten til prøven snarlig dekket av en sky med SiO_2(s) som kondenserer på digelveggen. Dette fenomene opptrer på alle prøvene, og kan forhindre strømmen av nitrogengass til å nå prøveoverflaten. Dette forklarer den veldig lave målingen av α-Si_3N_4 men høye målingen av cristobalite.

Fuktig lagringsforhold ble testen på en ren og finkornet (<75 µm) prøve navngitt A og viste at veksten av det beskyttende silikalaget forhindrer nitrideringsprosessen. Den finkornede prøven A slo også de grovkornede prøvene B og C i mengde omgjort Si, og beviste hvor viktig kornstørrelsen er for nitrideringsprocessen.

Rollen til urenhetene ble oppdaget; Jern catalyserer veksten av α-whiskers, aluminium oksideres og forhindrer gjendannelsen av det beskyttende silikalaget og kobber fungerer som en katalysator ved lavere temperatrer. Kalsium mengdene er for lave til å gi en konklusjon.

Table of contents

PREFACE .... **I**

ACKNOWLEDGEMENTS .... **II**

ABSTRACT .... **III**

SAMMENDRAG .... **IV**

TABLE OF CONTENTS .... **V**

ABBREVIATIONS AND DEFINITIONS .... **VII**

1 INTRODUCTION **1**

1.1 BACKGROUND 1
1.2 AIM 4

2 THEORY **5**

2.1 THE DIFFERENCE BETWEEN A AND B PHASE 5
2.2 FORMATION OF SILICON NITRIDE 8
2.3 MORPHOLOGIES AND GROWTH MECHANISMS 11
2.3.1 Alpha whiskers *12*
2.3.2 Alpha matte *13*
2.3.3 Beta phase *14*
2.3.4 SiO_2 .... *15*
2.4 DIFFUSION 16
2.4.1 Silicon nitride layer *16*
2.4.2 Bulk *17*
2.5 PARTIAL PRESSURES AND THE ROLE OF SIO 18
2.5.1 The Si-O-N system *18*
2.5.2 List of partial pressures at 1330°C *21*
2.6 THE FUNCTION OF IMPURITIES 22
2.6.1 Iron *22*
2.6.2 Aluminium *25*
2.6.3 Calcium *25*
2.6.5 Copper *25*
2.6.6 Inter-metallic etching effect *26*

3 EXPERIMENTAL **27**

3.1 APPARATUS AND SAMPLES 27
3.1.1 Thermogravimetric analysis *27*
3.1.2 XRD *27*
3.1.3 SEM and EDS *27*
3.1.4 Samples *27*
3.2 PROCEDURE 29
3.2.1 Thermogravimetric analysis *29*
3.2.2 XRD *33*
3.2.3 SEM and EDS *33*

4 RESULTS **35**

4.1 TGA 35
4.1.1 Humid storage conditions *35*
4.1.2 Cu-added sample *36*

4.1.3 Coarse B and C *37*
4.1.4 Summary *39*
4.2 OBSERVATIONS OF THE CRUCIBLE AFTER NITRIDATION 40
4.3 SEM 41
4.3.1 Sample B *41*
4.3.2 Sample C *42*
4.3.3 Comparing B and C *43*
4.3.4 Chosen cross section images *47*
4.3.5 Summary *49*
4.4 BSE IMAGES AND EDS 50
4.4.1 Selected images *50*
4.4.2 Summary *52*
4.5 XRD 53
4.5.1 XRD plot sample B3 with and without the top layer *53*
4.5.2 XRD plot stage 2 and 3 ..... *54*
4.5.3 XRD plot Cu Hi and D *55*
4.5.4 Summary *56*
4.6 SPECIAL CASE 57
4.6.1 Silica free exposed surface *57*
4.6.2 Highly magnified morphologies *58*

5 DISCUSSION 59

5.1 DETERMINING THE STRUCTURES 61
5.3 COMPARING SAMPLES 64
5.3 REGARDING GRAIN SIZES 65
5.4 ROLE OF STORAGE CONDITIONS 65
5.5 ROLE OF ADDITIVES AND IMPURITIES 66

6 CONCLUSION 67

7 FURTHER WORK 69

REFERENCES 70

APPENDIX I

A VAPOR PRESSURE I
B ELLINGHAM DIAGRAMS III
C XRD PLOTS V
D EXCHANGE PURE NITROGEN GAS FLOW WITH ARGON X
E ADDITIONAL DATA XII

Abbreviations and definitions

- BSE - Back-Scattered Electrons
- CVD - Chemical Vapor Deposition (process)
- DTA - Differential Thermal Analysis
- EDS - Energy-Dispersive Spectroscopy
- HIP - Hot Isostatic Pressing
- RSBN - Reaction Bonded Silicon Nitride
- SE - Secondary Electrons
- SEM - Scanning Electron Microscopy
- TGA - Thermogravimetric Analysis
- VLS - Vapor Liquid Solid (process)
- XRD - X-ray Diffraction

1 Introduction

1.1 Background

Two of the most abundant elements on Earth are silicon and nitrogen. By combining these two elements into silicon nitride, like Si_3N_4, one will get a high strength, low weight, material with excellent resistances to thermal shock and corrosive attack. However, natural occurring Si_3N_4 does not exist on earth, apart from very few meteorites that survives the travel through the atmosphere. The material must therefore be manufactured.

The first recording of mixing silicon and nitrogen to form Si_3N_4 was in 1859 by Deville and Wöhler [1], and in some years later a patent was filed regarding a production method of Si_3N_4 by reducing SiO_2 with carbon [2]. The atomic structure of this material was not determined and the earliest review of a 3:4 ratio silicon nitrogen was by Weiss and Engelhardt in 1910 [3]. The scientist at the time didn't see any particular use of Si_3N_4 compared to SiC, which was the hot topic of the time, and so the research on silicon nitride was kept at a minimum for many of the following years.

In the 1950s the research began to pick up again and as Si_3N_4 replaced other ceramics as refractory material in quick-heating and cooling processes. The importance of different additives were also investigated and iron proved to be the most interesting element as it worked as a catalyst and made it possible to form silicon nitride at lower temperatures and at higher yields [4]. The iron was mostly introduced during milling of the silica precursor. The mechanisms behind why iron worked so well was, however, not discovered until two decades later.

Extensive work began in the 1960s on the topics of high temperature engine materials such as combustion engines, but especially rockets (together with the idea of atomic-energy jets), and Si_3N_4 showed good potentials against thermal shock. As a result, few other (structural) ceramic materials have been so thoroughly studied in regard to the production technology and the science behind the transformation mechanisms. Among the important discoveries were the α and β phases which have slightly different properties due to different structures and morphology [5]. There are multiple reaction mechanisms in forming both α and β, and the former into the latter [6], and by selective mixing the two phases it is possible to alter the properties of the final product, in regard to strength, thermal conductivity and porosity. This can be achieved by e.g. additives such as iron, as shown by Hem (2013, [7]) in figure 1.1 and 1.2; the amount of converted silicon increases and the α:β ratio changes with different iron content. The mechanisms behind this will be discussed in more detail later in this report.

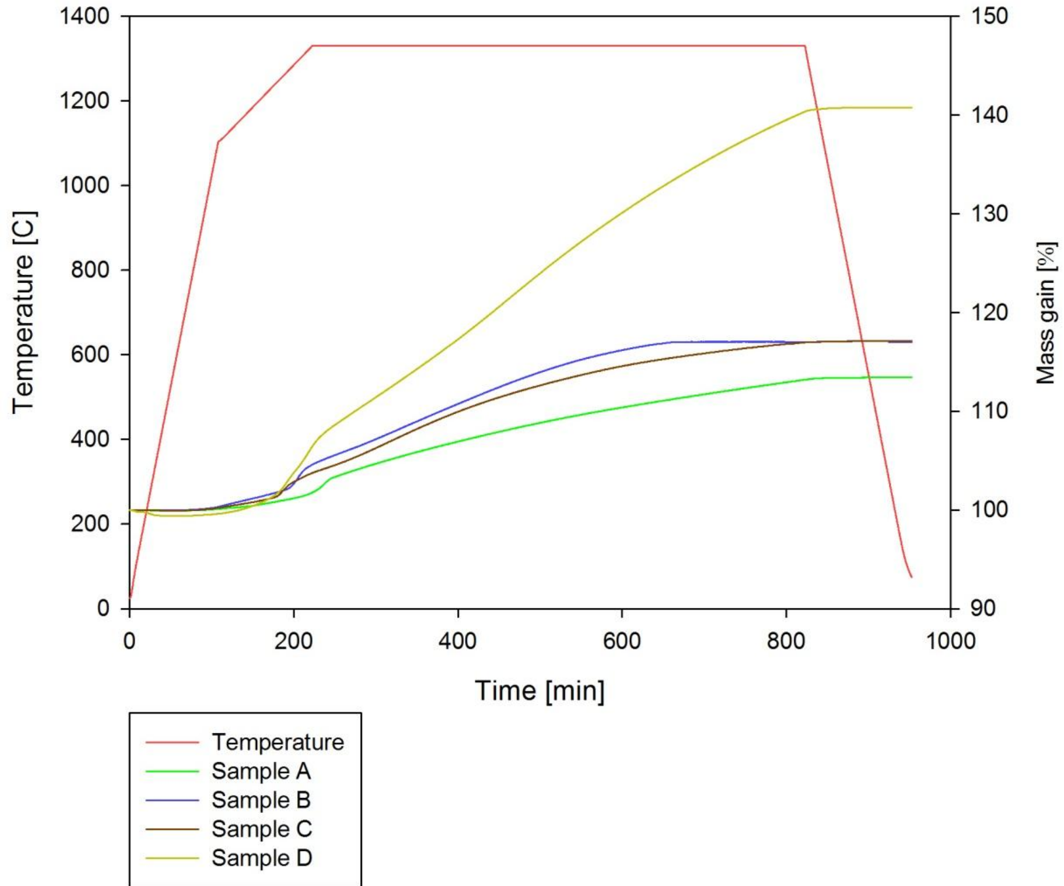

Figure 1.1: TGA plot, made my Hem [7], showing mass gain of four different samples during nitridation in pure nitrogen atmosphere, from A (< 20 ppm iron) to D (ca 7100 ppm iron). The iron content changes mass gained.

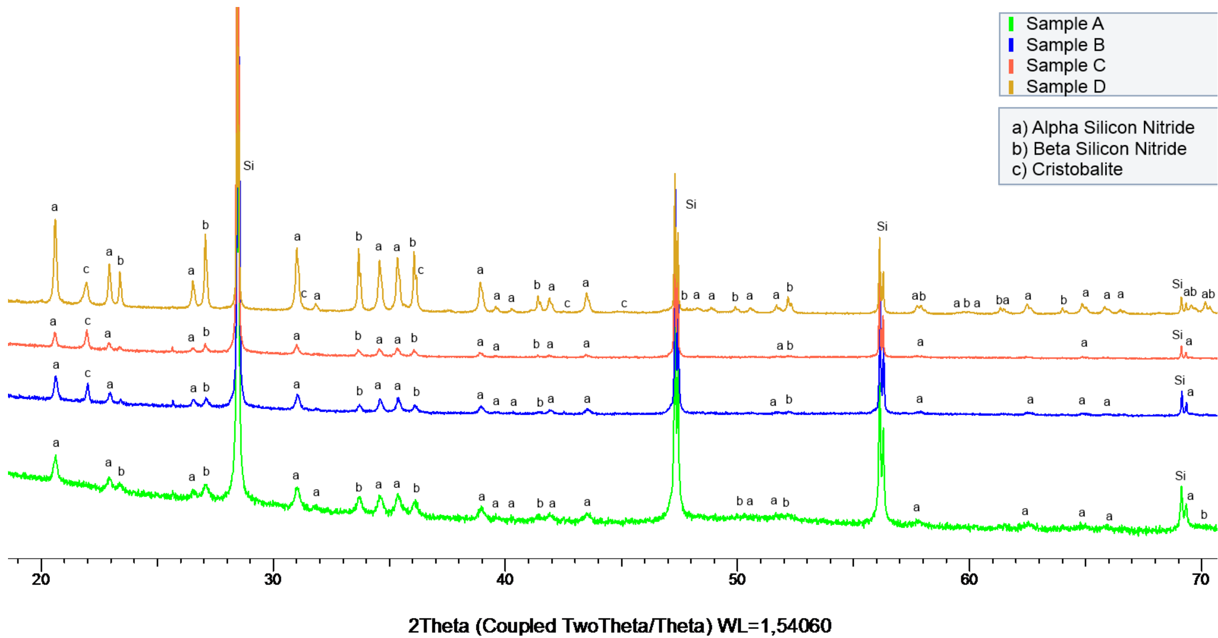

Figure 1.2: XRD plot, made by Hem [7], showing phase composition of four samples with increasing amount of iron content, from <20 ppm (A) to 7100 ppm (D). The iron content changes α:β ratio.

Other discoveries done during the 1960s were dense bodies using hot isostatic pressing (HIP) with e.g. MgO as a sintering aid, and a new production method, which was later named reaction bonded silicon nitride (RBSN) and involves nitridation of powder or compact silicon in N_2 atmosphere [5].

In the wake of the rediscovery of silicon nitride Moulson et al. [8,9,10,11,12,13] investigated deeper into the mechanisms behind silicon nitride forming by RBSN, and especially the function of adding iron. In a review article in 1979 [13] Moulson summarizes these discoveries and thereby creates a fundamental platform regarding Si_3N_4 which has been cited over 240 times [14]. Another important, and more recent, review article was made by Riley in 2000 [5], which has been cited more than 450 times [14]. It is therefore logical that both of these papers are used as a foundation in this report.

Later studies up to present day have been more focused on the Si-Al-O-N system and semiconductor industries i.e. the functional properties of silicon nitride, and not so much on the structural properties as these are by now fairly well established in the literature.

The discovery of RBSN made it easy to form complex shapes and made Si_3N_4 suitable for high temperature applications such as turbines and nozzles due to the high thermal conductivity and low thermal expansion combined with the strength in extreme environments, as well as an insulator, and etch masking due to high resistivity and high dielectric constant. Another important application is as cantilever in atomic force microscopes due to all the before mentioned properties.

Today Si_3N_4 is most commonly produced by RBSN [5]:

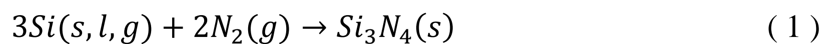

$$3Si(s,l,g) + 2N_2(g) \rightarrow Si_3N_4(s) \quad (1)$$

This method is carried out at temperatures around 1200-1450°C in nitrogenous atmospheres. A commonly used procedure is to slowly heat up to 1300°C and hold until the reaction almost comes to a complete stop, before increasing the temperature to 1450°C to achieve the highest conversion rates of silicon. With this setup the nitridation is related to heating rate and nitrogen uptake rate. The whole process is still quite time consuming (12-36h) [5].

Silicon nitride has been proven to perform well in numerous of various applications and might replace existing materials in different industries. However, the reason why Si_3N_4 is still not in high supply today, even though the raw material prices are low, is because of the high production costs. Keeping the temperature at 1450°C for many hours is not cheap, and to achieve the desired properties one cannot produce silicon nitride from large and dense silicon precursor, so there is an issue of mass production as well. The main obstacle is however the slow conversion rate, and further knowledge of the growth mechanisms are required in order to achieve more effective production methods.

1.2 Aim

In the present study the precursors will be metallic silicon with different purity and particle size, and the main objective will be to investigate how nitridation is affected by parameters such as:

- Oxide layer (SiO_2)
- Long term storage (dry vs. humid)
- Particle size
- Impurities and additives (Al, Fe, Ca, Ti and Cu)

A thermogravimetric analyzer (TGA) will be used to measure the mass changes during nitridation. This will give an indication regarding the different conversion rates between the samples, as the apparatus logs time, temperature and weight during the process, which is controlled by a temperature program. By allowing a long isothermal holding time, at nitriding conditions, the experimental setup will also give indications on the evolution of the nitridation from the beginning till the end of the program. The program will later be stopped at different stages in the process to investigate the propagation of silicon nitride from start to the given stage.

The nitridated samples will be studied further in scanning electron microscope (SEM) to determine the surface morphology, energy dispersive spectroscopy (EDS) to map the elements in the surface, and X-ray diffraction (XRD) to confirm what phases are represented in the sample.

2 Theory

2.1 The difference between α and β phase

Silicon nitride, Si_3N_4, exists in two major configurations: α and β. There is also a very rare γ-Si_3N_4, but this configuration is formed at very high pressure and temperature [15] and hence beyond the scope of this investigation.

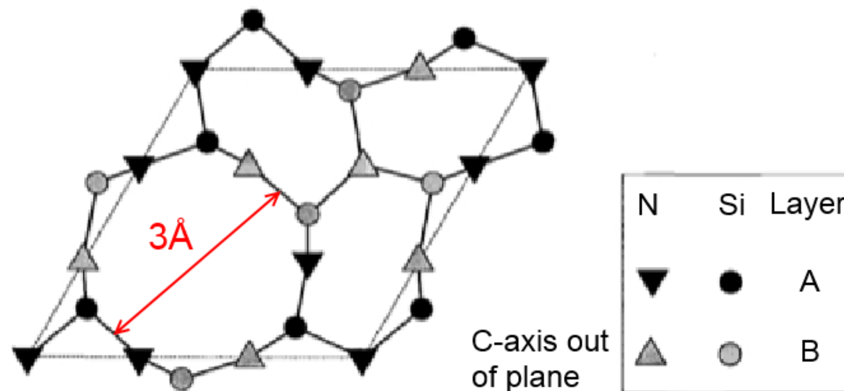

Figure 2.1: Basal plane of β-Si_3N_4 made up by two layers; A and B [16]. The channel's diameter: 3Å [5]. Density: 3.203 g/cm3 [17].

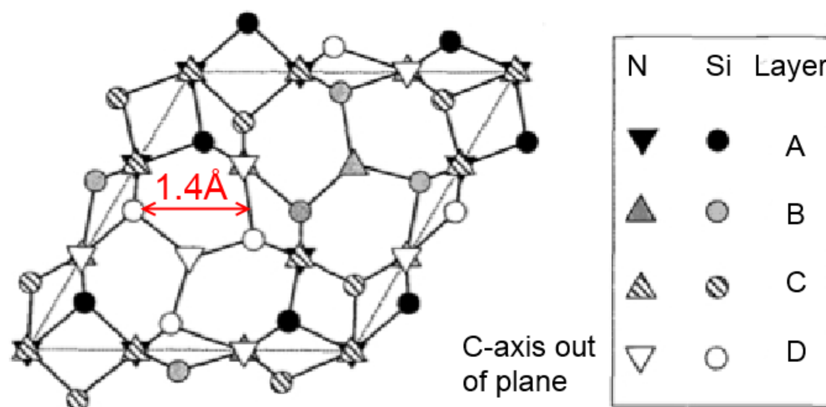

Figure 2.2: Basal plane of α-Si_3N_4 made up by four layers, where C and D is rotated 180° in relation to layer A and B [16]. Due to the rotation of C and D the channel's diameter is much smaller, 1.4Å [5], and the density is also lower; 3.149 g/cm3 [17].

Both α and β have hexagonal structure [18] based on phenacite; Be_2SiO_4 where the beryllium atoms are replaced with silicon and oxygen atoms are replaced by nitrogen. The bonding leads to slightly distorted Si_3N_4 tetrahedra joined together by corner sharing N. The stable β-structure then becomes an enclosed form with ABAB sequences, see Figure 2.1, with the space group $P6_3/m$ and a density of 3.203 g/cm^3. Pure silicon has a density of 2.33 g/cm^3 [19].

The terms “high and low oxygen potential” were previously used in regard to the α-structure as it was speculated that the structure also contained oxygen [20], but the consensus today is that α is a meta-stable form of non-oxygen Si_3N_4 with space group $P3_1c$ and the layer sequence ABCDABCD with a density of 3.149 g/cm^3. The CD layer in α is similar to the AB layer, but rotated 180° on the c-axis as seen in Figure 2.2 indicated by the rotated triangles. This means that the long continuous channels along the c-axis found in the β-structure are not present in the α-structure [21], making diffusion of e.g. nitrogen much slower though α-Si_3N_4 than β-Si_3N_4 [22].

For some time the theory was that the two structures formed by two different reaction mechanisms: chemical-vapor-deposition (α) and vapor-liquid-solid (β) [12]. Later studies suggested that this theory was too simple; it had no consistency with data in the literature [6]. Jennings [6] introduced the concept of atomic and molecular nitrogen as the missing parameter in the determination of whether α or β would be formed:

α-Si_3N_4: Silicon gas evaporates from the surface, or liquid phases, and reacts with nitrogen molecules and is considered to form sphere shaped crystals, called a matte, or whisker formations [13,23]. The sphere-growth is based on Ostwald ripening, where the larger grains increase in size at the cost of the smaller [24].

β-Si_3N_4: Nitrogen dissolves and dissociates into liquid silicon, or other liquid phases (e.g. $FeSi_2$), and then combines with silicon and forms rod shaped crystals or spikes [23,25] with preferred growth direction, due to ease of N diffusion, along the c-axis, seen in Figure 2.3. Increased partial pressure of nitrogen and higher temperature will favor β structure as the liquid phase is able to solve more nitrogen [26].

A comprehensive study of silicon nitride crystallography, kinetics and thermodynamics has been carried out by Myhre, 1989 [27]. He covered the topic of using pre-made α or β-Si_3N_4 powders in the Si precursor to influence the reaction towards the phase that was added before the nitridation process.. This technique is called seeding [6], and the need for clean crucibles is therefore important.

The β-structure is the stable structure at all temperatures, meaning it is possible to convert α to β, but never vice versa [27,28]. This will explain and confirm many observations reported in the literature [13,28,29,12] regarding why phase transition from α to β is possible, but never vice versa. This phase transition is observed during sintering and densification processes, i.e. at temperatures exceeding 1414°C, when the α-phase is in contact with liquid silicon phase, either pure silicon or an inter-metallic phase such as $FeSi_2$. The liquid dissolves the silicon nitride and it reacts with the solved atomic nitrogen to form β, as described above [6]. A liquid of metal oxide impurity might also act as the solvent of the α-phase at lower temperatures and transform α to β, if SiO_2 is present, while the liquid itself transforms into a glass phase [21]:

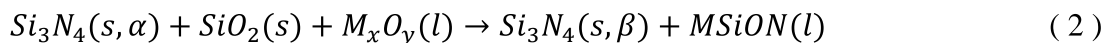

$$Si_3N_4(s,\alpha) + SiO_2(s) + M_xO_y(l) \rightarrow Si_3N_4(s,\beta) + MSiON(l) \quad (2)$$

It is therefore ideal to remove as much silica as possible prior to sintering and densification, as the glass phase severely weakens the strength of the material. Examples of oxide additives are binders for sintering purposes like MgO or Y_2O_3 + Al_2O_3 and other rare earth oxides to modify the microstructure. Other sources of oxides are impurities like Fe oxides.

One might still wish to separate α and β phases by CVD and VLS respectively, as there is a strong trend towards such separation (only traces of α by VLS and vice versa). Pure silicon is however not liquid below 1414°C, but if the temperature is high enough for silicon-inter-metallic compounds to form, like $FeSi_2$ (1212°C), then it is possible to achieve growth by VLS. More on this in the next section.

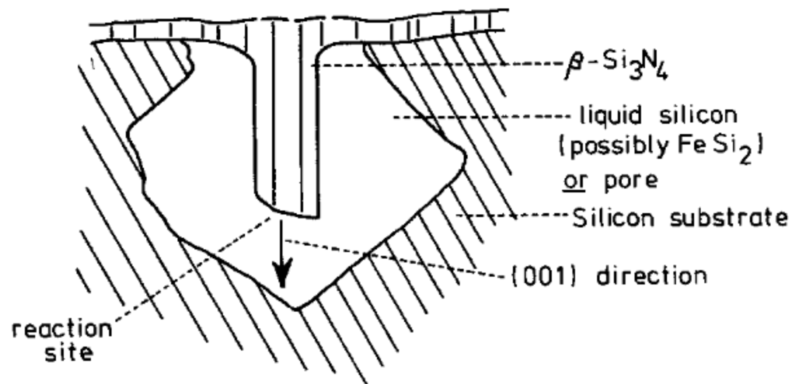

Figure 2.3: Illustrated β Si_3N_4 growth [6] into the open space of a pore.

The spike growth shown in Figure 2.3 might grow deeper into the silicon bulk and force the grain to crack due the stresses generated at the tip. Also note that nitrogen might diffuse down the from the surface, as the growth is in the 001 direction, c.f. Figure 2.1.

2.2 Formation of silicon nitride

The main reaction when forming RBSN is described in equation (1) in the introduction. Solid silicon is mixed with pure nitrogen gas and heated up to form silicon nitride. At elevated temperatures this can be done through solid, liquid and gaseous silicon [13]:

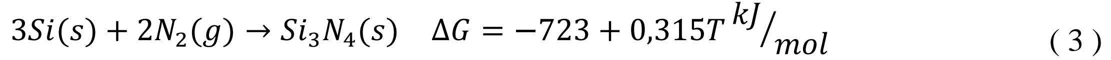

$$3Si(s) + 2N_2(g) \rightarrow Si_3N_4(s) \quad \Delta G = -723 + 0{,}315T \ {}^{kJ}/_{mol} \tag{3}$$

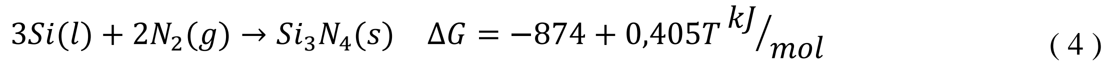

$$3Si(l) + 2N_2(g) \rightarrow Si_3N_4(s) \quad \Delta G = -874 + 0{,}405T \ {}^{kJ}/_{mol} \tag{4}$$

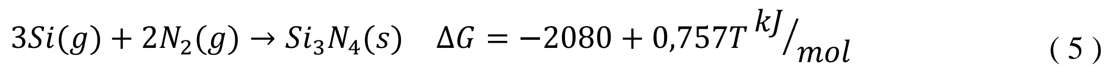

$$3Si(g) + 2N_2(g) \rightarrow Si_3N_4(s) \quad \Delta G = -2080 + 0{,}757T \ {}^{kJ}/_{mol} \tag{5}$$

The Gibbs free energy difference between α- and β- Si_3N_4 is very small and the formation of either one is more connected to the growth mechanism than the energy of formation, so the literature does not distinguish between the two phases [5,6]. From equations 3-5 the free energy of formation is plotted over the temperature range of RBSN in Figure 2.4:

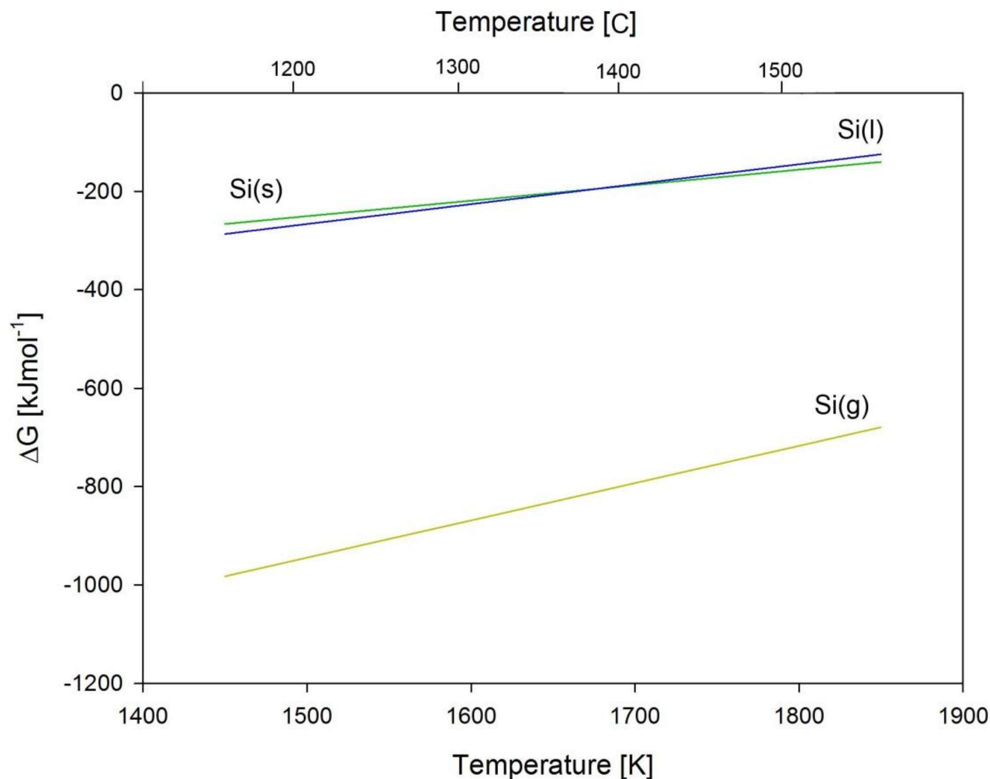

Figure 2.4: The Gibbs free energy of formation for RBSN based on equations 3-5.

From Figure 2.4 it is obvious that gaseous silicon is the highly preferred route to form silicon nitride.

The formation of silicon nitride proceeds through three distinct stages. First stage is nucleation and growth, which can be controlled by external parameters such as nitrogen partial pressure and temperature: High P_{N2} and low temperature favors high nuclei density because the reaction is highly exothermic (eq. 3-5). This is shown in Figure 2.6.A.

Assuming that the precursor consists of 100% silicon pure silicon, and even no silica layer. After the short initial period of nucleation and growth by direct nitridation (eq. 3), i.e. nitrogen adsorbs to the surface and reacts with silicon through CVD, the silicon surface will be covered by sites consisting of mostly α-Si_3N_4, which will grow is vertically, and mostly β-Si_3N_4 if the growth is horizontally [5,6,13], i.e. on the surface, seen in Figure 2.5. After these have been established on the surface, then the silicon has to migrate to the reaction sites by either surface diffusion or evaporation, and cavities start to appear since the silicon nitride grows into the gradient of nitrogen, illustrated in Figure 2.6.B and C.

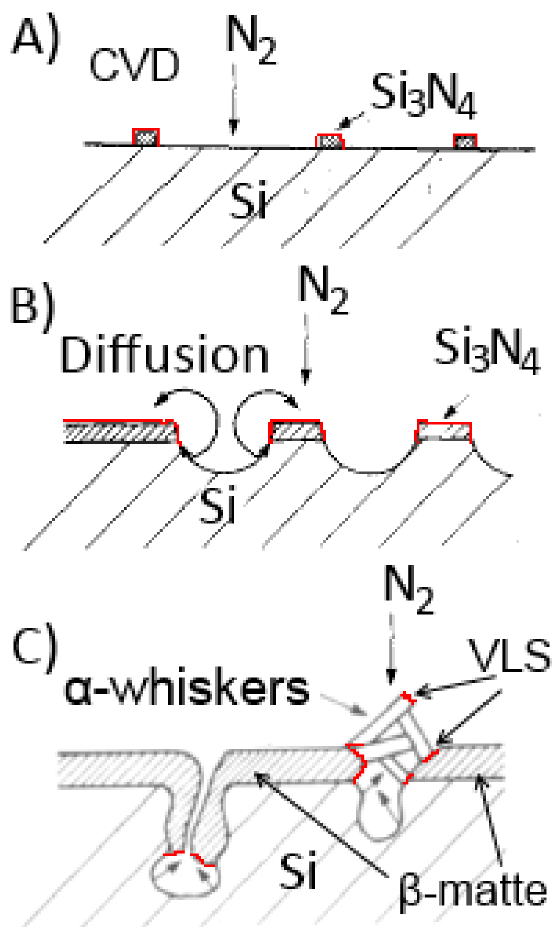

These cavities will eventually start to deepen, but leaving open channels, called chimneys, where gaseous silicon continues to migrate through and reacts with nitrogen through CVD (eq. 5). This gives rise to growth of the Si_3N_4-whiskers and the cavities now increase in size and forming pores, generating more exposed surfaces as the pores widen.

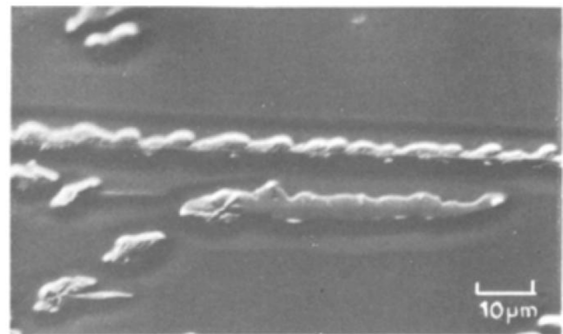

Figure 2.5: The growth of β-Si_3N_4 on the surface, as illustrated in Figure 2.6.B. Notice the cavities surrounding the strips of silicon nitride due to migration of silicon to reaction sites. Source: [13].

Figure 2.6**:** A) Formation of silicon nitride; vertical growth gives mostly α-phase, horizontal growth gives mostly β-phase. B) Nucleation and growth. C) Pore closing. The red spots marks reaction sites. Source: [13].

Further reaction of Si closes the pores to the surface, Figure 2.6.C, retarding the nitridation diffusion rates to a final stop as inter-diffusion through the Si_3N_4-layer is extremely slow, as shown in section 2.3. If the temperature is high enough, then there might be some liquid phase present to form β-Si_3N_4 crystals [13].

At elevated temperatures liquid phases will occur inside the pores. As explained in section 2.1 these pools play an important part in producing silicon nitride as they dissolve α-Si_3N_4 and solve both silicon and mono-atomic nitrogen, illustrated in Figure 2.7.A.

During the last stage of nitridation the α-phase may continue to grow, even though the thickness of the Si_3N_4-layer prevents diffusion, as the chimneys may still transport Si(g) [12]. These chimneys might also appear because of micro-cracks from the different thermal expansion coefficient between silicon nitrides, shown in Figure 2.7.B below. As β needs a liquid phase, which by this stage is capsule inside the pore [5], the formation of this structure stops new pools are generated on the surface. No further reactions occur after a complete separation of silicon from nitrogen.

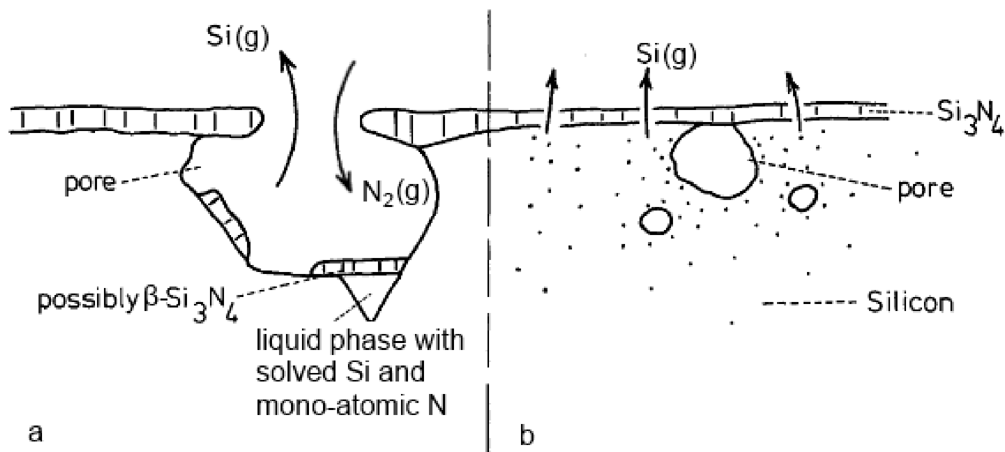

Figure 2.7: A sketch of how nitridation may occur inside cavities and pores (a); Evaporates of silicon gas diffuses out of the pore and form α-whiskers from CVD with nitrogen from the atmosphere, or inside the pore if the partial pressure of nitrogen is high enough. The liquid pool dissolves α-Si_3N_4 and solves silicon and mono-atomic nitrogen to form β-Si_3N_4. A closed pore (b); Silicon gas continues to migrate to the surface through chimneys and micro-cracks in the silicon nitride surface. Source: [6].

The volume expansion of the reaction is mostly inwards into cavities of the silicon crystal, as shown in Figure 2.3 and Figure 2.6.C. This means that the growth of silicon nitride depends on the size of the silicon grains [30], meaning that smaller grains with higher specific surface should achieve higher nucleation and growth and thereby higher conversion rates than larger grains, where the nitridation process stops before it penetrates the whole bulk. This is illustrated in Figure 2.8.

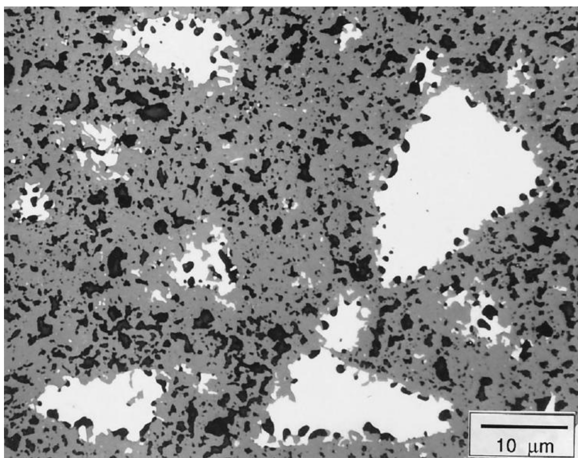

Figure 2.8: Larger grains have not fully converted the silicon (white) into silicon nitride (gray) as the cavities do not penetrate the whole bulk of the silicon grain. Source: [5].

2.3 Morphologies and growth mechanisms

Extensive work by Jennings and Richman [23] were conducted on formation mechanisms and kinetics of RBSN, including morphologies present at different parameters of the process. It is established in the literature that Si_3N_4 can be divided into three main microstructures; α-phase whiskers (formation containing many needles), α-phase matte (dense surface layer) and β-phase rods and spikes.

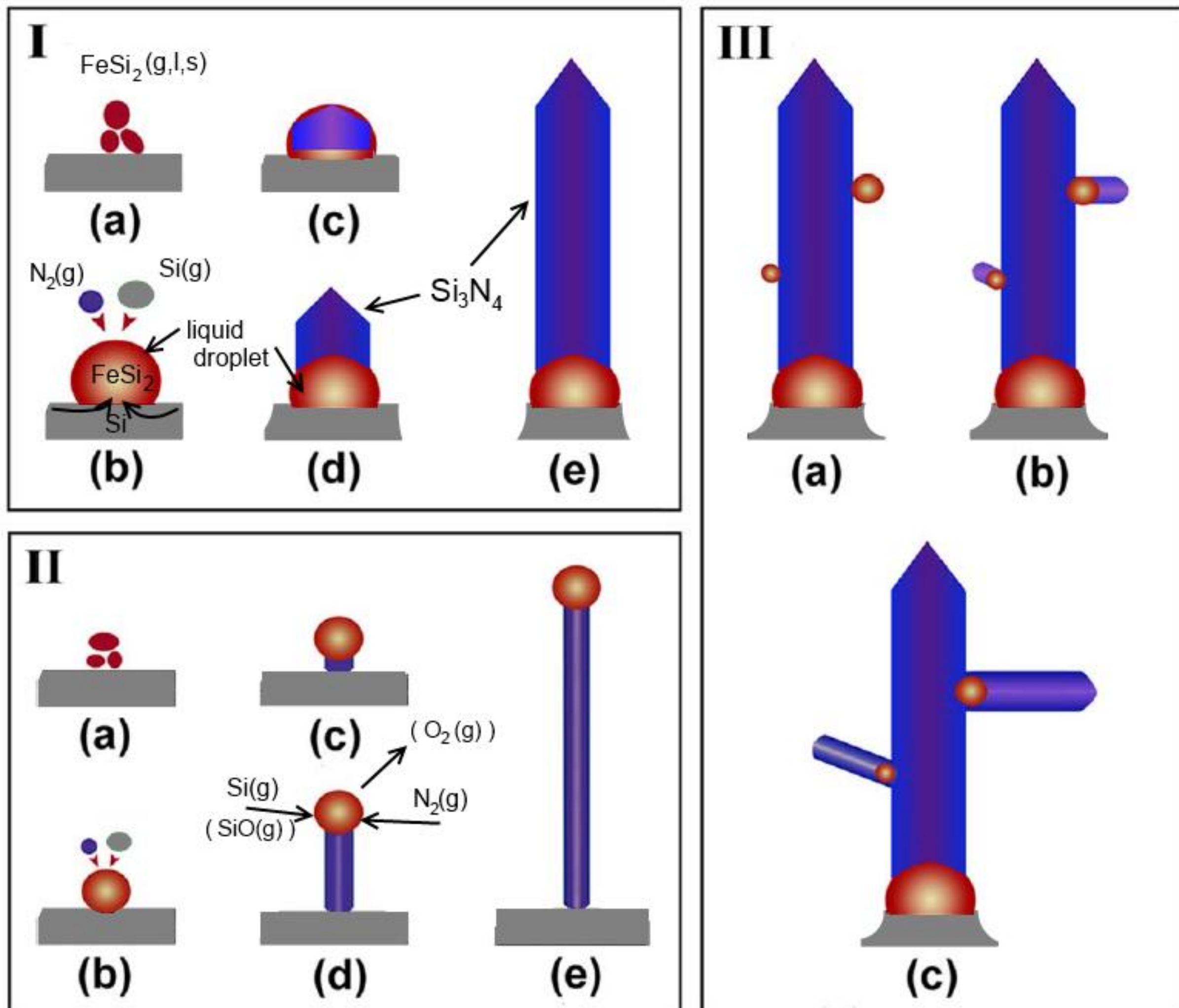

Figure 2.9: Three different growth mechanisms with VLS; I) Whisker growth from larger particle at the origin on the surface: a) Nucleation and melting of an inter-metallic phase with melting point below silicon (e.g. $FeSi_2$), called the seed. b) The diffusion of nitrogen gas and silicon (either as gas or solid) solves in the droplet. c) Nucleation of an α-needle. d-e) Growth of whisker by both VLS at the origin and VS (vapor solid) at the tip. II) Whisker growth from bead at the terminus: a-b) Same as for section I. c-e) VLS growth at the tip, meaning only gaseous reactants (Si(g) or SiO(g)); no direct supply of Si(s) from the surface. III) Branched growth: a) Catalytic materials condenses on the sides of a whisker and starts a new branch by VLS. Source: [31]

2.3.1 Alpha whiskers

This structure is the most common in silicon nitride products [13,23]. They are very thin, around 50-300 nm [23,31,32], and have a aspect ratio of >25. This structure is however not present in very pure silicon precursors [33]. In the case the silicon contains impurities, some of the needles have beads at the terminus, as shown in Figure 2.10, while others have larger particles at their origin. This indicates growth by VLS which is illustrated by Figure 2.9. Some of the needles in the whisker formation might only have a crystalline core and amorphous outer-layers [23,34], formed by CVD. Others might have crystalline silicon nitride walls, but liquid Si cores [35].

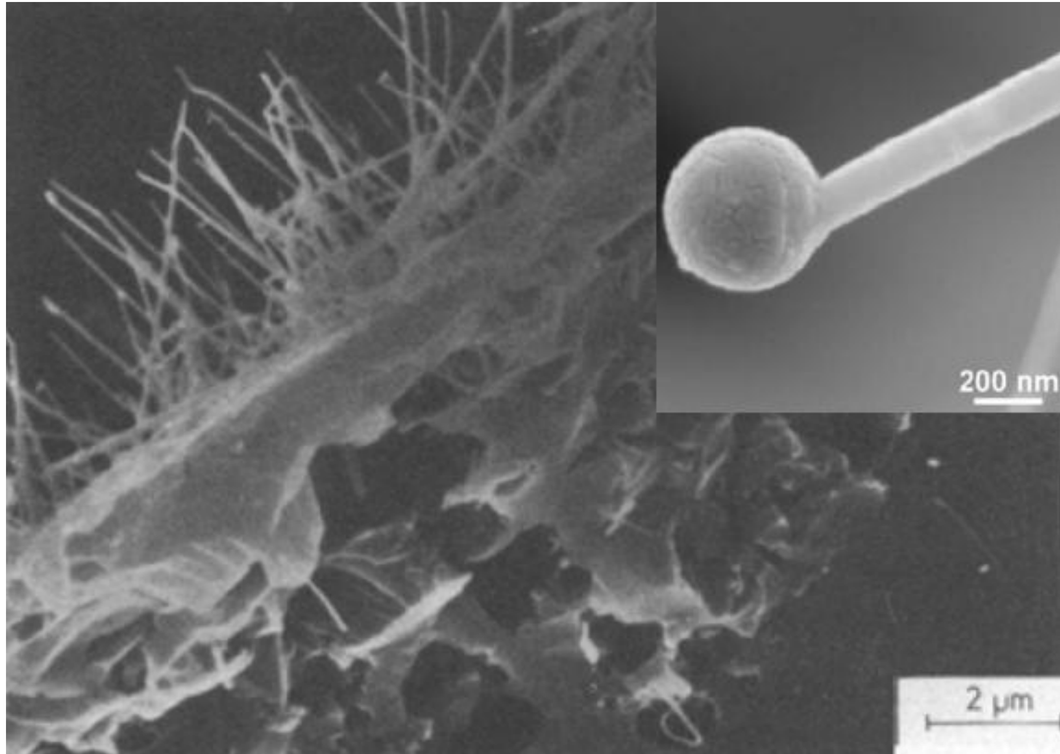

Figure 2.10: Cross section showing α-whiskers above the surface. Static nitrogen atmosphere at 1270°C after 65 hours, source: [35]. Inset: Magnified bead at the terminus of a needle (single whisker). Source: [31].

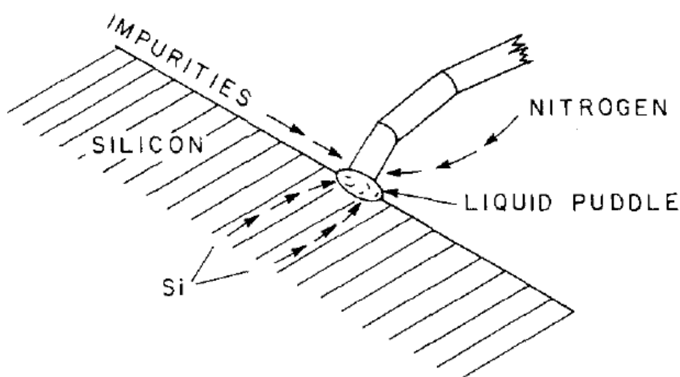

In the cases when the liquid is in the form of a puddle on the surface, it has to support the weight of the whisker. This means the whisker may have low angle grain boundaries if there is a small shift in the growth direction, illustrated in figure 2.11. Impurities might also induce this phenomenon.

Figure 2.11: Seed at the origin on the silicon surface. Low angle grain boundaries might occur due to small shift in growth direction. Source: [23].

2.3.2 Alpha matte

This compact and grained layer is produced from fine and more pure silicon grains. It does not form any needles and since the smallest grains react first, the formation of a matte leaves openings (i.e. pores) into the silicon crystal as the larger grains consume, by Ostwald ripening, the smaller grains. This is illustrated in Figure 2.12. This structure also favors static atmosphere; meaning no gas flow [23].

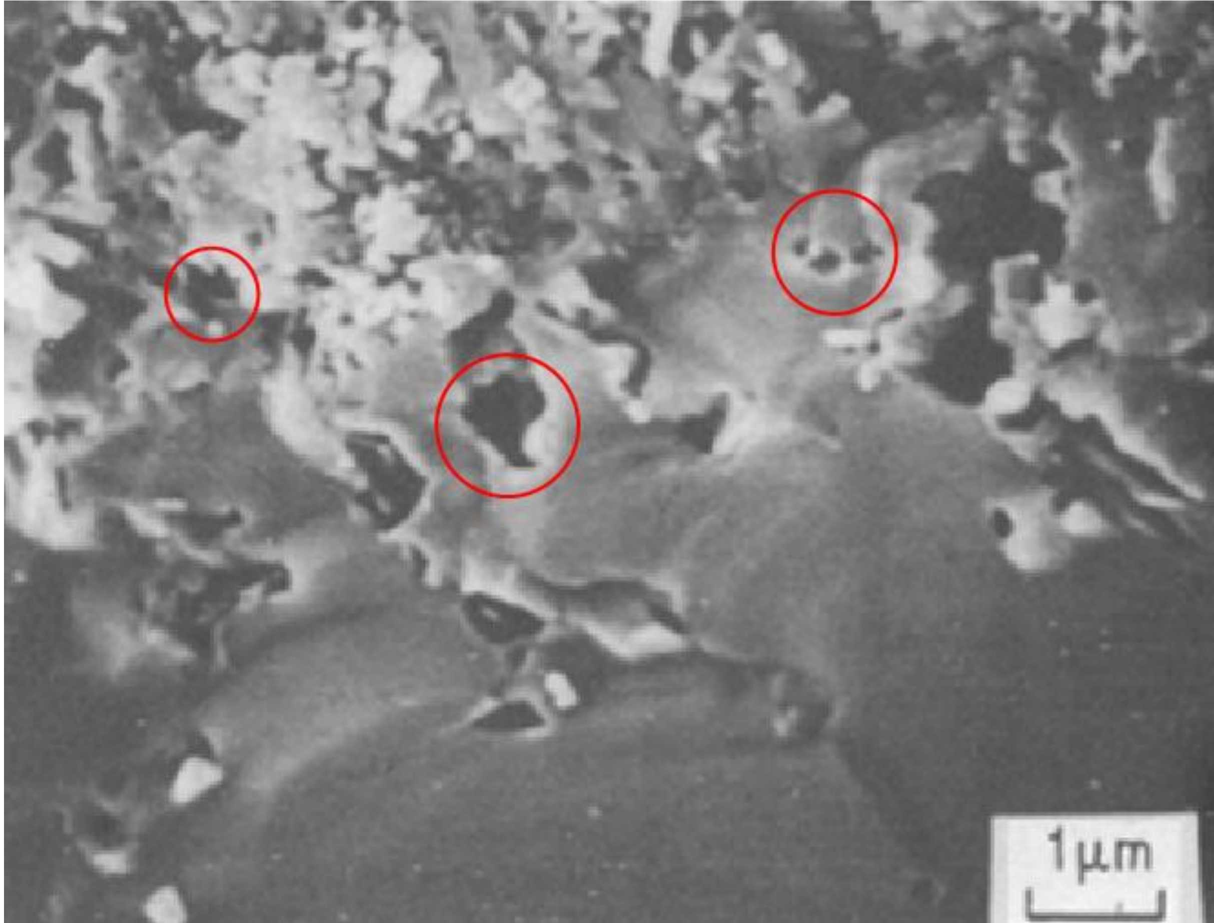

Figure 2.12: Cross section of a silicon crystal showing the α-matte structure and the generated pores on the surface. The lighter parts are silicon nitride. As the grains grow in size it opens pores in the silicon crystal, indicated by the red rings. Temperature <1400°C and no gas flow, source: [23].

2.3.3 Beta phase

The rods and spikes of the β-phase are much larger than the α-phase and grows inwards into the silicon crystal [23,13]. As established in the two previous sections the β-structure requires a liquid phase to form. This can be achieved by rapid heating of the precursor and thereby limiting the predominating α-phase reaction period prior to the formation of liquid phases, and thus hindering the closing of the pores into the liquid pools. This means the β-structures requires less pure (more inter-metallic liquid phases to form pools) and coarse grains (less surface area to compete with the α-phase). β-structure growth into the silicon crystal is shown in Figure 2.13. Because of α to β transitions, the β-structure might also be similar to the former. With higher impurities, i.e. the liquid phases form lakes, the β-phase forms dendrite formation on the surface, seen in Figure 2.5.

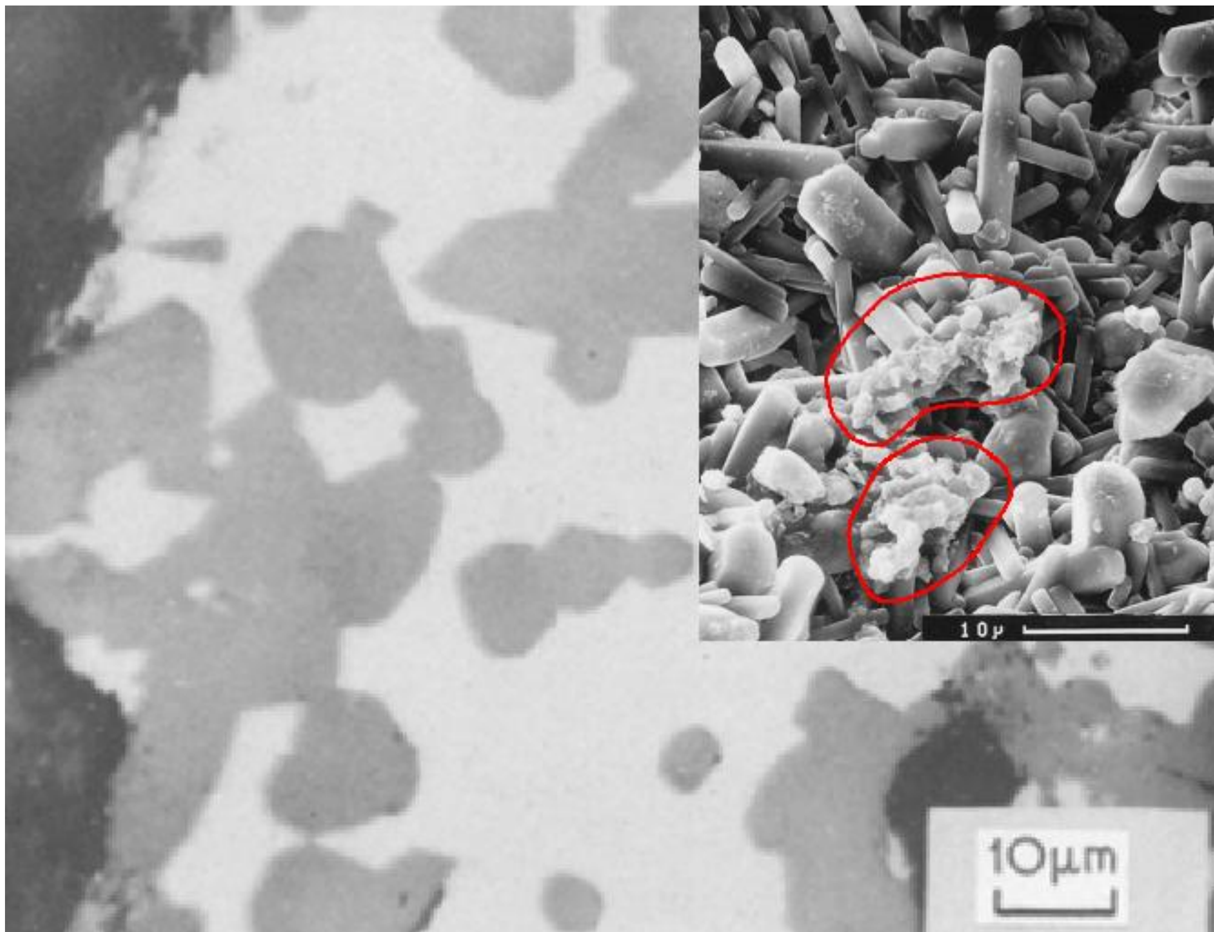

Figure 2.13: Cross section image of β-rods and spikes (grey) growth into the silicon crystal. Temperature >1450°C in rapid gas flow, source: [23]. Inset: Image of highly etched (removed) silicon surface, showing β-rods and α-matte marked by the red rings. Source: [5].

2.3.4 SiO_2

In the event of a buildup of SiO_2(s), that was not removed during the nitridation process, then it will change phases according to the Gibbs free energy plot versus temperature in seen in Figure 2.14:

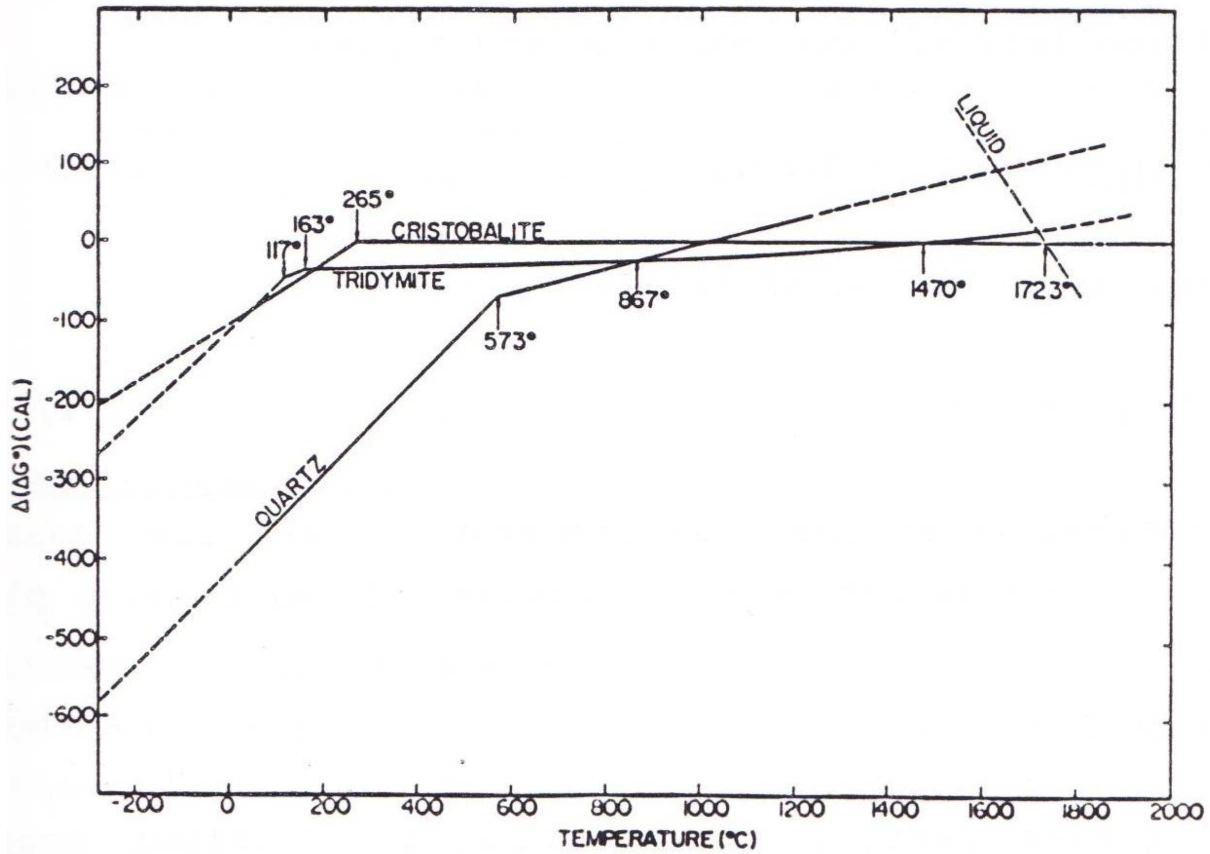

Figure 2.14: Standard free energy of different phases of SiO_2. Source: [36].

Tridymite does not usually form from pure SiO_2(s) and it is therefore possible to crystallize cristobalite directly from amorphous quartz at temperatures above 1050°C [37]. At temperatures around 1400°C the normal devitrification product from vitreous silica is cristobalite with presence of micro cracks [38], which provides an easy path for Si(g).

2.4 Diffusion

The total rate of reaction is determined by multiple factors: Gas flow, bulk diffusion and surface reaction. The first step is controllable by partial N_2 pressure and gas flow passing by the precursor grains, the second is given by material properties such as crystal structure shown in section 2.1, and the last step by catalysts (impurities) in the material. In this section an overview regarding diffusion of reactants through different materials is given.

2.4.1 Silicon nitride layer

Mono-atomic nitrogen self diffusion in polycrystalline α and β has been measured and the diffusion rates were found to be [22]:

$$D_{N,\alpha} = 3.7 \times 10^{-8} e^{\left(-\frac{233kJmol^{-1}}{RT}\right)} m^2 s^{-1} \quad (6)$$

$$D_{N,\beta} = 6.8 \times 10^{10} e^{\left(-\frac{777kJmol^{-1}}{RT}\right)} m^2 s^{-1} \quad (7)$$

These values apply within the temperature range of RBSN (1200-1410°C). Even though α and β have somewhat similar crystal structure, see Figure 2.1 and Figure 2.2, the β-structure has a higher diffusion rate at elevated temperatures, as seen in Figure 2.15. This indicates different vacancy formation energies between the two structures [22], as seen in the different activation energies in equation 6 and 7. It might be possible for atomic nitrogen to diffuse through the open rings (Figure 2.1 and Figure 2.3) of β [6], but still at a very slow rate.

Even lower diffusion values has been observed of Si(g) through α-Si_3N_4 because of the larger Si atom [39]:

$$D_{Si,\alpha} = 2.0 \times 10^{-15} e^{\left(-\frac{197kJmol^{-1}}{RT}\right)} m^2 s^{-1} \quad (8)$$

All of these values are very small and states that nitridation of large silicon grains is highly unfavorable. However, diffusion along grain boundaries is considerably faster than diffusion through the bulk, and smaller grain sizes have an advantage compared to larger [22]. Still, the diffusion rates are fairly low and considered to be the rate controlling parameter in the process of nitridation of silicon through a layer of silicon nitride [5], and also the reason why commercial production of silicon nitride takes many hours, at elevated temperatures, to complete.

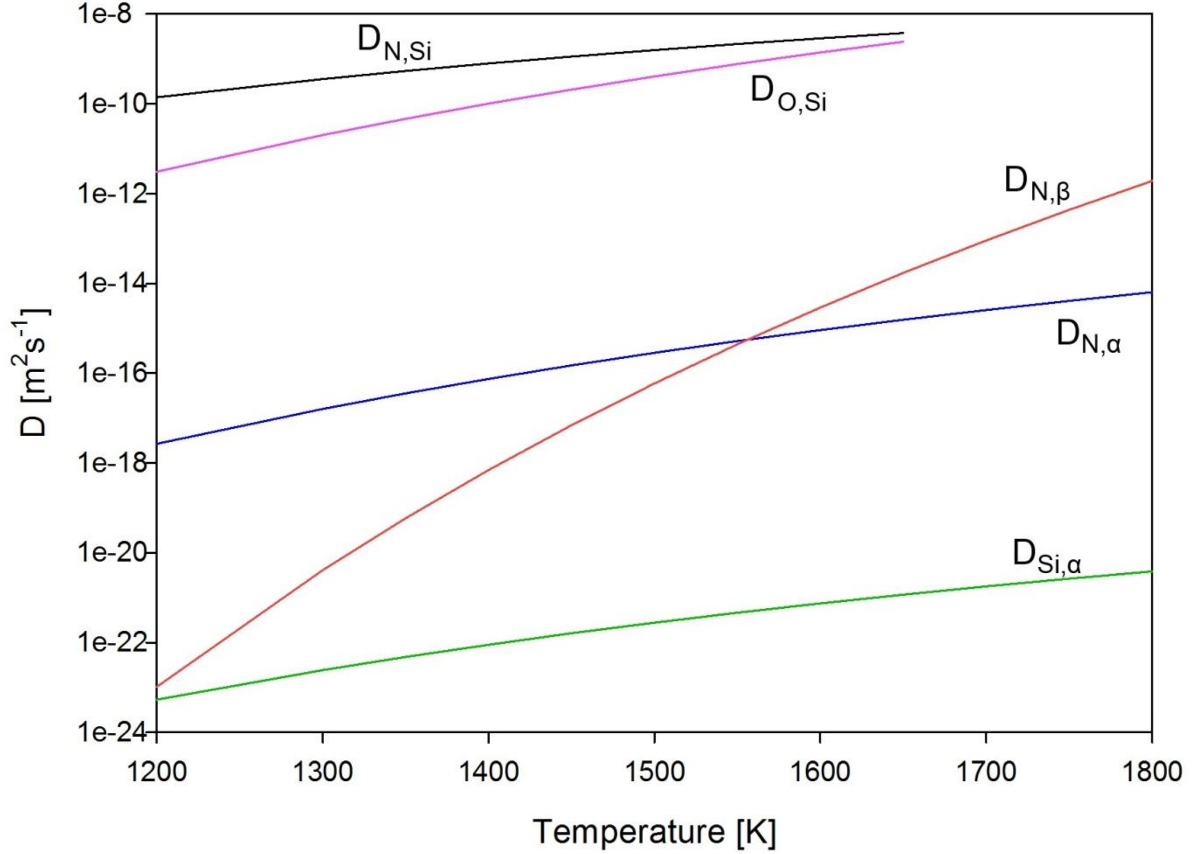

Figure 2.15: Diffusion rates based on equations 6-10. Higher diffusion rates in β-structure at elevated temperatures indicates differences in nitrogen vacancy formation energies between α and β. Diffusivities in silicon is limited to solid silicon.

2.4.2 Bulk

The diffusivity of nitrogen though the silicon is given by [40]:

$$D_{N,Si} = 2.5 \times 10^{-5} e^{\left(-\frac{120kJmol^{-1}}{RT}\right)} m^2 s^{-1} \tag{9}$$

For oxygen [41]:

$$D_{O,Si} = 1.3 \times 10^{-5} e^{\left(-\frac{244kJmol^{-1}}{kT}\right)} m^2 s^{-1} \tag{10}$$

These values are quite high, as seen in Figure 2.15, but as the temperature increases both nitrogen and oxygen will of course react with the silicon and therefore the penetration depth of the gases will be rather short. The solubility of nitrogen in liquid silicon near the melting point is around 10^{19} atoms per cubic centimeter [42,43], or at 0.02% [6].

The native SiO_2 layer on the surface of silicon metal is only a few nanometers thick [13,44], and it's diffusion values is therefore discarded as it must be removed prior to nitridation [6,13,35,45]

2.5 Partial pressures and the role of SiO

2.5.1 The Si-O-N system

The thermodynamics of the Si-O-N system is the fundament regarding stabilizing the growth of silicon nitride; Si_3N_4. In section 2.1 it was established that prior to the formation of silicon nitride, the native silica layer must be removed, at least partially so that a silica free Si surface might react with nitrogen. Figure 2.16 shows the partial pressures over SiO_2(s,l) at a constant ambient partial pressure of oxygen at 10^{-8} atm [46]:

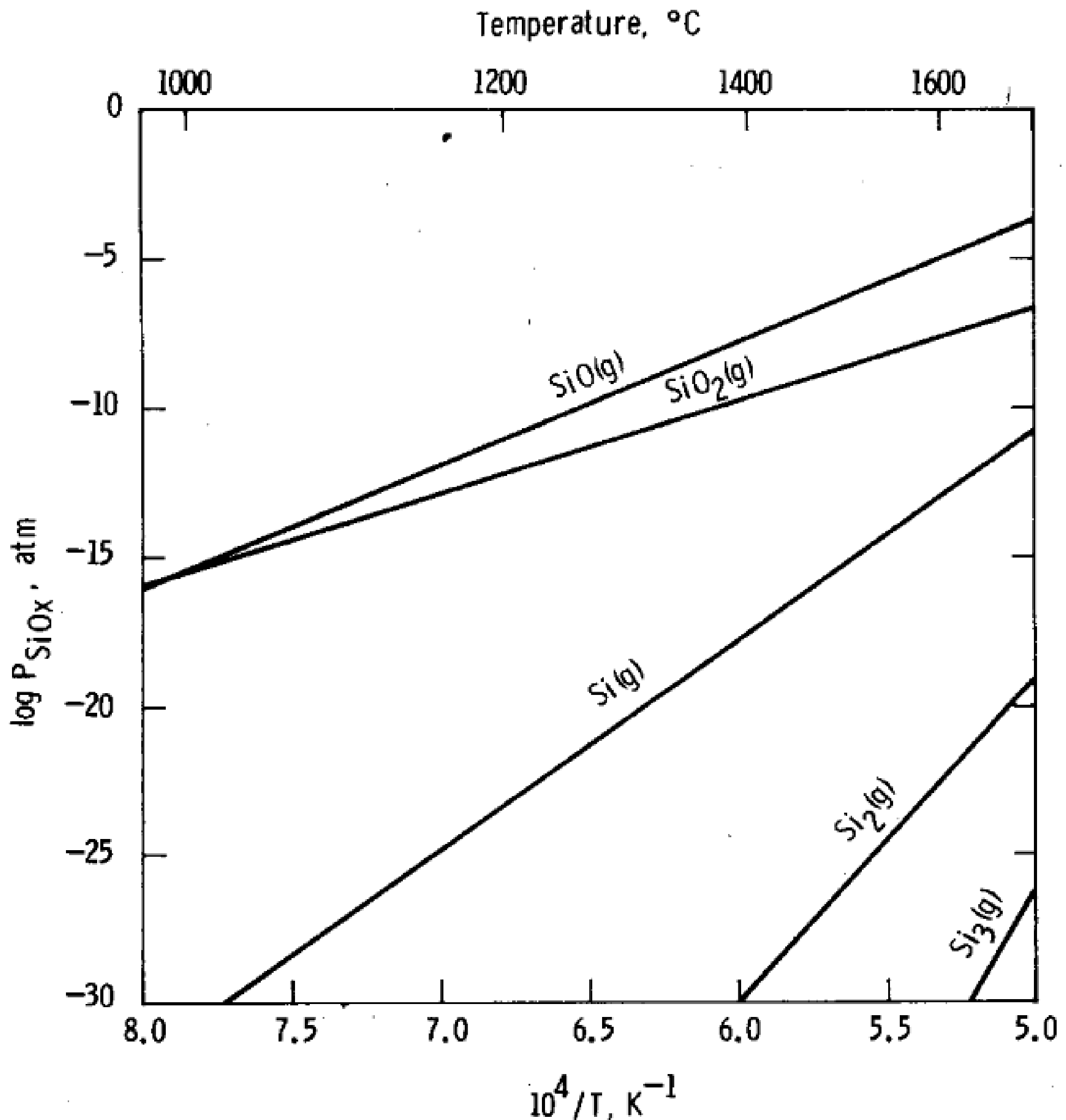

Figure 2.16: Partial pressure of various volatile species over SiO_2(s,l) in 10^{-8} P_{O2}. Source: [46].

Given that the RBSN process occurs below the melting point of silicon, the following chemical reactions compete against each other [47], and is visualized in Figure 2.17:

$$Si(s) + O_2(g) \leftrightarrow SiO_2(s) \tag{11}$$

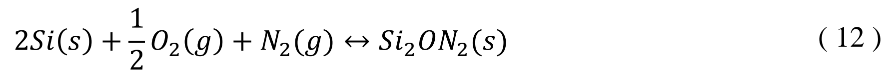

$$2Si(s) + \frac{1}{2}O_2(g) + N_2(g) \leftrightarrow Si_2ON_2(s) \tag{12}$$

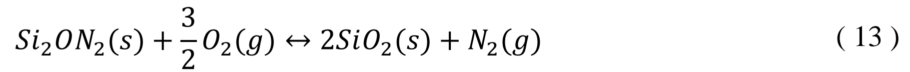

$$Si_2ON_2(s) + \frac{3}{2}O_2(g) \leftrightarrow 2SiO_2(s) + N_2(g) \tag{13}$$

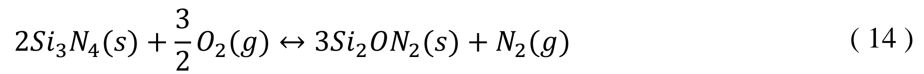

$$2Si_3N_4(s) + \frac{3}{2}O_2(g) \leftrightarrow 3Si_2ON_2(s) + N_2(g) \tag{14}$$

$$3Si(s) + 2N_2(g) \leftrightarrow Si_3N_4(s) \tag{15}$$

This means that at 1 atm pressure of nitrogen the partial oxygen pressure must be lower than ca 10^{-22} atm in order stabilize Si_3N_4 at 1250°C [48]. This is not possible in conventional, or even most laboratorial, reaction chambers. All experimental data in the literature shows however that it is possible to produce silicon nitride with some partial pressure of oxygen, and that rather SiO(g) is the active oxygen carrier; instead of investigating the stable phases represented by P_{O2} vs. P_{N2} in Figure 2.17, one should rather investigate P_{SiO} vs. P_{N2} Figure 2.18.

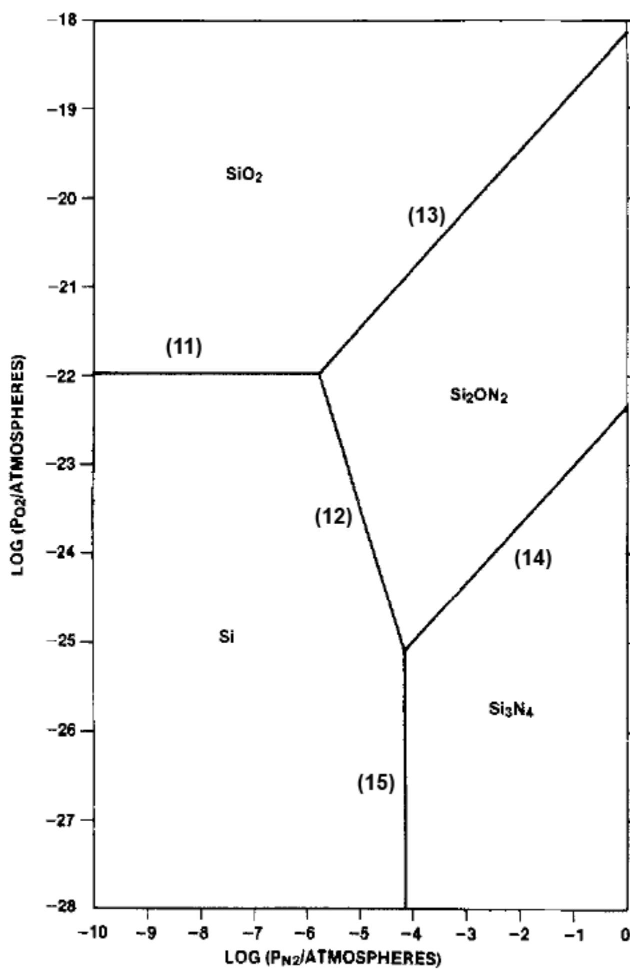

Figure 2.17: Log-plot partial pressure of nitrogen versus oxygen. The lines separating the stable phases are represented by eq. 11-15. Temperature is constant at 1250°C, source: [48].

Rearranging eq. 11-14 with SiO(g) as the active oxygen carrier, and keeping eq. 15 as it is:

$$SiO_2(s) + Si(s) \leftrightarrow 2SiO(g) \quad (16)$$

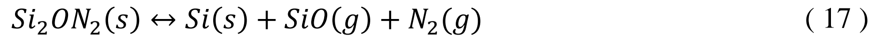

$$Si_2ON_2(s) \leftrightarrow Si(s) + SiO(g) + N_2(g) \quad (17)$$

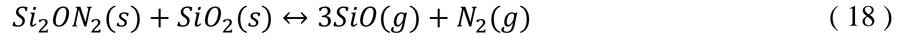

$$Si_2ON_2(s) + SiO_2(s) \leftrightarrow 3SiO(g) + N_2(g) \quad (18)$$

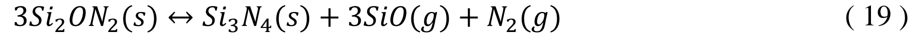

$$3Si_2ON_2(s) \leftrightarrow Si_3N_4(s) + 3SiO(g) + N_2(g) \quad (19)$$

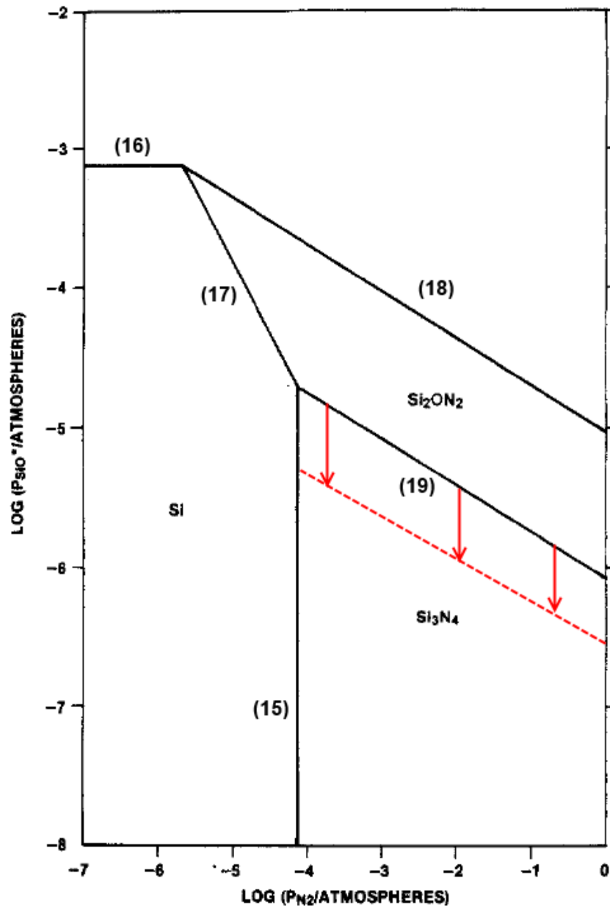

From Figure 2.18 at 1 atm pressure of nitrogen, the partial pressure of SiO(g) must be lower than 10^{-6} atm to stabilize Si_3N_4 at 1250°C. This is feasible compared to Figure 2.16 in the temperature range of RBSN, but the pressure might locally be higher during the earlier stages where the native silica layer is rapidly removed. However, as the partial pressures stabilizes, Si_2ON_2 might convert back to Si_3N_4, c.f. eq. 19. The literature does only report very few findings of trace amounts of silicon oxynitride in the final product [46] after nitridation. It is however present at high partial pressure of oxygen (oxidation of silicon nitride) at elevated temperatures [49]. Mark that higher temperatures lowers the line separating the two phases.

Figure 2.18: Log-plot partial pressure of nitrogen versus SiO. The lines separating the stable phases are represented by eq. 15-19. Temperature is constant at 1250°C. The red dashed line indicates the movement of the line in respect to stabilizing Si_3N_4 (eq. 19) at higher temperatures, given 1 atm N_2. Source: [48].

An important side-reaction is the reported nitridation of SiO(g), by VLS explained in section 2.3, where the Si(g) is exchanged by SiO(g) [13]. This is favorable to the growth of whiskers, due to the otherwise extreme low partial pressure of Si(g) seen in Figure 2.16.

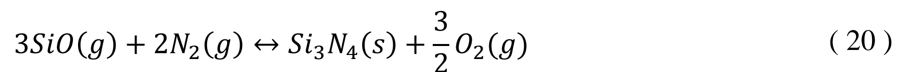

$$3SiO(g) + 2N_2(g) \leftrightarrow Si_3N_4(s) + \frac{3}{2}O_2(g) \quad (20)$$

2.5.2 List of partial pressures at 1330°C

Beneath is a list of partial pressure of selected impurities over its own metal (i.e. P_{Fe} over Fe) at 1330°C. Numbers taken from [50] (Appendix A):

Element	Partial pressure at 1330°C [atm]
Si	3×10^{-7}
Fe	1×10^{-6}
Al	9×10^{-5}
Ca	3×10^{-1}
Cu	2×10^{-5}

2.6 The function of impurities

The most common impurities in the silicon precursor are: Aluminium, iron and calcium. These elements, together with additives from other transition metals such as copper, chromium and yttrium [51], effect the morphology and phase composition of the finished product of silicon nitride. In this section some of the most common impurities and additives will be discussed in further detail. Please note that the literature are based on very pure silicon grains with added pure elements of impurities. This is not in consistence with the mass production, where there will always be a more or less homogenous mixture of several impurities in the precursors.

2.6.1 Iron

Iron as a transition metal will have positive effects on removing the silica layer (Figure 2.20) and aid the overall nitridation process by forming a liquid phase composition of $FeSi_2$ at temperatures exceeding 1212°C [5,11,13,52,45], where it acts as a catalyst in a VLS process (droplet), contribute to higher vapor pressure of Si(g) and SiO(g) over the pools (contribute to α-Si_3N_4 formation), and solves monoatomic nitrogen to form β-Si_3N_4. This is visualized in Figure 2.19.

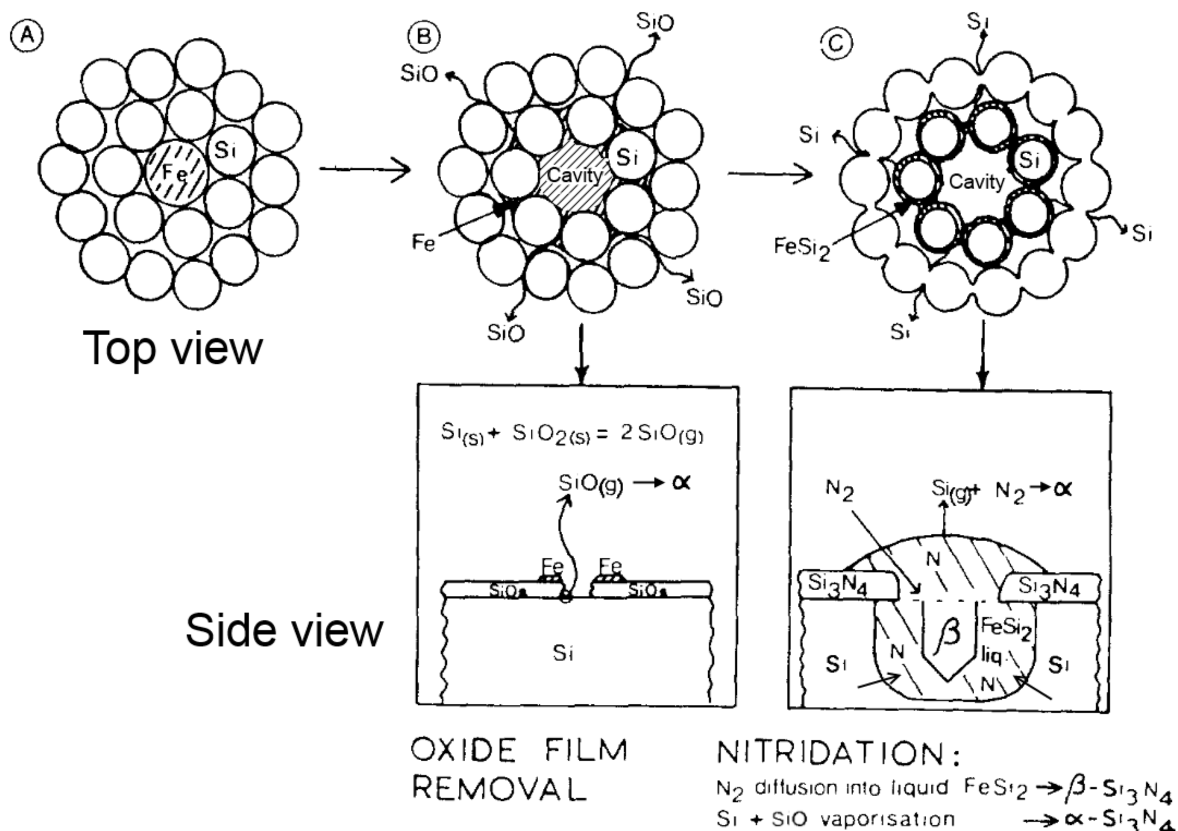

Figure 2.19: Schematic overview of the function of Fe during the nitridation process: A) Si crystal containing Fe particle. B) Initial stages; cavity formation and oxide film removal as Fe (seen as a shade beneath the surface) liquefies, SiO(g) evaporation forming α-Si_3N_4 whiskers. C) Nitridation via $FeSi_2$ liquid, also Si sintering in Fe free regions. Source: [11].

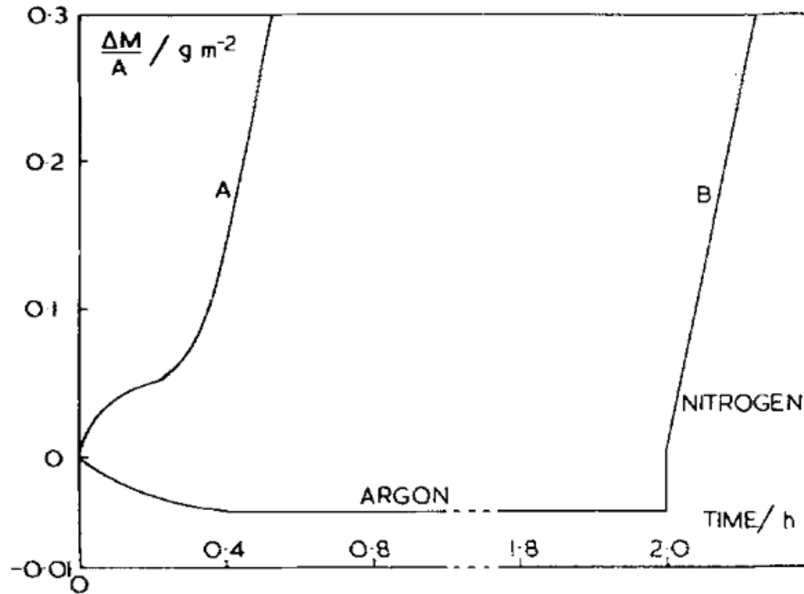

Figure 2.20: The effect of Fe on the SiO_2 layer in a TGA. A) Nitridation of Si powder containing 2000 ppm Fe impurities at 1370°C in pure nitrogen. B) Same sample, but kept in an inert argon atmosphere for 2 hours prior to nitridation. Oxide film removal as weight loss, and the following extreme rapid weight gain when the gas flow is switched to pure nitrogen. [11].

The literature reports as little as 55ppm of Fe impurities might improve conversion rates of silicon to silicon nitride significantly, especially the α-phase at smaller concentrations [11]. This effect increases up to around 1000 ppm as by then further increments promotes virtually only more β at the expense of α, shown in Figure 2.21:

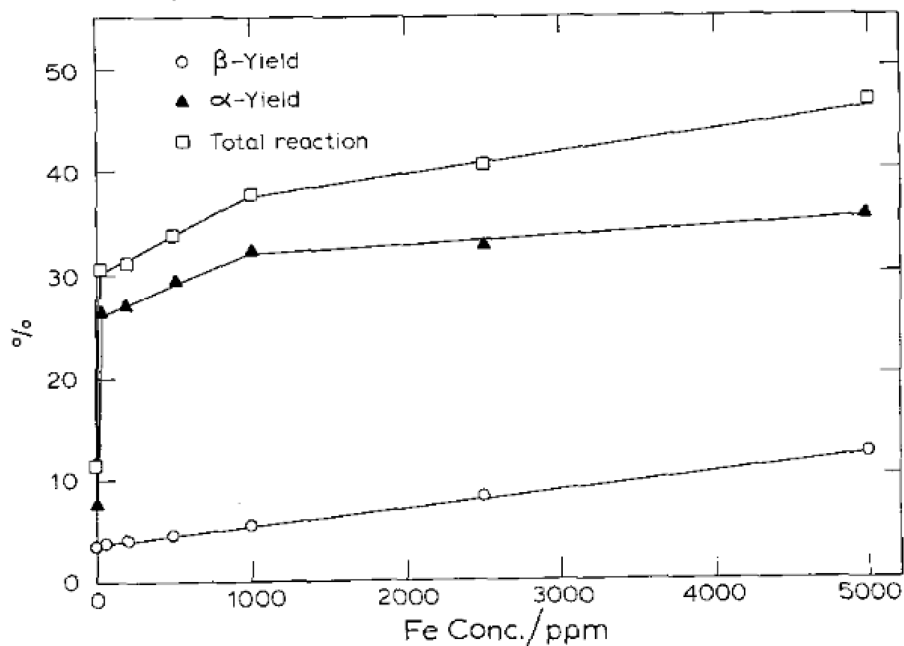

Figure 2.21: The formation of the two phases as a function to iron content plotted against total yield. Nitridation in pure nitrogen for 10 hour at 1350°C. Grain size <53μm, source: [11].

Boyer and Moulson [11] postulate that "devitrification of the surface silica by iron reduces its adhesion to the underlying silicon" and that remaining oxygen in the atmosphere might react with the now exposed silicon layer, but reforming as SiO(g) instead of SiO_2(s) because of the presence of iron, given that the partial pressure of oxygen is sufficiently low. This will lead to a rapid formation of α-Si_3N_4 by the vapor phase reactions mentioned in section 2.3, with Si(g) and SiO(g) as precursors. However, at temperatures below the melting point of the disilicide (1212°C) the silicon will diffuse from the bulk, through the solid $FeSi_2$, and form silica, since $FeSi_2$ has a much lower affinity for oxygen than Si metal, but a higher diffusivity of Si than what the silica layer has of oxygen [53].

Another feature of iron impurity is the generation of vacancies in the Si_3N_4 lattice. Even though Fe does not go into solid solution with Si [54], it does have a solubility of 0.6 at% in silicon nitride [30]. The iron, as Fe^{3+}, swaps with Si^{4+} and thereby forces an N-vacancy in order to remain charge neutral. This opens up for much higher vacancy diffusion through the bulk (extrinsic + intrinsic), and might improve the nitridation process significantly as the nitrogen diffusion is established as the rate limiting step, c.f. section 2.4.

2.6.2 Aluminium

Traces of Al might be good in capturing excess O_2 from the silica layer and form Al_2O_3 [55]. From the Ellingham diagram [56] (Appendix B) alumina is stable at a partial pressure of oxygen above 10^{-26} atm at 1330°C. This is lower than that for silica, which means alumina will stabilize first and only excess oxygen will produce silica, given that the material is perfectly homogeneously mixed. Because the free energy in forming Al_2O_3 is relatively lower than that of AlN [57] (Appendix B), the latter phase will not compete against the formation of Si_3N_4 as long as there is any oxygen present.

It is also shown in the literature that aluminium, as a liquid phase, promotes β structure [55,51,13]. There are some arguments in the literature that an alumina crucible might influence the nitridation properties if in directly contact with the silicon precursor. Moulson [13] reports that because of alumina, a liquid phase would be expected at temperatures lower than that of $FeSi_2$, which others have confirmed [10].

2.6.3 Calcium

Among all the additives and impurities, only calcium promotes the α-phase and the overall yield at the cost of β-phase (only trace amounts) [51]. This applies to low level of impurities, as higher levels (≥1%) gave lower yield, but still enhanced α significantly. The downside of using calcium is the notable decrease of high temperature strength of the silicon nitride, as it might form an eutectic glass phase composing of CaO-Al_2O_3-SiO at 1170°C [51,58].

2.6.5 Copper

Small amounts of copper additives to the silicon precursor gives a boost to nitridation yield but suppresses the growth of β-phase at the lower temperature end of RBSN (1200°C). On the other hand high temperature (>1300°C) lowers the yield but then promotes the β-phase [51]. The inter-metallic compound, Cu_3Si melts at 859°C [59], which is much lower than that of iron.

2.6.6 Inter-metallic etching effect

Inter-metallic particles on the surface of silicon might form lithography-free etch micro patterns by the means of evaporating the top part of the silicon layer before the evaporation of the inter-metal itself [60]. The micro patterns' form is determined by the silicon crystal orientation on the surface. This process is best described by Figure 2.22 below, and visualized in Figure 2.23 [60]:

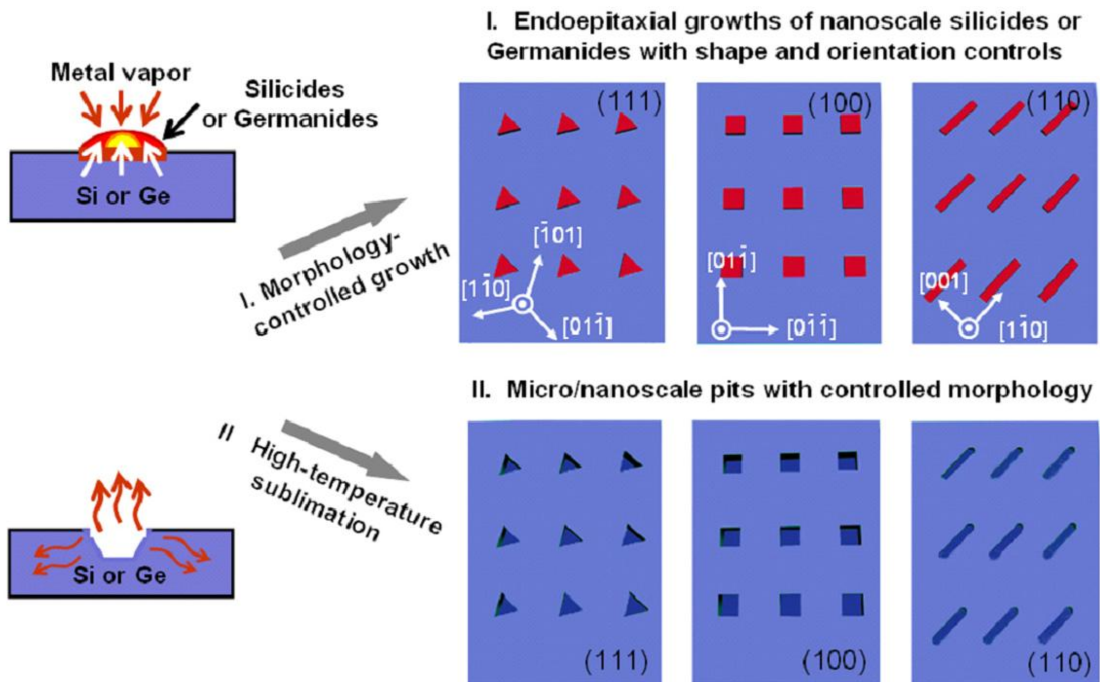

Figure 2.22: Condensation of metal vapor or surface diffusion of metal/inter-metallic particles such as e.g. $FeSi_2$. These droplets will act as catalysts evaporating the underlying silicon crystal. The pit forming beneath the droplet is shape controlled by the crystal orientation. Final step is evaporating of the droplets, which leave behind the finished micro patterns.

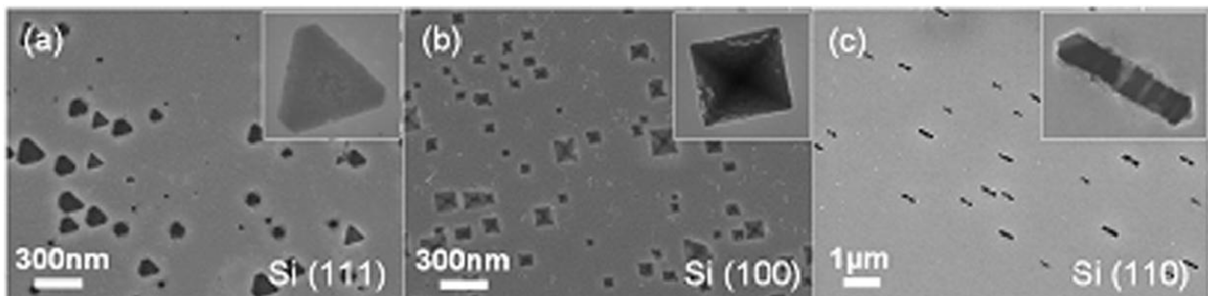

Figure 2.23: Micro and nano scale pits forming a pattern on the silicon crystal surface The same orientation of all the pits indicate that the surface has a uniform crystal orientation. Source: [60].

3 Experimental

3.1 Apparatus and samples

3.1.1 Thermogravimetric analysis

Previous works [61] were used as guidelines in this report. A predefined temperature program (Figure 3.4) was found optimal, with the exception of the isotherm holding time, which was increased to 10 hour to emphasize the difference between the stages, and the gas flow was set to pure nitrogen. The container for the samples is a DTA Al_2O_3 crucible, with 6.0 mm diameter and 11.0 mm high walls, made by Netzsch. These were filled with 80mg of sample for each run.

In short; the mass increase recorded during a TGA will be a good indication of how much of the material has been transformed, given that the reaction reactants and products are known. The TGA experiments have been carried out on a Netzsch STA 449C Jupiter at NTNU.

3.1.2 XRD

An apparatus with the serial name D8Davinci, manufactured by Bruker, was used to determine and confirm the different phases present in the samples after the TGA. Detection parameters were 15-75° with a 0.3° slit over a period of 60 minutes. For monochromatic XRD a Siemens D5000 was used. This apparatus uses a quartz to generate the monochromatic wave, and uses 16h to scan 15-65° through an automatic slit. In both cases the programs Diffrac.EVA made by Bruker was used to present the results.

3.1.3 SEM and EDS

Most of the pictures and all element analysis were taken by a Hitachi S-3400N. The higher resolution images was taken by Hitachi SU6600 FE-SEM. The program Aztec version 2.2 by Oxford Industries was used in gathering EDS results from BSE signal.

3.1.4 Samples

The silicon powders were supplied by Elkem AS Silicon Materials and stored as-received in zip lock bags at ambient indoor conditions, with the exception of a small portion of sample A, which was stored in humid conditions at 22°C. The powders are milled to smaller sizes: <75 µm for the fine grain sizes, 0.2-0.8mm in diameter for the coarse grains and <200µm for the copper rich grains. The table 3.1 describe the fine samples used by Hem 2013 [7] and the coarse samples used in this report.

Table 3.1: Element contents of the samples. Data provided by Elkem Silicon Materials. The fine samples A, B, C and D were used by Hem 2013 [7], c.f. figure 1.1 and 1.2.

Sample	PSD	Si Wt%	Fe Wt%	Al Wt%	Ca Wt%	Ti Wt%	Cu Wt%
A (fine)	<75 µm	99.9	<0.002	<0.002	<0.002	<0.002	-
B (fine)	<75 µm	99.8	0.031	0.083	0.011	0.001	-
C (fine)	<75 µm	99.5	0.135	0.215	0.025	0.013	-
D (fine)	<75 µm	98.3	0.71	0.74	0.09	0.100	-
B (coarse)	0.2-0.8 mm	99.8	0.031	0.098	0.011	0.001	-
C (coarse)	0.2-0.8 mm	99.5	0.130	0.209	0.020	0.010	-
Cu Lo	<200 µm	98.5	0.610	0.604	0.071	0.074	0.021
Cu Hi	<200 µm	98.6	0.578	0.559	0.063	0.070	0.098

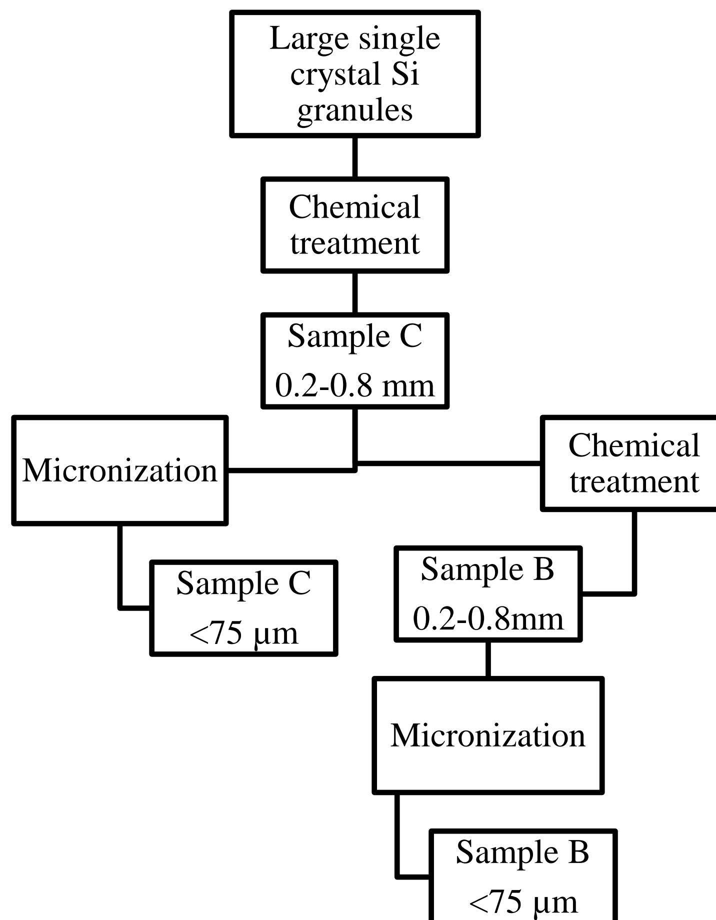

Figure 3.1: Schematic illustration on how the coarse and fine powders of sample B and C are produced. With permission from Elkem Silicon Materials.

3.2 Procedure

3.2.1 Thermogravimetric analysis

To better understand the growth mechanisms during the nitridation of silicon, three different stages was investigated, as illustrated in Figure 3.2:

- Before the process starts, that is; the as-received material
- Stage 1; just before the rapid mass increase and the onset of nitridation. This was marked by the sudden endothermic reading from the TGA apparatus, seen in Figure 3.3, indicating a phase change.
- Stage 2; right after the rapid initial growth. This point was more diffuse, but marked at the end of the linear mass increase based on results from a full run (to stage 3)
- Stage 3; after raising the temperature to 1330°C and holding for 10 hours before cooling to room temperature

To achieve this the full run to stage 3 was first conducted for both sample B and C. By doing so it was easy to see at what time and temperature the two other stages occur. Next step was then to manually abort the full temperature program, illustrated in Figure 3.4, at the right moment for both samples in stage 1 and 2. This was done without any problems, and stage 2 also coincided at the same time and temperature for both samples.

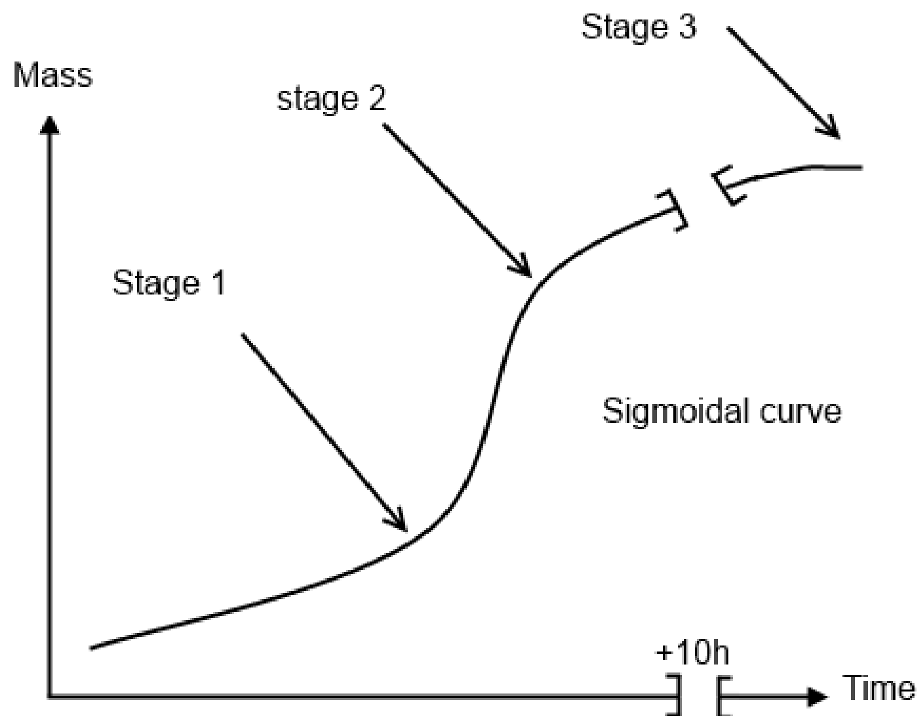

Figure 3.2: Schematic illustration of the 3 stages investigated.

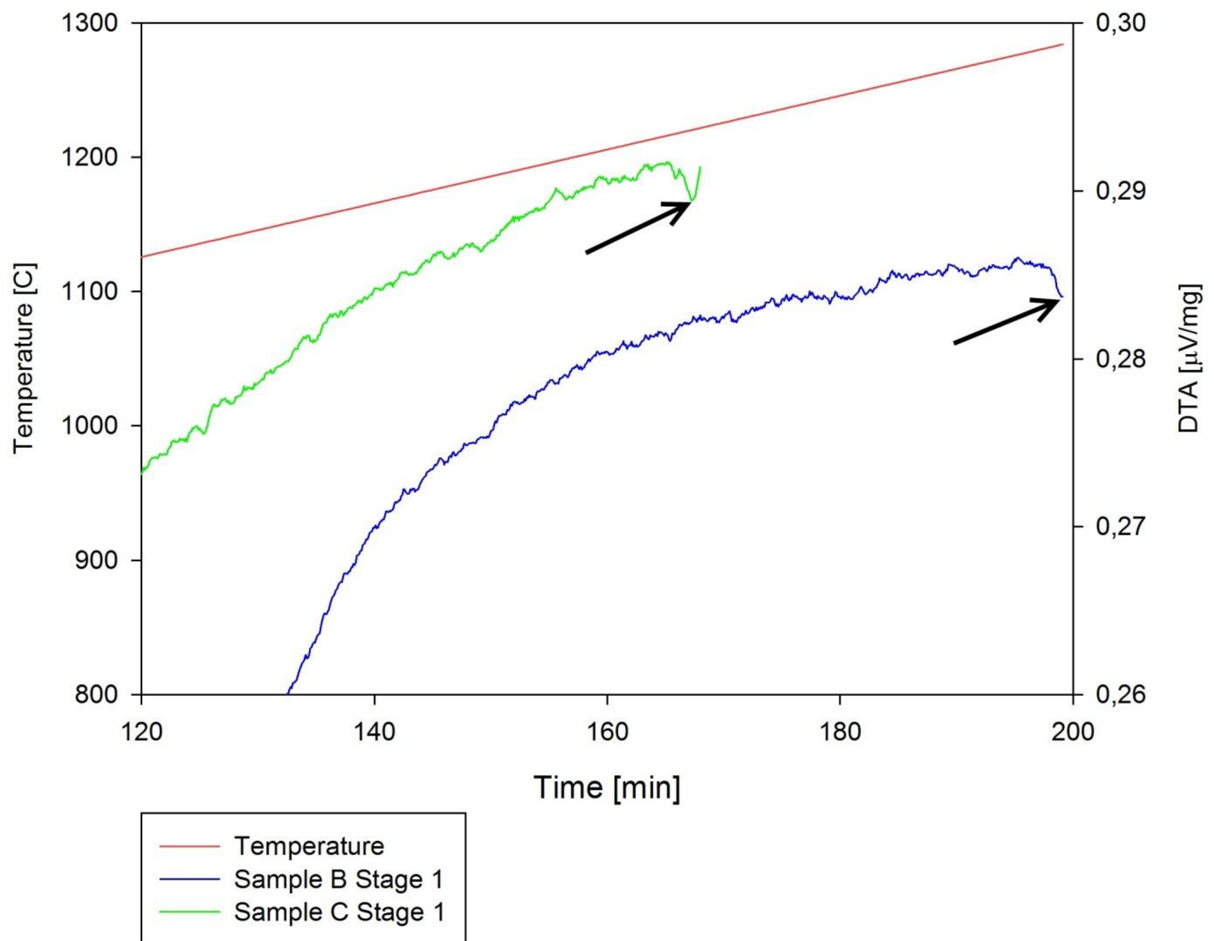

Figure 3.3: Showing the DTA curves from the TGA machine. The program was halted at the onset of an endothermic reaction, marked by the black arrows, indicating a phase change.

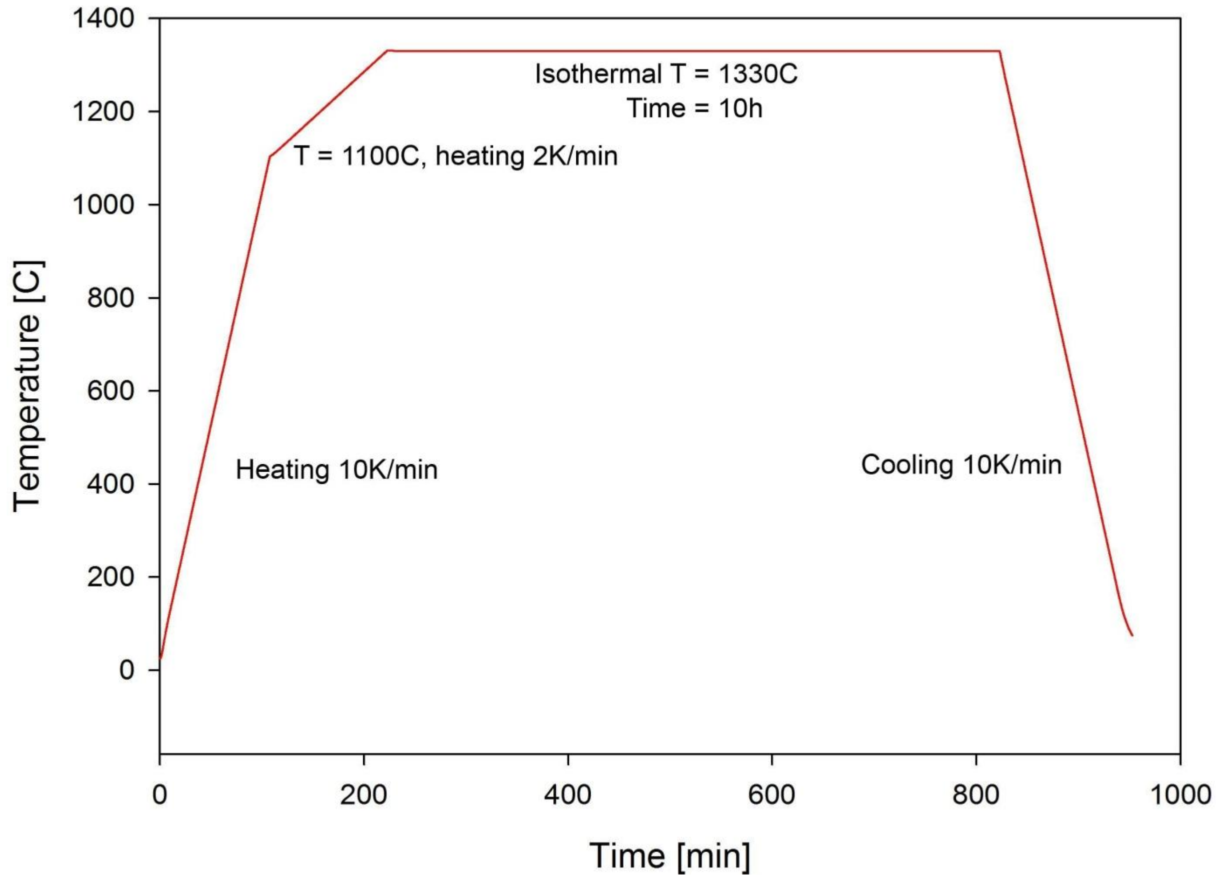

Figure 3.4: Schematic setup of the temperature program used in TGA for all samples. Taken from Øvregård [61].

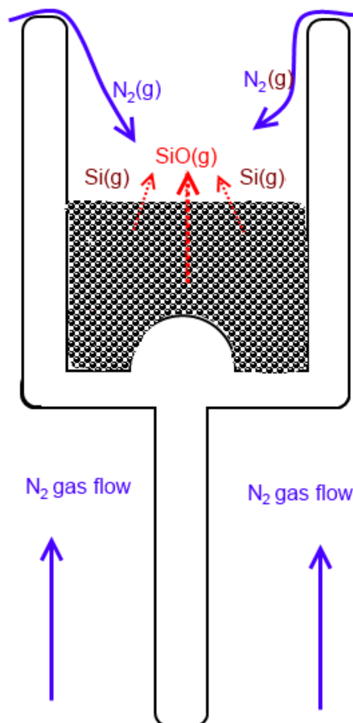

The setup of the TGA apparatus is roughly sketched in Figure 3.5 with focus on the crucible. The gas flow comes from beneath and the flow into the crucible is illustrated by blue arrows. The heating elements surround the crucible along the walls, but not the top or bottom. During the temperature program it is expected that Si(g) and SiO(g) will evaporate from the surface of the grains. In the case of coarse grains, it is also expected that the evaporation deeper into the charge contribute to an increase of partial pressure of these gases on the surface of the sample, illustrated by red arrows, where these gases meet the front of the nitrogen gas.

Figure 3.5: Sketch of the crucible inside the TGA chamber with indications of gas flow paths and increase partial pressure of volatile species on the surface of the sample.

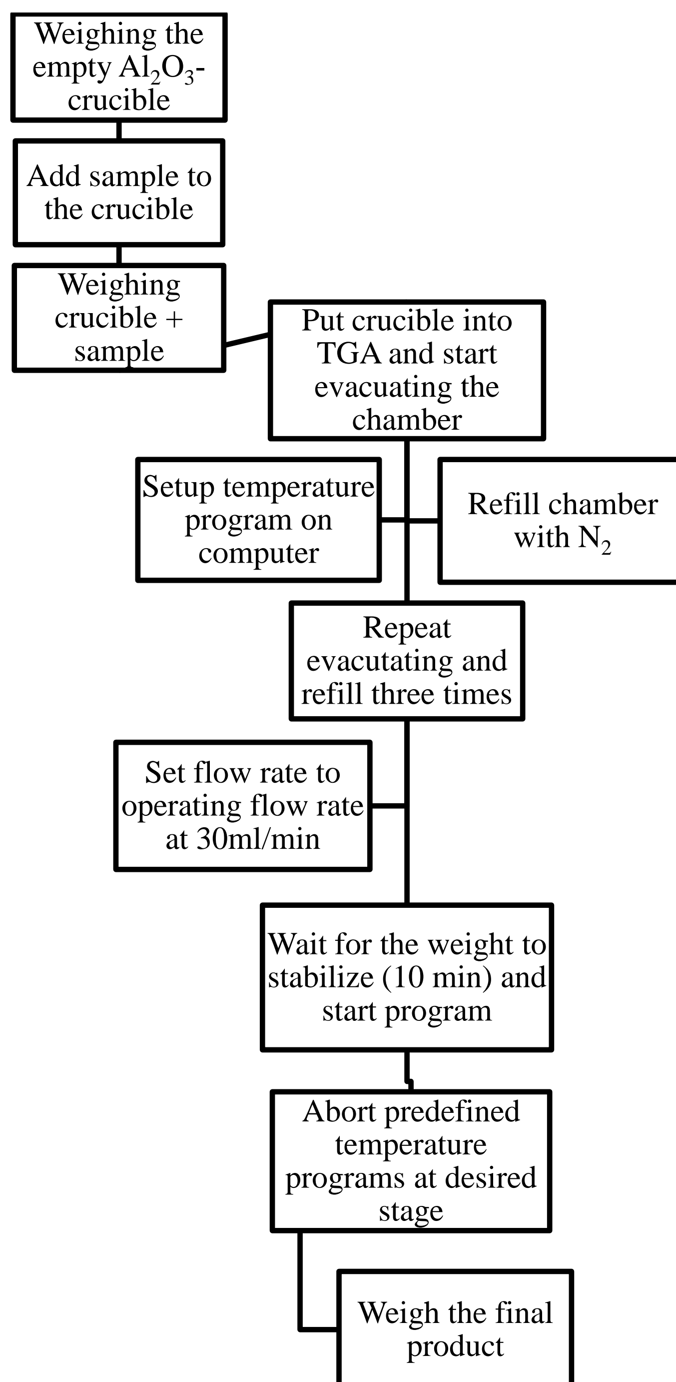

Figure 3.6: Schematic illustration of sample preparation.

The program logs 100 times each minute. A background measurement was done prior to the actual runs and this background will later be subtracted by the other measurements to show correct weight readings. The result are presented in % mass gain.

3.2.2 XRD

To get accurate plots from the XRD apparatus one needs fine powder. The samples from the nitridation were too coarse and therefore made finer by the use of pestle and mortar made of non crystalline material. This procedure will not generate any artifacts in the analysis. After a while a fine paste was achieved and then the sample was soaked with ethanol and sucked up into a dropper and squeezed onto a sample holder with a single silicon crystal (which is oriented to give zero refraction intensity). The ethanol eventually evaporated and a fine thin film was left behind. The procedure is illustrated in Figure 3.7. Only stage 2 and 3, as well as the as-received precursors, will be studied by XRD. Stage 1 was considered to have too little change from the as-received plot, and will therefore not be investigated.

3.2.3 SEM and EDS

Due to the depth of the crucible and the possibility of non reacted material in the lower levels, only grains from the top of the charge were used in SEM and EDS analysis. The only exception were the as-received samples, which the grains were picked by random. Each grain was fastened to a copper pin by dual-sided carbon tape before mounted into the vacuum chamber. Some samples were split in half by a stainless steel tweezers to make cross section images. The samples prepared for Secondary Electron (SE) imaging were also coated by gold to give sharper pictures. This was done by the use of Edwards Sputter Coater S150B at 15mA in two times one minute intervals. The pictures were then taken at 2000 times magnification at 12keV and 15keV for SE and backscatter electron (BSE), respectively, if not described otherwise. See Figure 3.7 for step by step procedure.

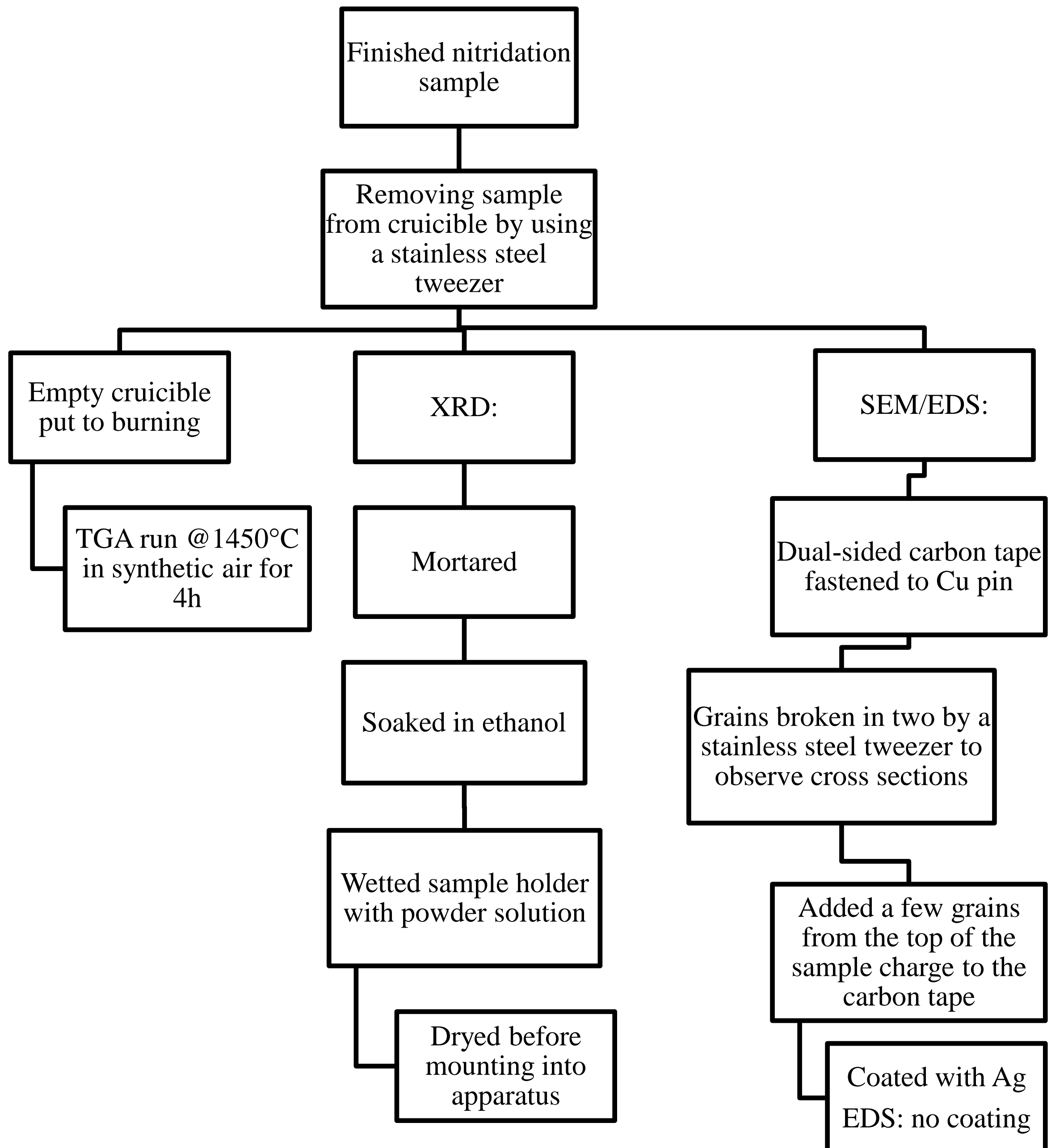

Figure 3.7: Schematic illustration of procedures of finished nitridation samples.

4 Results

4.1 TGA

4.1.1 Humid storage conditions

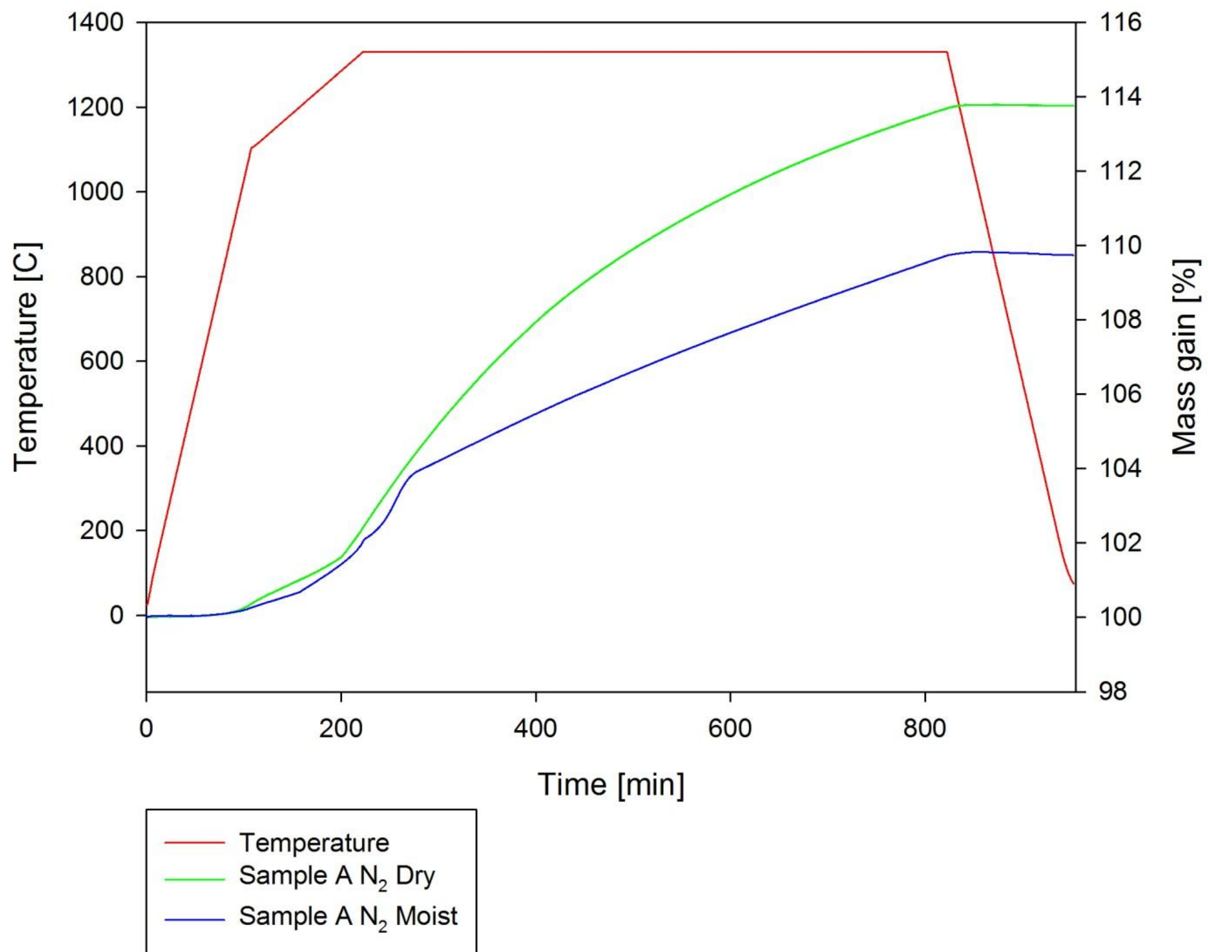

Figure 4.1: Pure silicon powder has been stored 3 months in high humid conditions. The TGA plot shows that moist storage conditions retards the nitridation process. Notice the onset of a linear mass growth after 270 minutes at 1330°C isothermal holding temperature. Separating into stages; Dry: Stage 1 at 1280°C and stage 2 estimated to be 40 min into the isothermal zone with 1330°C. Moist: Stage 1 at 1330°C and stage 2 also estimated to be 40 min into the isothermal zone.

4.1.2 Cu-added sample

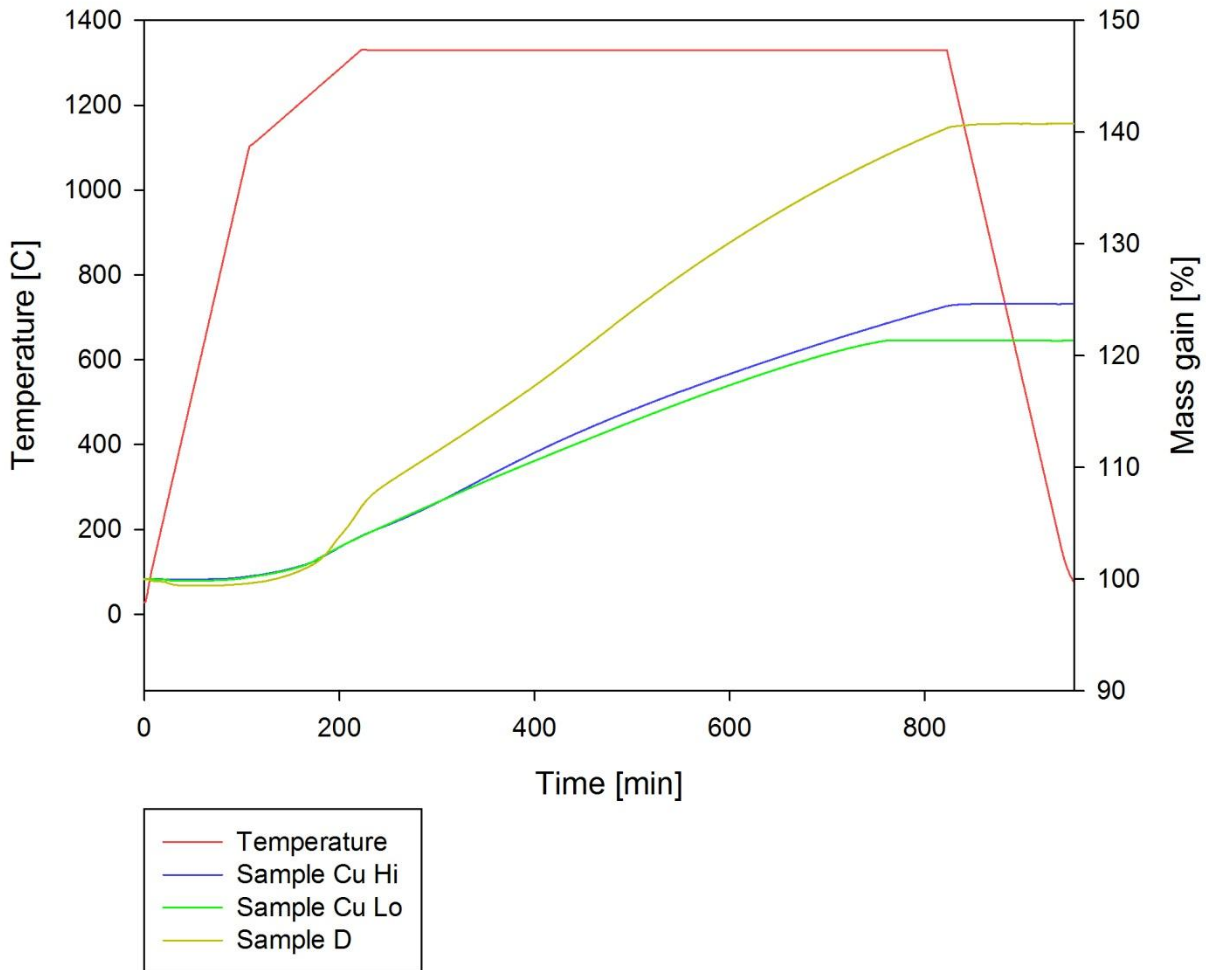

Figure 4.2: Comparing the two Cu samples with the similar, but non-Cu added, sample D based on results from Hem 2013. Observe that the Cu samples have a slow mass grain already from ca 850°C and onwards. The Cu Lo flats out before the temperature program ends and that both Cu samples do not have a clear sigmoidal curve, which is typical for the nitriding process, but rather a continuous linear growth.

The Cu samples have larger grains (<200µm) than the D sample (<75µm), and all samples were loosely sintered, especially the Cu samples (but not too hard to remove from the crucible), when completed. It is not viable to separate the Cu sample curves into the stages defined in section 3, and if one disregard the early flattening of the curve of sample Cu Lo, then Cu Hi and Cu LO are practically identical.

4.1.3 Coarse B and C

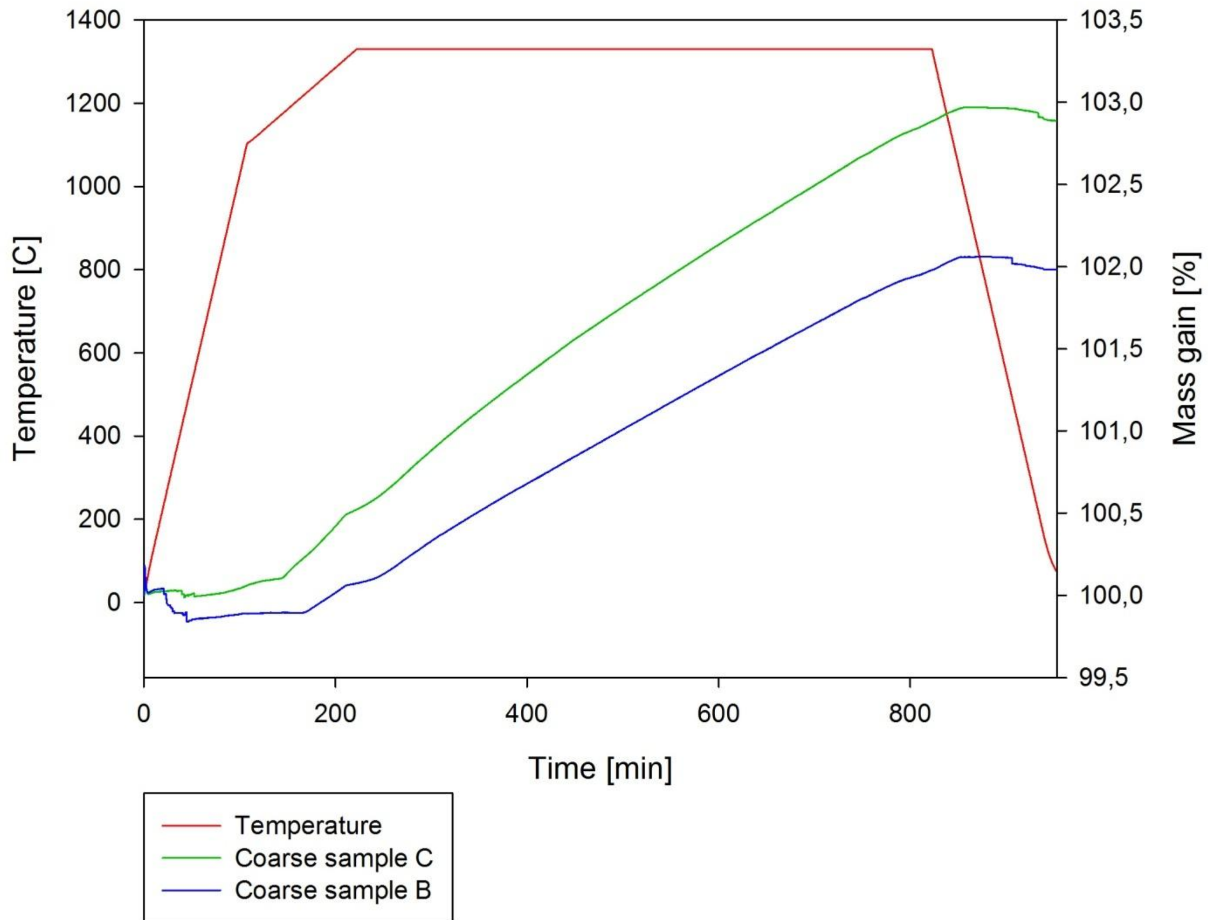

Figure 4.3: TGA results from coarse sample B and C run 1, taken March 2014. The onset of stage 1 and 2, as described in section 3: B) stage 1 at 1280°C and stage 2 at 1300°C, C) stage 1 at 1220°C and stage 2 at 1300°C. The sudden drop in mass at the beginning is due to unclean environment as the apparatus is used in many different projects with different samples. The difference in relative mass gained between the two samples is significant (% wise), but rather insignificant weight wise compare to other samples.

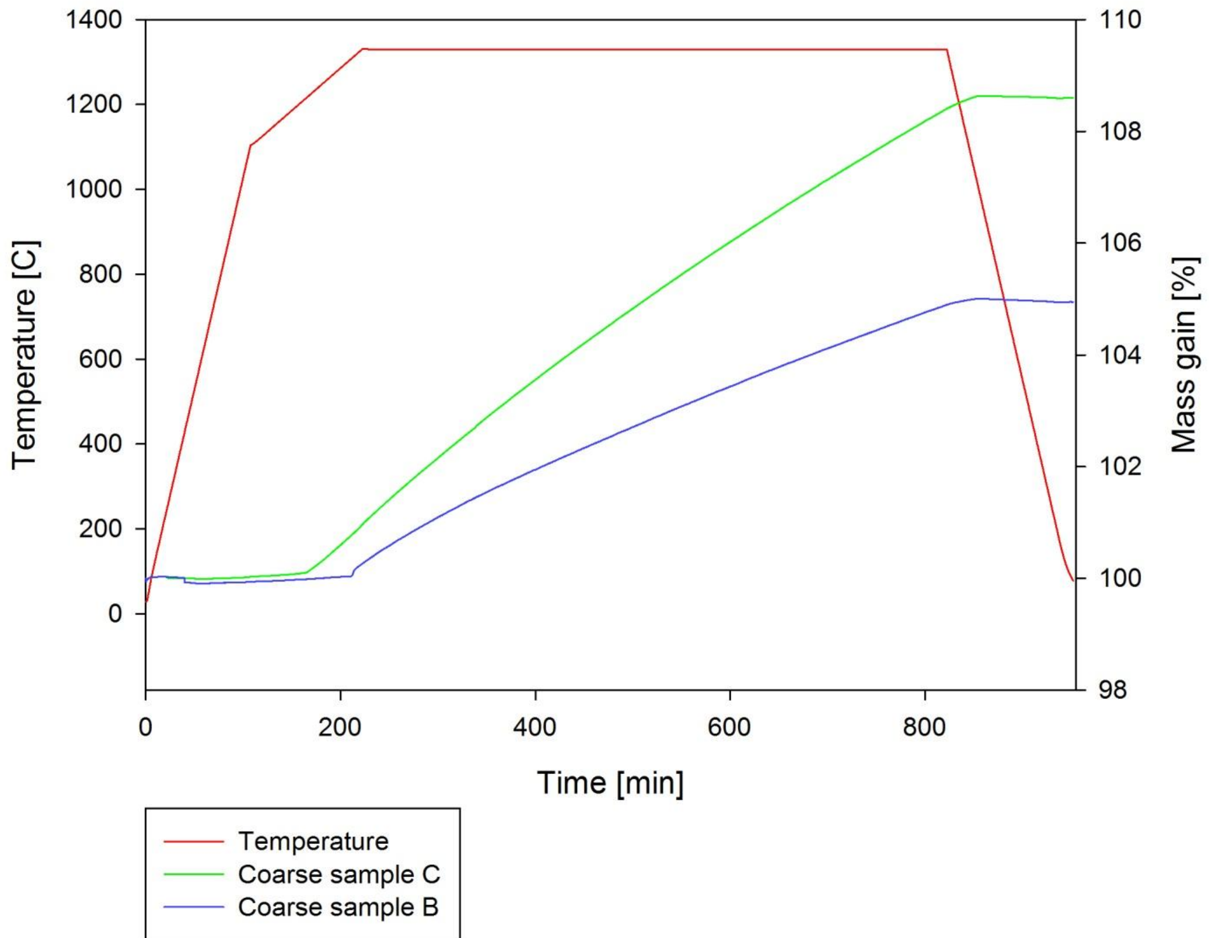

Figure 4.4: TGA results from coarse sample B and C run 2, taken June 2014. The onset of stage 1 is clearly visible: B) at 1310°C and for C) at 1215°C. No visible transformation into stage 2 for sample C, but estimated at 1330°C, 5 min into the isotherm. For sample B stage 2 seems to occur at the same temperature as stage 1. The difference between the mass gained by the two samples is notable.

4.1.4 Summary

Table 4.1: Summary of weight before and after the TGA run. Weighing was done on a separate weight from the TGA apparatus:

Run nr and sample name	PSD	Start weight [mg]	End weight [mg]	Weight increase [%]
Run 1 Sample B	0.2-0.8 mm	80.53	82.26	2.1
Run 2 Sample B	0.2-0.8 mm	79.23	83.13	4.9
Run 1 Sample C	0.2-0.8 mm	79.05	81.54	3.1
Run 2 Sample C	0.2-0.8 mm	79.73	86.56	8.6
Fine A dry	<75 µm	81.21	92.26	13.6
Fine A moist	<75 µm	80.27	88.11	9.8
Cu Hi	<200 µm	80.23	99.99	24.6
Cu Lo	<200 µm	79.96	97.12	21.5

Table 4.2: Overview of the onset of the different stages in the different samples:

Run nr and sample name	PSD	Temperature stage 1 [C]	Temperature stage 2 [C]
Run 1 Sample B	0.2-0.8 mm	1280	1310
Run 2 Sample B	0.2-0.8 mm	1310	1310
Run 1 Sample C	0.2-0.8 mm	1220	1300
Run 2 Sample C	0.2-0.8 mm	1215	1330 + 5 min (est.)
Fine A dry	<75 µm	1280	1330 +40 min (est.)
Fine A moist	<75 µm	1330	1330+40 min (est.)
Cu Hi	<200 µm	n/a	n/a
Cu Lo	<200 µm	n/a	n/a

Data from table 4.1 is in agreement with data from the TGA plots. From the table 4.1 it is evident that the C sample has the higher weight increase compared to sample B, especially in run 2, but much lower compared to the smaller grain sizes with higher surface area.

The Cu doped samples gained almost twice as much mass compared to the pure samples, A dry and moist. The data shows that the moist sample had less mass gain than the dry sample.

The onset of stage 1 varies between the samples. Stage 1 for sample C is in close proximity to the melting point of $FeSi_2$ (1212°C), and stage 1 for sample B and dry sample A are close together, even though the particle size distributions are different.

4.2 Observations of the crucible after nitridation

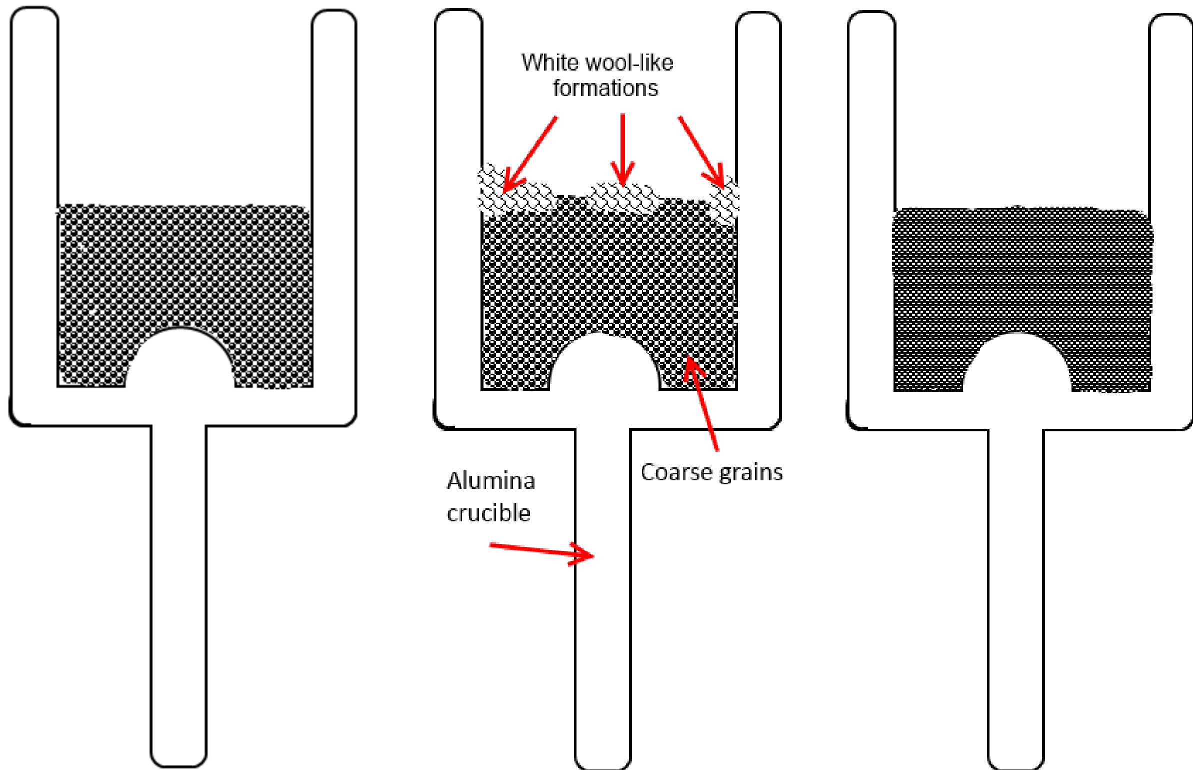

Figure 4.5: Cross section illustration of the alumina crucible. Left: Before nitridation and also after nitridation of stage 1 of both samples. No visible changes to the surface. Middle: Both stage 2 and 3 of both samples showed large spots of white wool-like formations, which also grew upwards along the walls. Right: Cu samples completely sintered and with a very thin, almost transparent, white layer. The moist pure fine powder A showed a thin gray surface with a hint of whiskers along the crucible wall, much like the illustration to the left.

Figure 4.6: Top view of wool-like formations on the surface and upwards (i.e. only the grains at the very top was clad in this wool-like formation) of the sample. This picture is the same illustrated in Figure 4.5.middle, sample coarse C.

4.3 SEM

4.3.1 Sample B

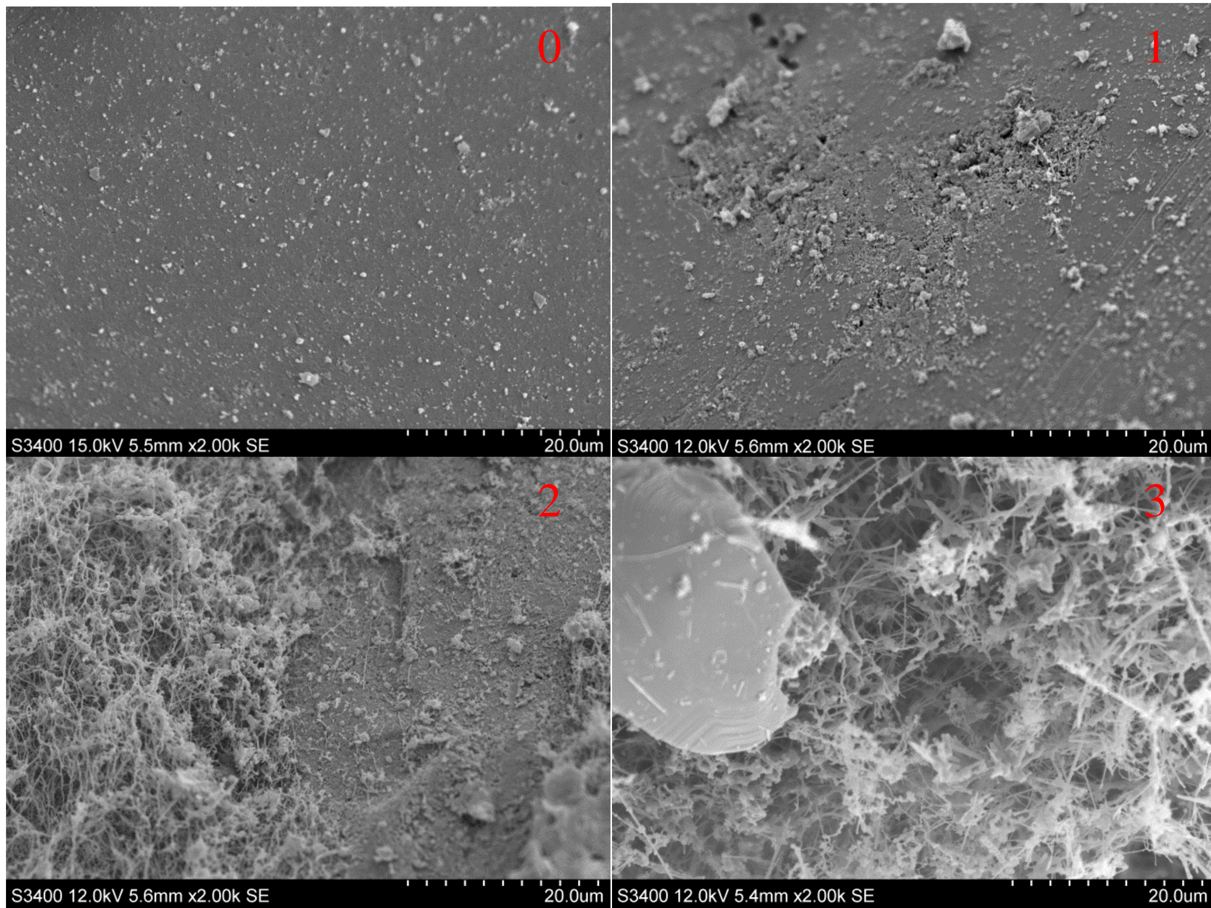

Figure 4.7: Sample B pictured at different stages in the nitriding process; 0) The precursor as-received 1) stage 1 at 1280°C 2) stage 2 at 1300°C and 3) stage 3 at 1330°C after 10 hours.

The fine and somewhat smooth surface of as-received sample B develops trench like cavities from evaporation and surface diffusion to the activation sites up to stage 1, as seen in Figure 4.7.1 above. Between stage 1 and 2 there is a massive formation of wool-like whiskers (thickness ca 300 nm) on certain surfaces, while other surfaces only exhibit the previously mentioned cavities. After the complete run of the program, defined as stage 3, the wool-like structure is so massive that it is difficult to see the surface, as if it was a very dense forest. Longer, straighter, whiskers are also visible. The large smooth surface in Figure 4.7.3 is recognized as an Al_2O_3 particle from EDS.

4.3.2 Sample C

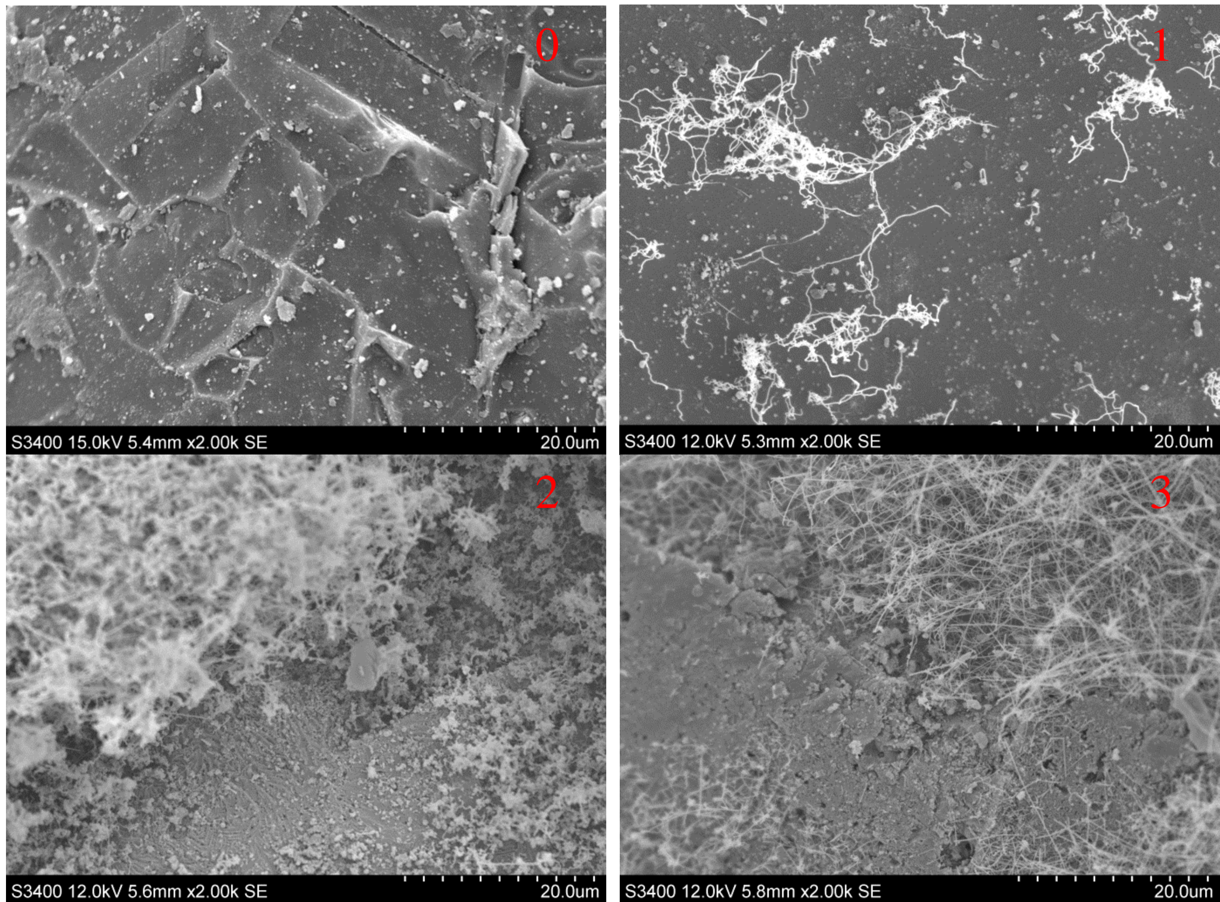

Figure 4.8: Sample C pictured at different stages in the nitriding process; 0) The precursor as-received 1) stage 1 at 1220°C 2) stage 2 at 1300°C and 3) stage 3 at 1330°C after 10 hours.

The as-received sample C has not gone through the final chemical treatment step as sample B, c.f. Figure 3.1, which leaves it more rough and edgy. In stage 1 the wool-like whiskers (thickness ca 300 nm) appear growing outward from the surface, and at every origin of these whiskers, there is a particle. This will become clearer in the next section. In stage 2 there is a dense wool formation on one side, while the other side mostly consists of trench formation with the occasional deeper pits visible as black spots in Figure 4.8.2. At the last stage longer and straighter whiskers becomes dominant. These whiskers grow more along the surface, and not necessary directly outwards of the surface plane. The surface not covered in whiskers is recognized as Al_2O_3 by EDS.

4.3.3 Comparing B and C

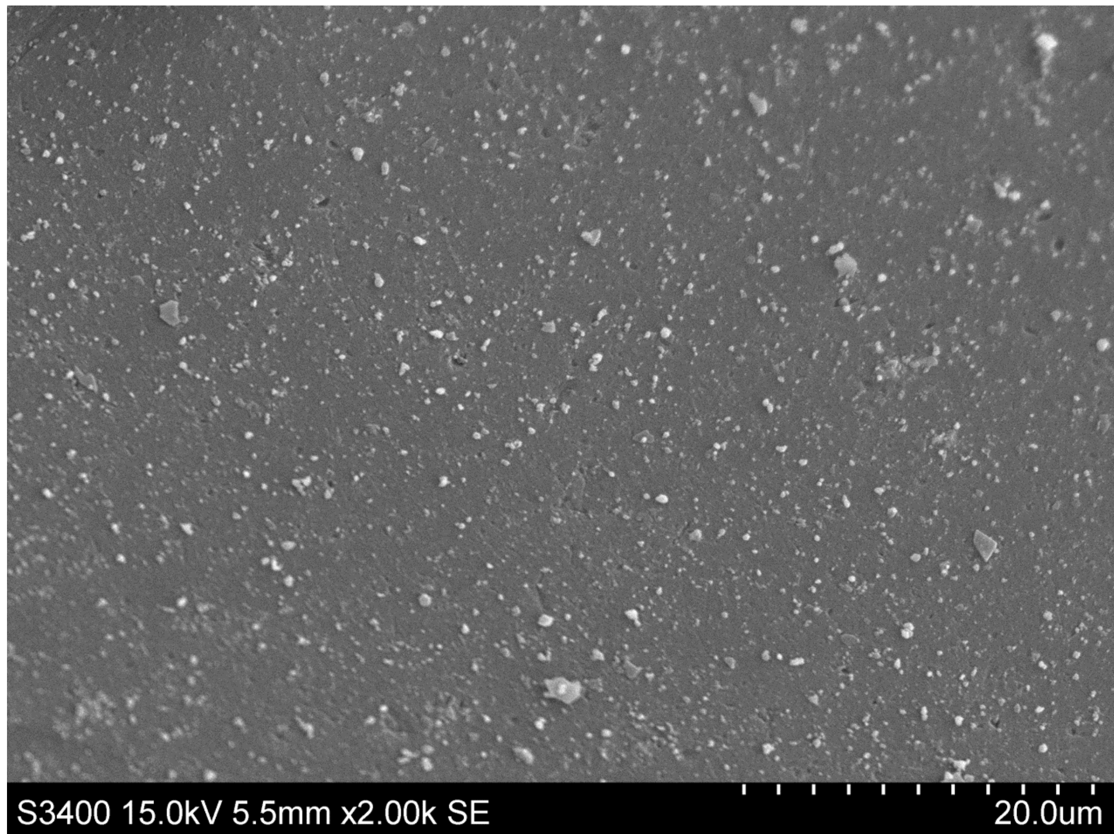

Figure 4.9: Sample B as-received. Specs of Si-dust on the surface.

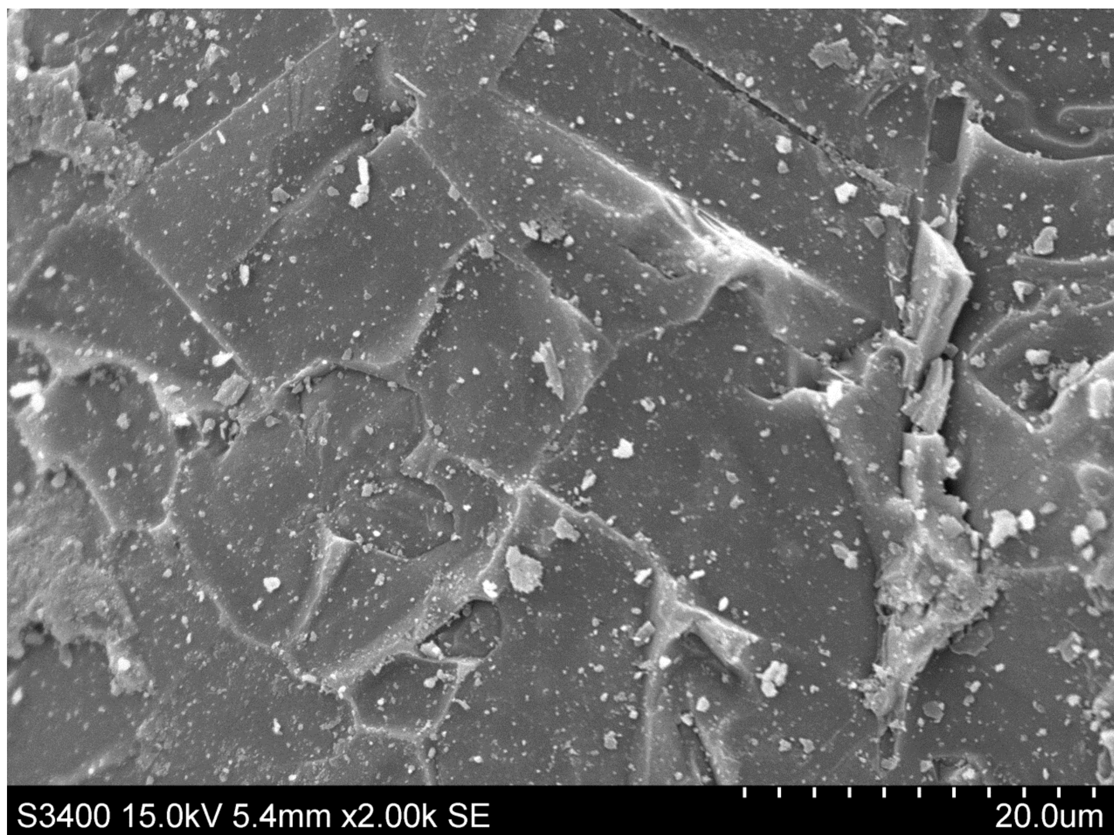

Figure 4.10: Untreated sample C as-received. Specs of Si-dust on the surface.

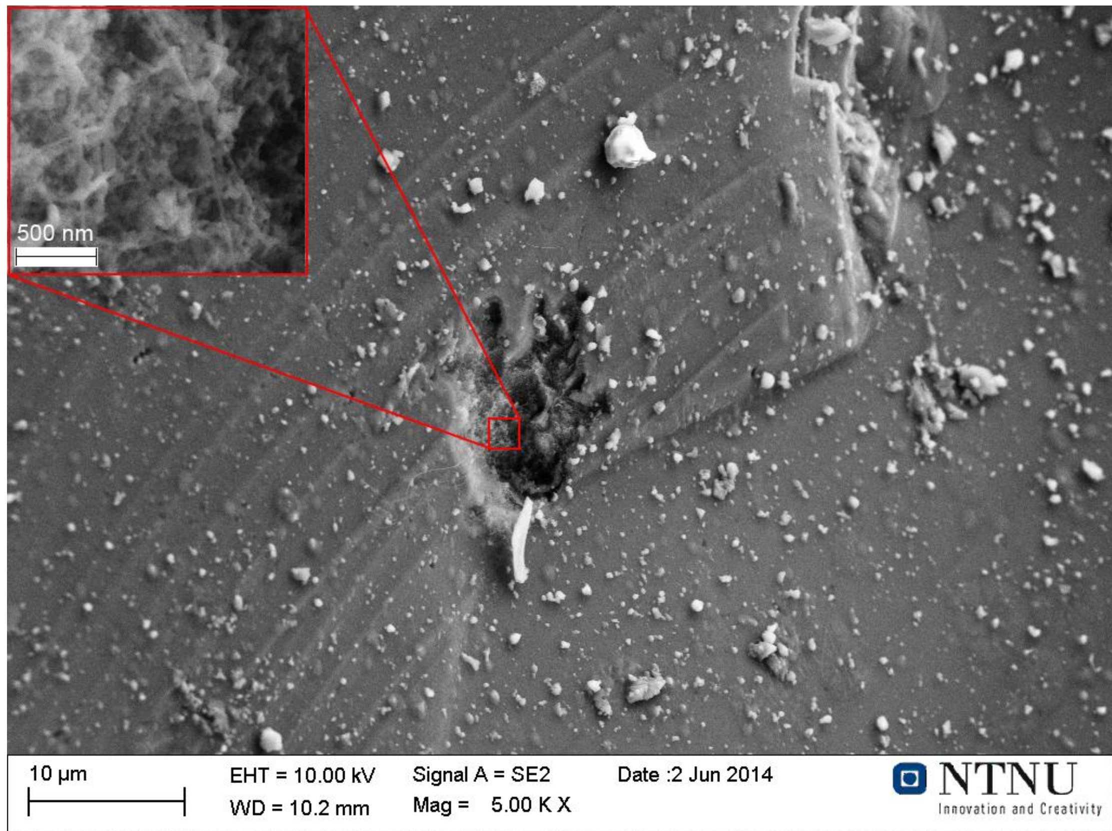

Figure 4.11: Sample B1 at 1280°C. The onset of cavity formation. Whiskers and spheres observed inside the cavity. Granules of inter-metallic particles on the surface.

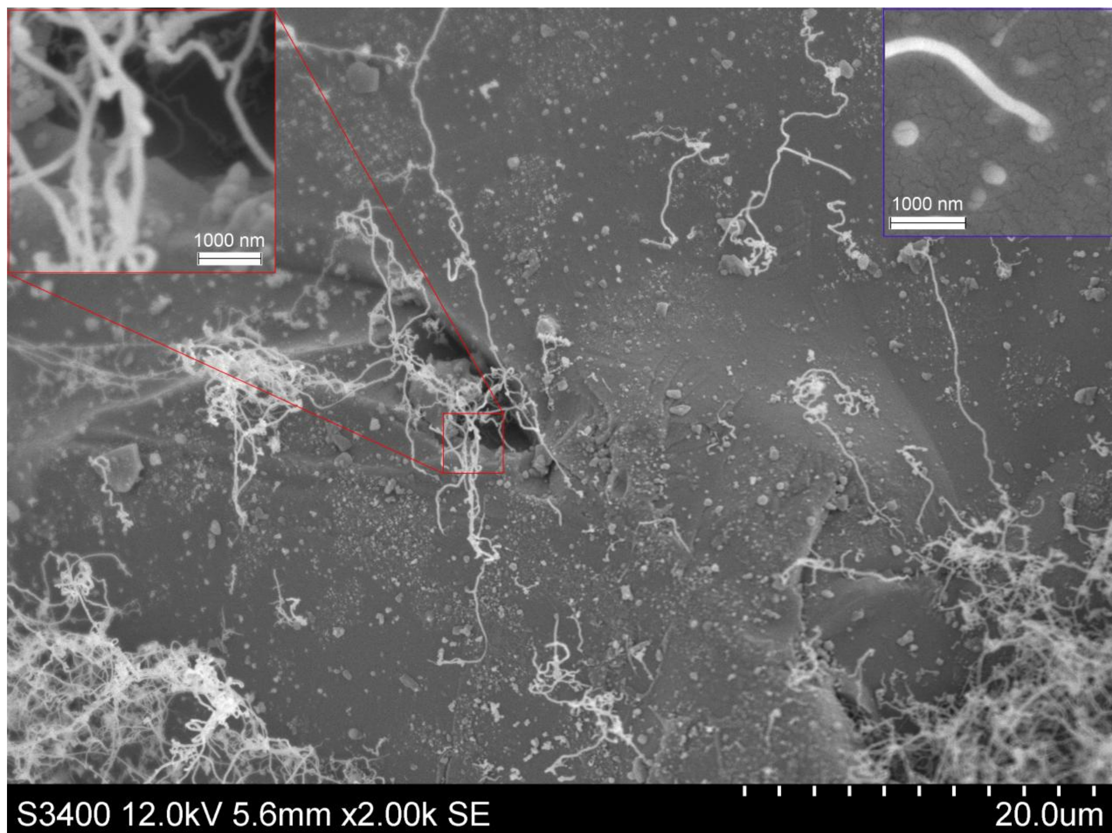

Figure 4.12: Sample C1 at 1220°C. Granules of inter-metallic particles on the surface acts as seeds to form wool-like whiskers by surface VLS reaction, magnified in the blue image.

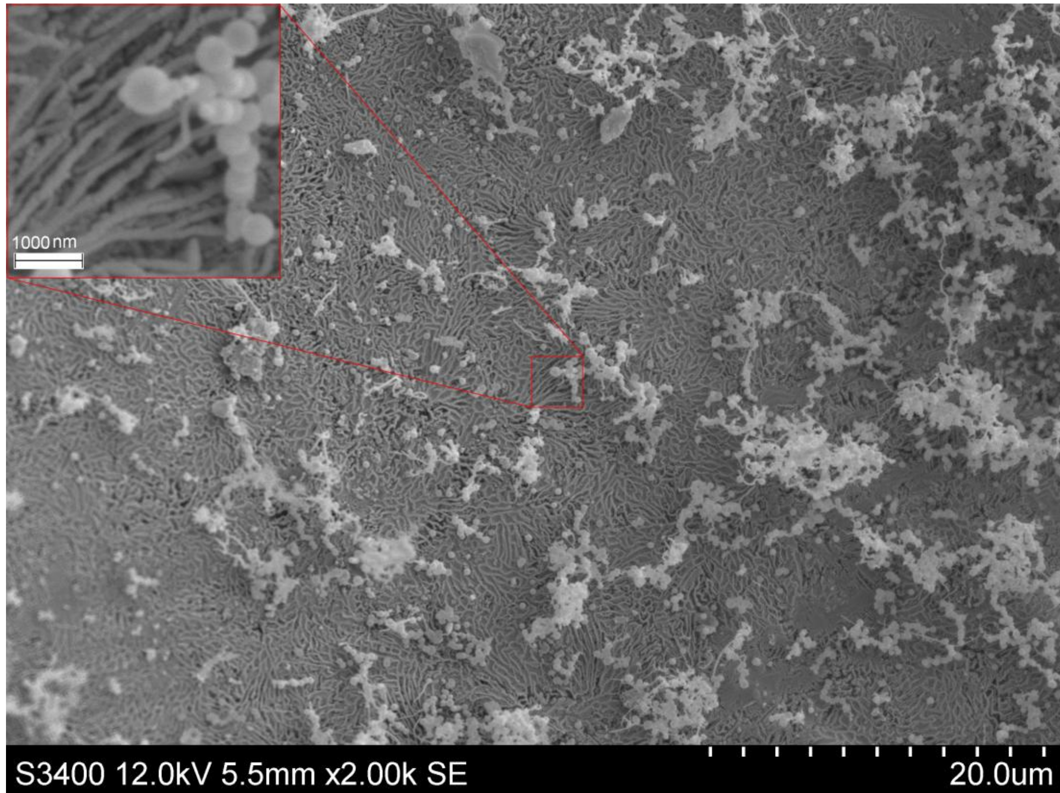

Figure 4.13: Sample B2 at 1300°C. Massive trench cavity formation with wool-like whiskers growing out of the surface. Spherical formations attached to the whiskers.

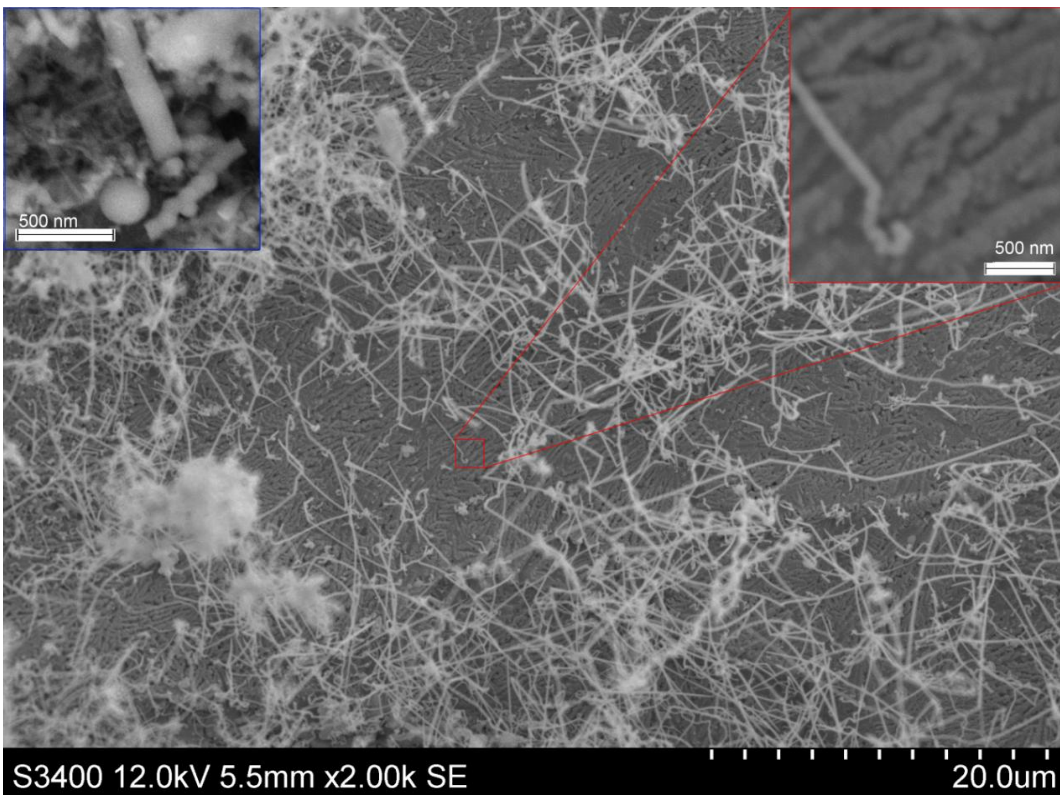

Figure 4.14: Sample C2 at 1300°C. Trench like cavities on the surface, forming dendrittes, seems melted together in some places. Formation of straight whiskers as well as the wool-formation. Blue inset: Higher magnification from a different grain inside a trench, rod and spherical particle.

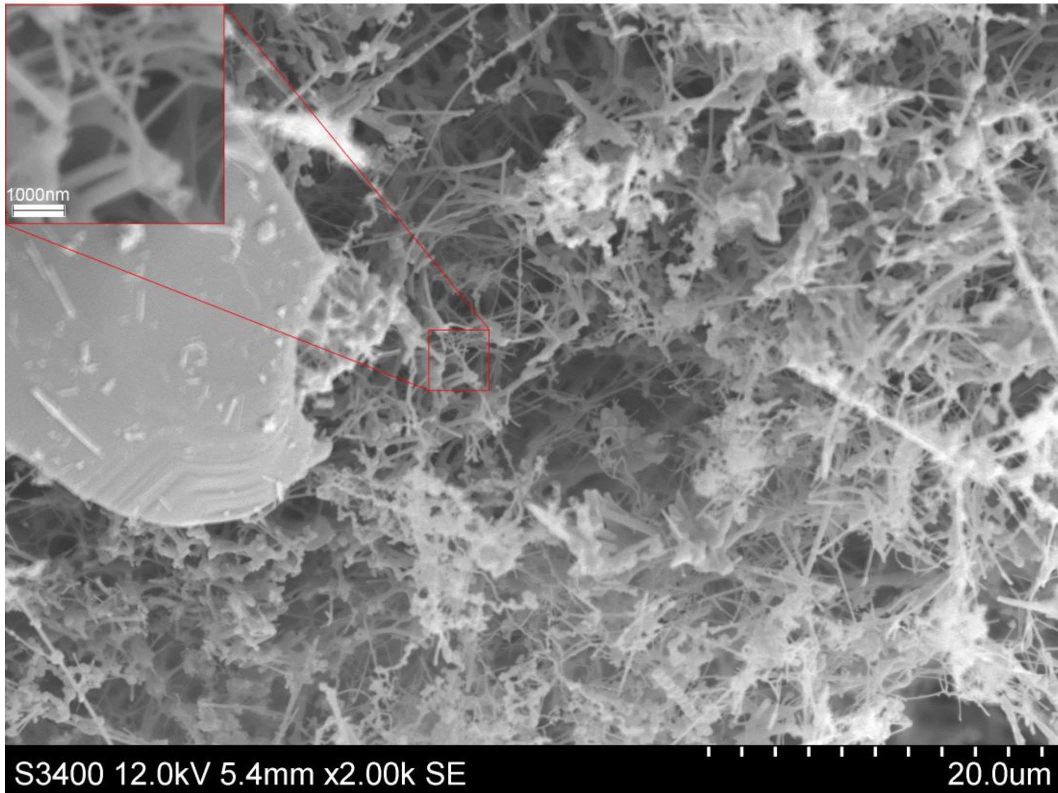

Figure 4.15: Sample B3 at 1330°C after 10 hours holding time. Branched whiskers of primarily wool-like, but also the occasional straight. Large particle is Al_2O_3.

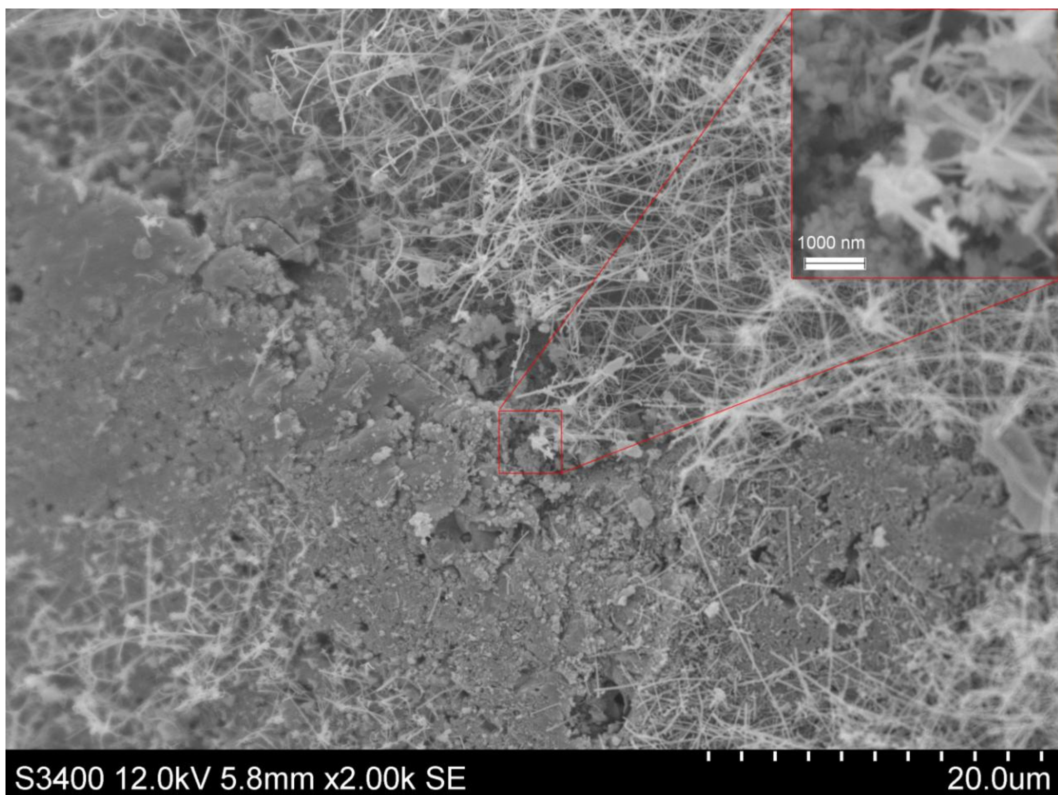

Figure 4.16: Sample C3 at 1330°C after 10 hours holding time. Branched whiskers of primarily straight ones, but also the occasional wool-like. Area of non-whisker is Al_2O_3. The granules, seen to the upper left in the magnified image, is α-matte.

4.3.4 Chosen cross section images

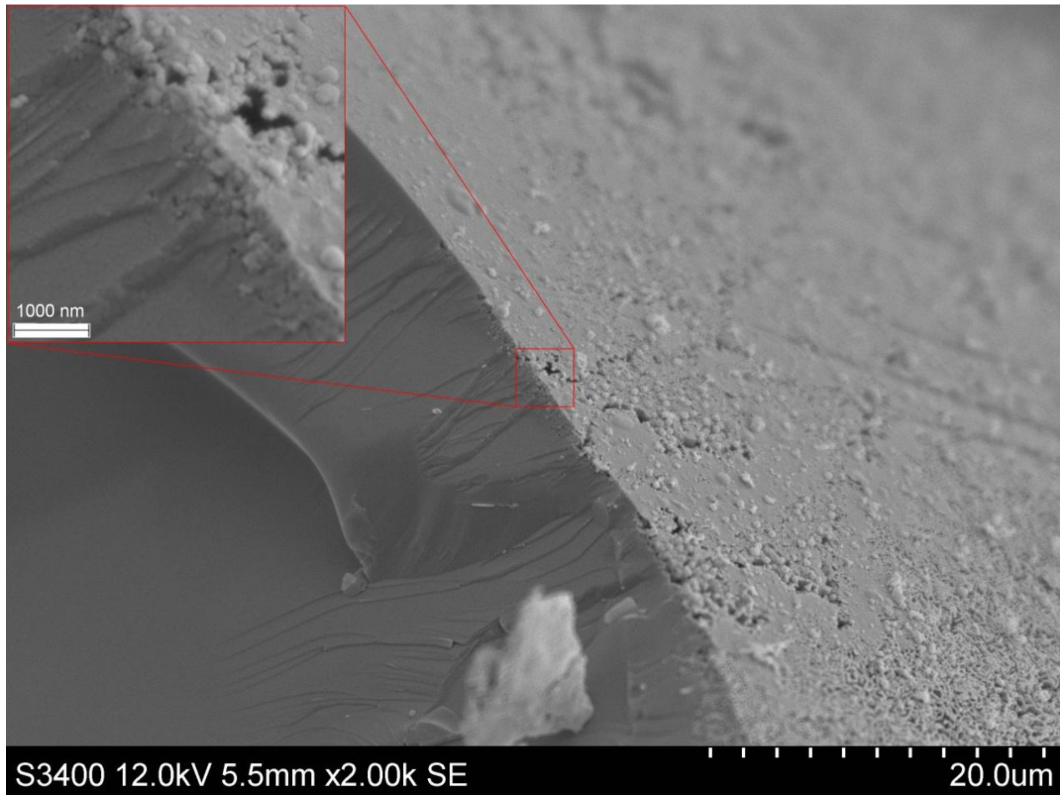

Figure 4.17: Sample B2 cross section. Observe trench formation and nano pores on the surface, and the channels going into the bulk on the cross section.

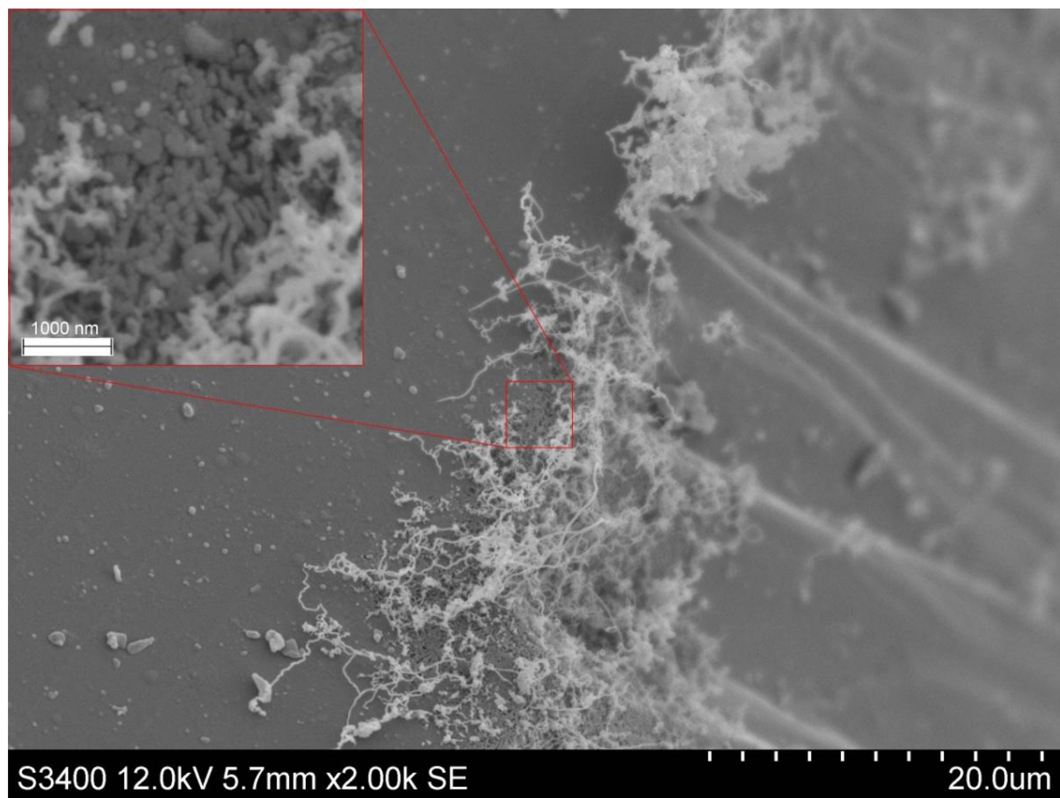

Figure 4.18: Sample C2 cross section. Notice wormlike formation from the surface into the bulk.

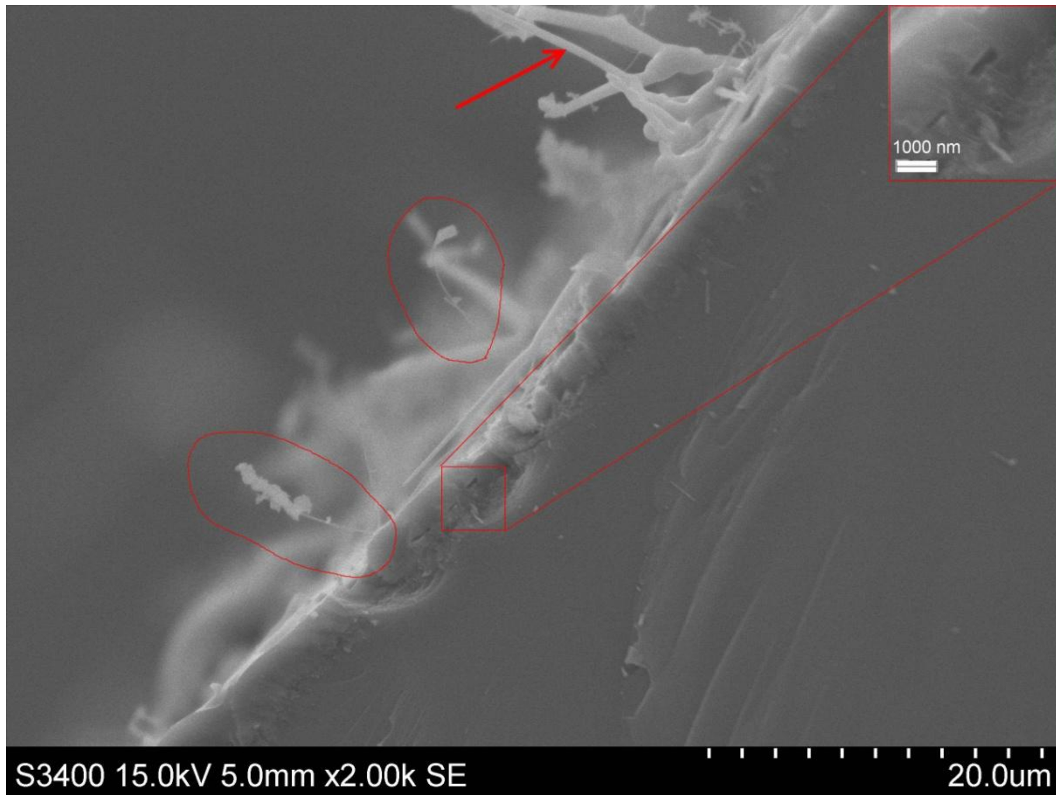

Figure 4.19: Sample B3 cross section. Few pores, but growth of perpendicular formations to the surface into the bulk. Observe the condensed material at the tip of the very tiny whiskers, marked by the red circles, and the thickening of the whisker stem, marked by the red arrow.

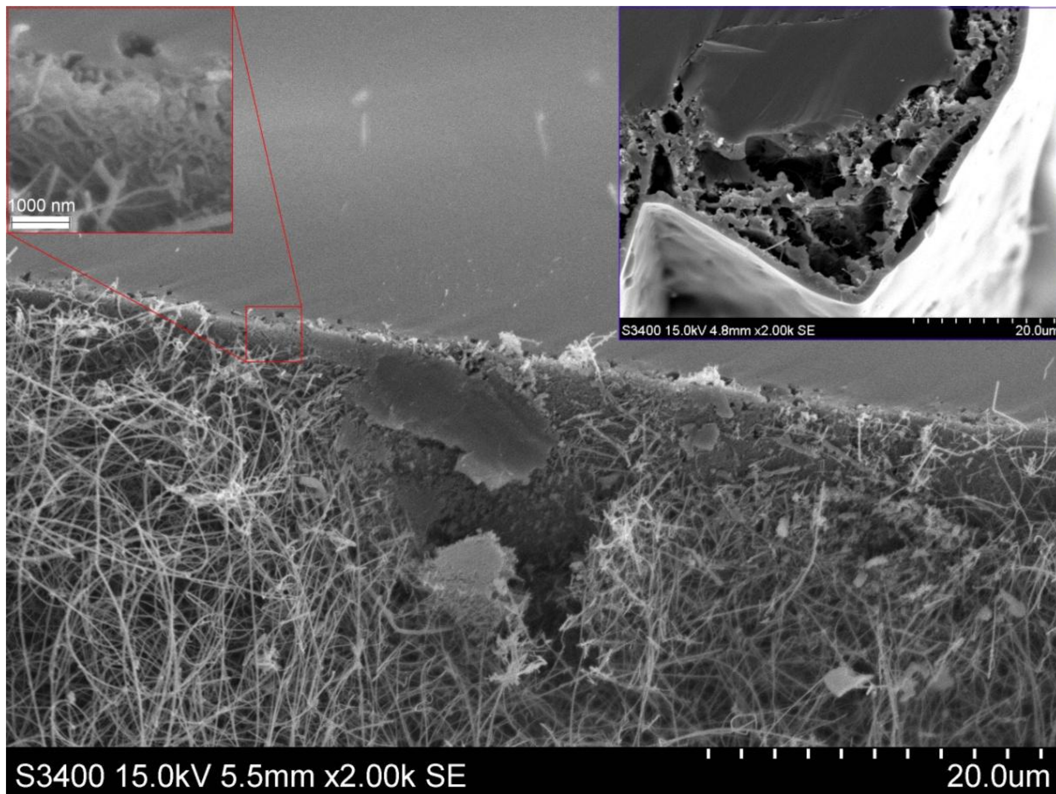

Figure 4.20: Sample C3 cross section. Notable pore size beneath the surface. Notice the change in grayscale from the pores into the bulk. The blue inset is a sample showing extreme pore formations beneath a dense surface. Note the crack propagation into the bulk.

4.3.5 Summary

Table 4.3: Overview of the SEM images of sample B and C.

Sample ID	Whiskers	Special note
B as-received	None	Smooth surface
C as- received	None	Coarse surface
B1	Nano-scale inside cavity	Reaction sites inside cavity
C1	Wool-like	Reaction sites on particles on the surface
B2	Wool-like	Whole surface covered in trench-like cavities Channels from surface into the bulk
C2	Wool and straight	Trench-like cavities, some melted together Wormlike formations beneath the surface
B3	Wool, occasional straight	Very dense forest of whiskers, smooth Al_2O_3 particles Condensed material on nano-scale straight whiskers
C3	Straight, occasional wool	Dense forest of whiskers, smooth Al_2O_3 particles Notable pore size beneath the surface

4.4 BSE images and EDS

4.4.1 Selected images

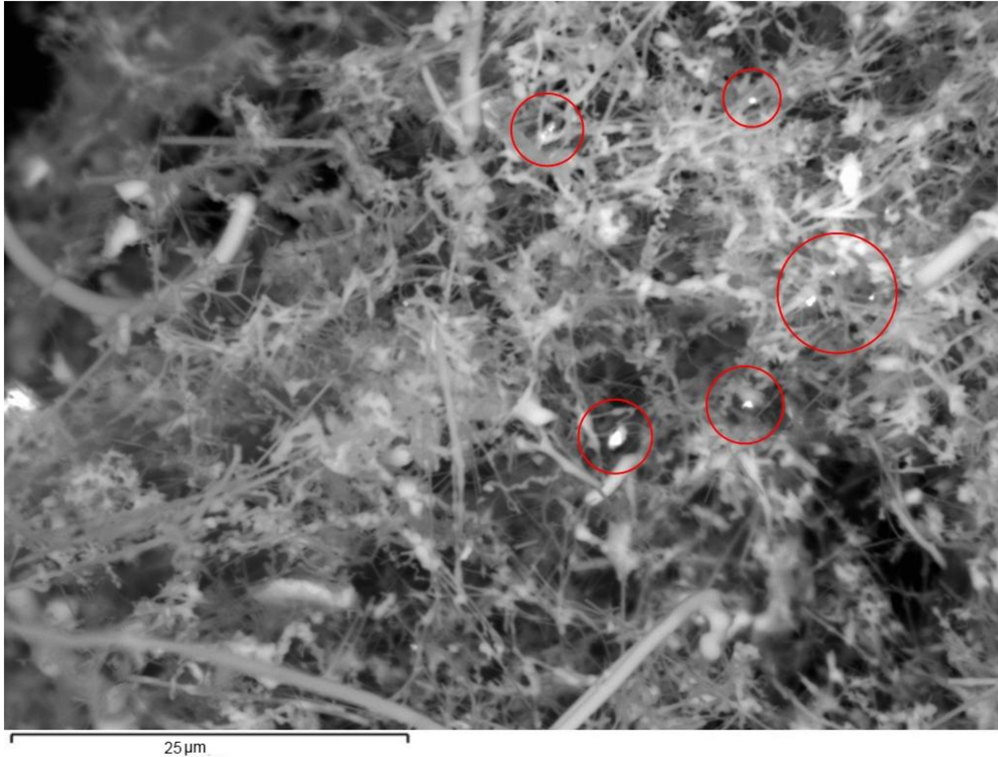

Figure 4.21: BSE image of sample B3. The red rings mark heavy elements at the end of some whiskers.

Figure 4.22: EDS image showing the concentration of iron in the same area as Figure 4.21.

Even with low iron detection, it is possible to see at least two of the rings in Figure 4.21 and Figure 4.22 overlap each other, proving that the tip of some whiskers contain iron.

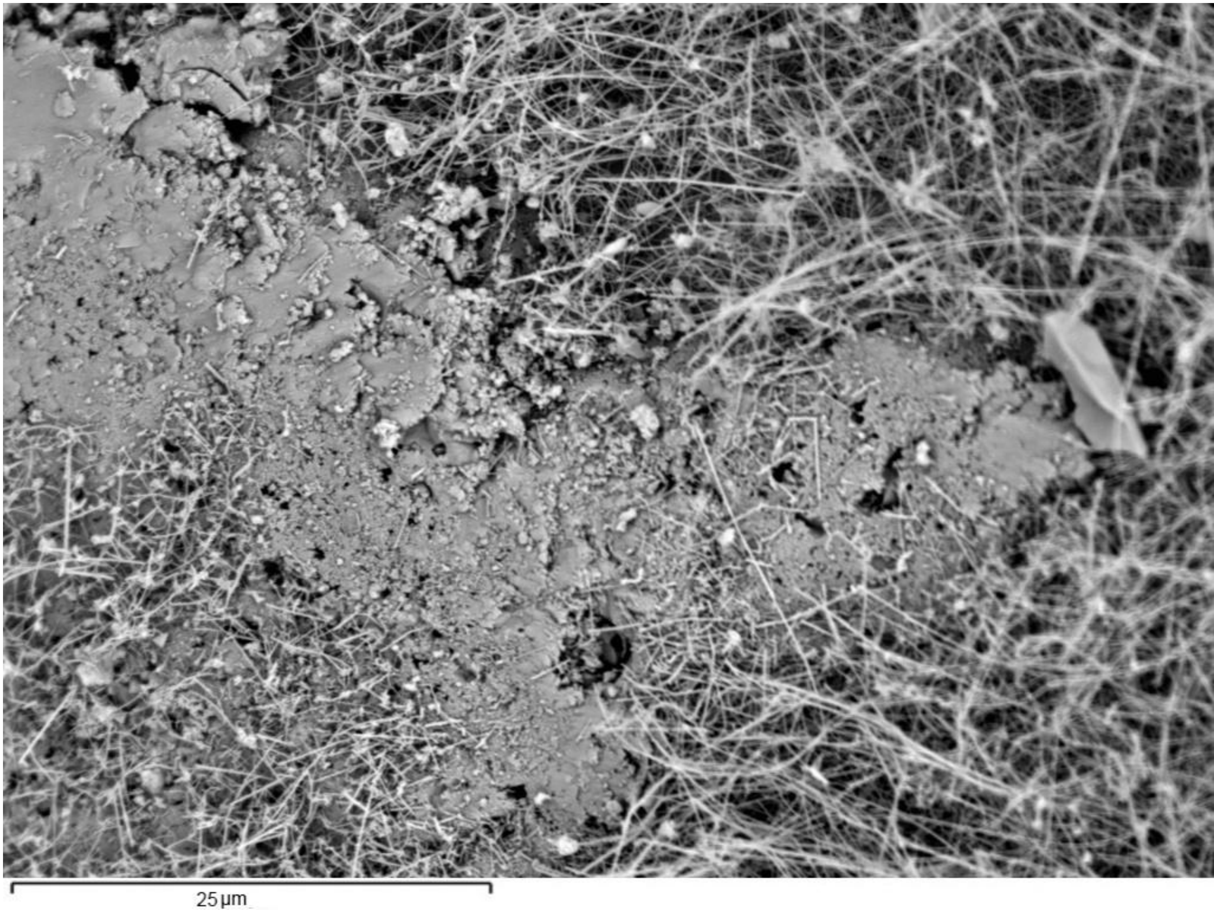

Figure 4.23: BSE image of sample C3. Area of Al_2O_3 surrounded by a forest of whiskers.

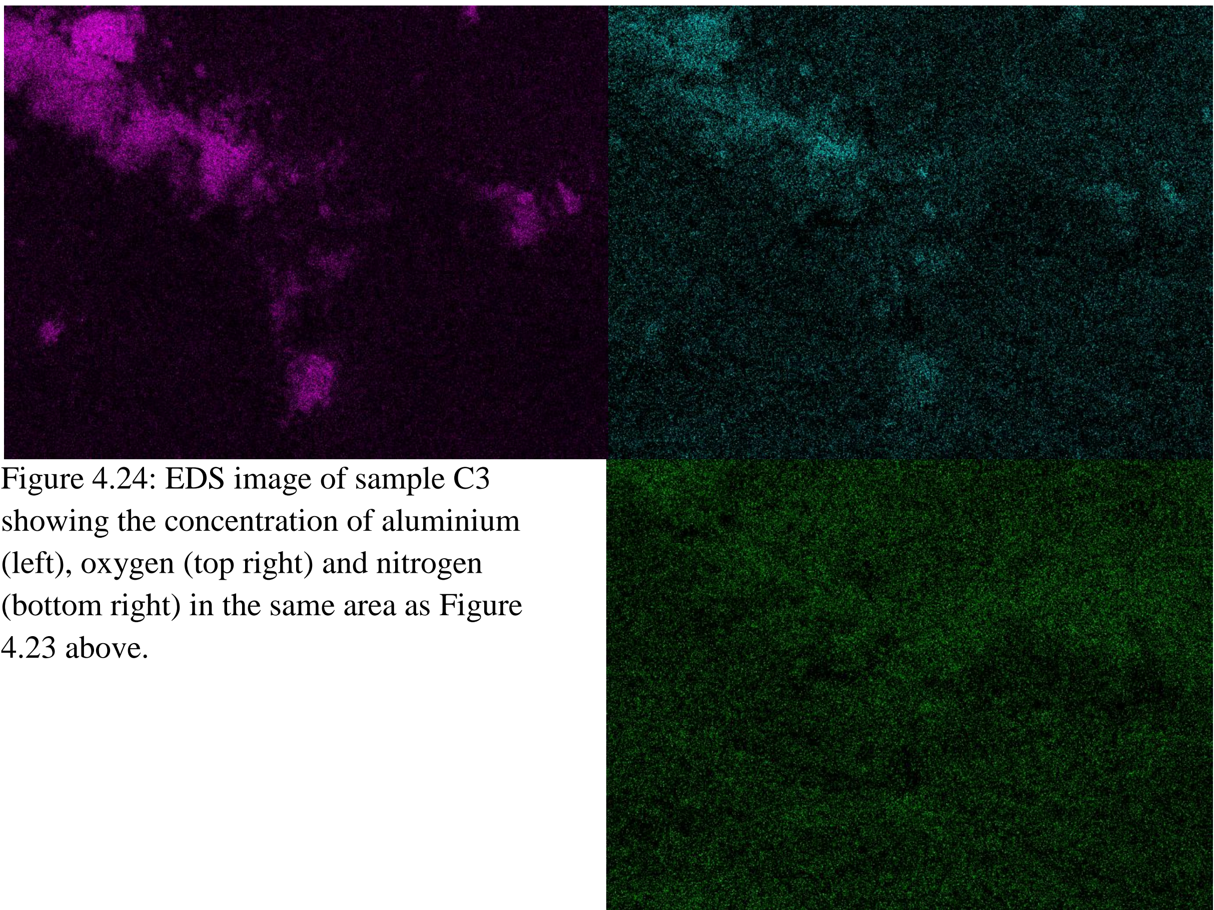

Figure 4.24: EDS image of sample C3 showing the concentration of aluminium (left), oxygen (top right) and nitrogen (bottom right) in the same area as Figure 4.23 above.

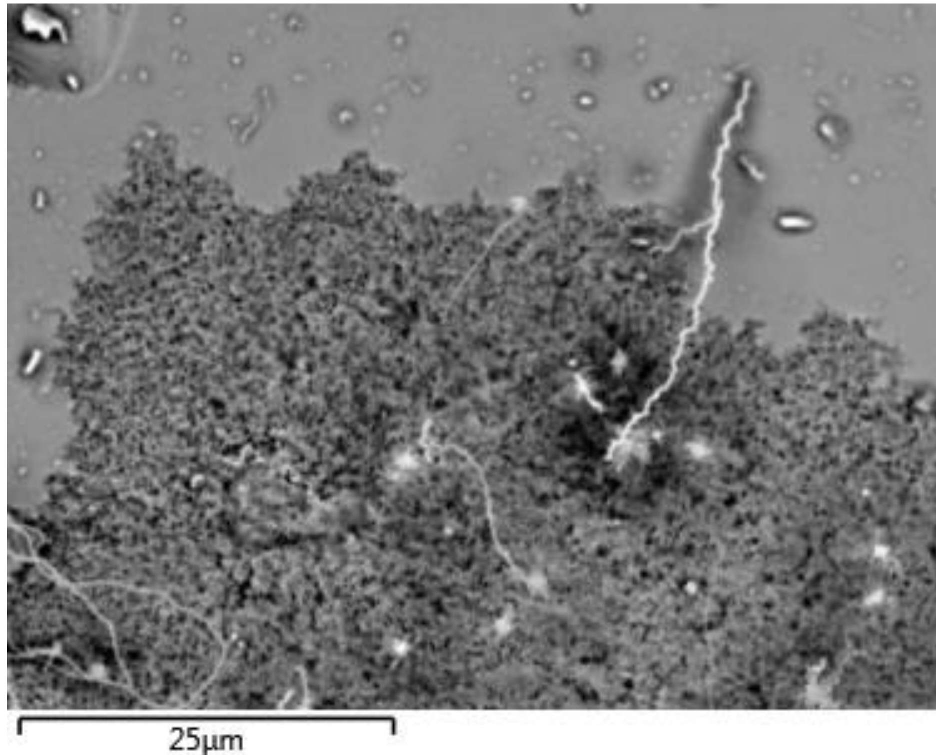

Figure 4.25: BSE image of sample C2. Cavity trench formation in the surface. Black spots indicate deeper pits. Growth of whisker originated from a particle in the surface. Same phenomenon, minus the whiskers, has been observed for the B2 sample.

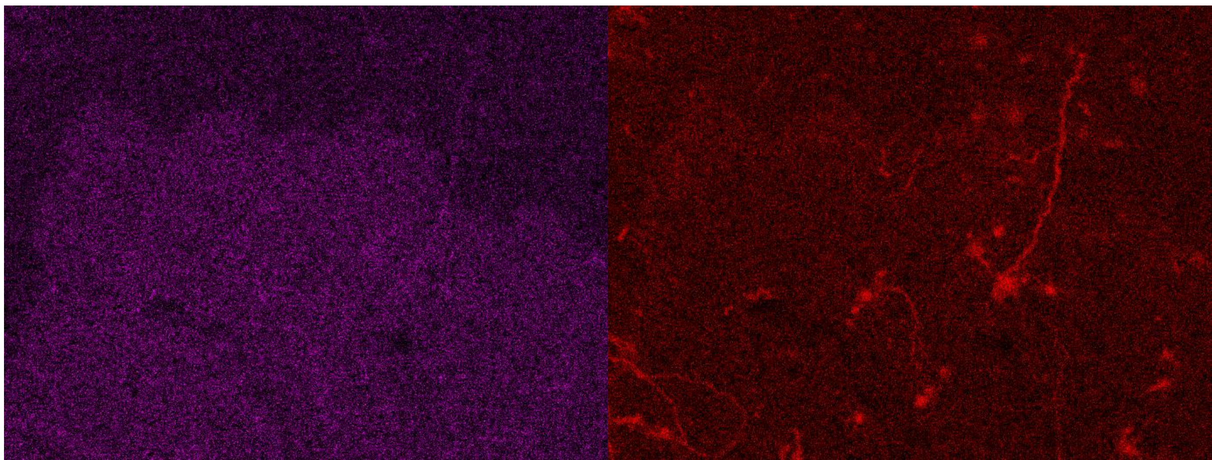

Figure 4.26: EDS image of sample C2 showing the concentration of nitrogen (left) and oxygen (right) in the same area as Figure 4.25.

4.4.2 Summary

Due to the setup and quality of the apparatus it is not possible to achieve a higher resolution, which means it is difficult to separate specific structures and phases from each other.

The EDS results at least indicate that: The nitrides originates from reaction sites (mostly inside the cavities), some of the whiskers have an iron containing terminus, there is no AlN and only Al_2O_3 and the whiskers consists of silicon, nitrogen and especially oxygen c.f. Figure 4.26.

4.5 XRD

4.5.1 XRD plot sample B3 with and without the top layer

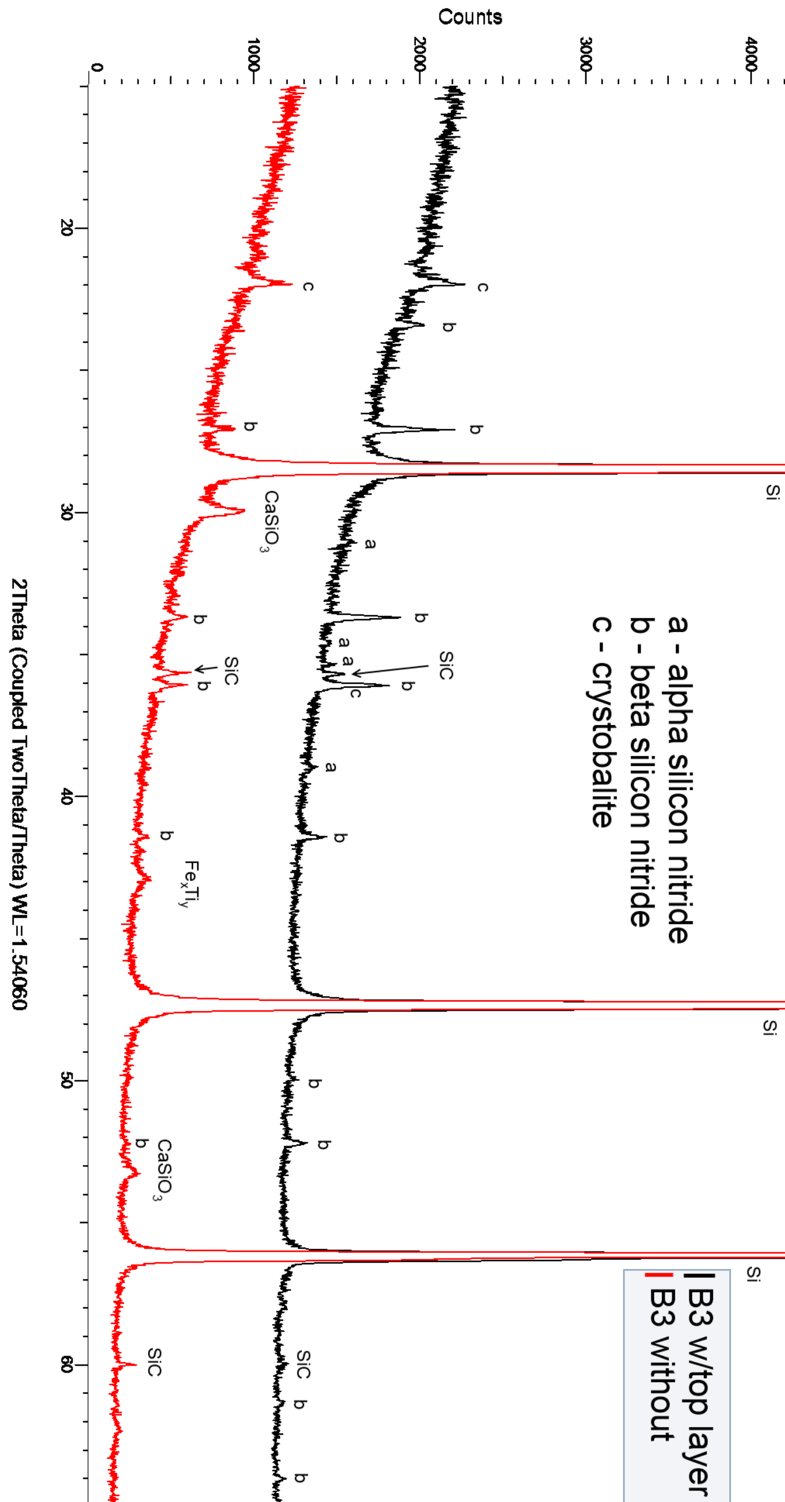

Figure 4.27: XRD plot of sample B3: With (black) and without (red) the top layer. Mark: Significant lower counts of β- and no detectable α-Si_3N_4 in the sample without the top layer, and also the negligible different in cristobalite. The presence of $CaSiO_3$ in the sample without the top layer must be regarded as a contamination of the sample.

4.5.2 XRD plot stage 2 and 3

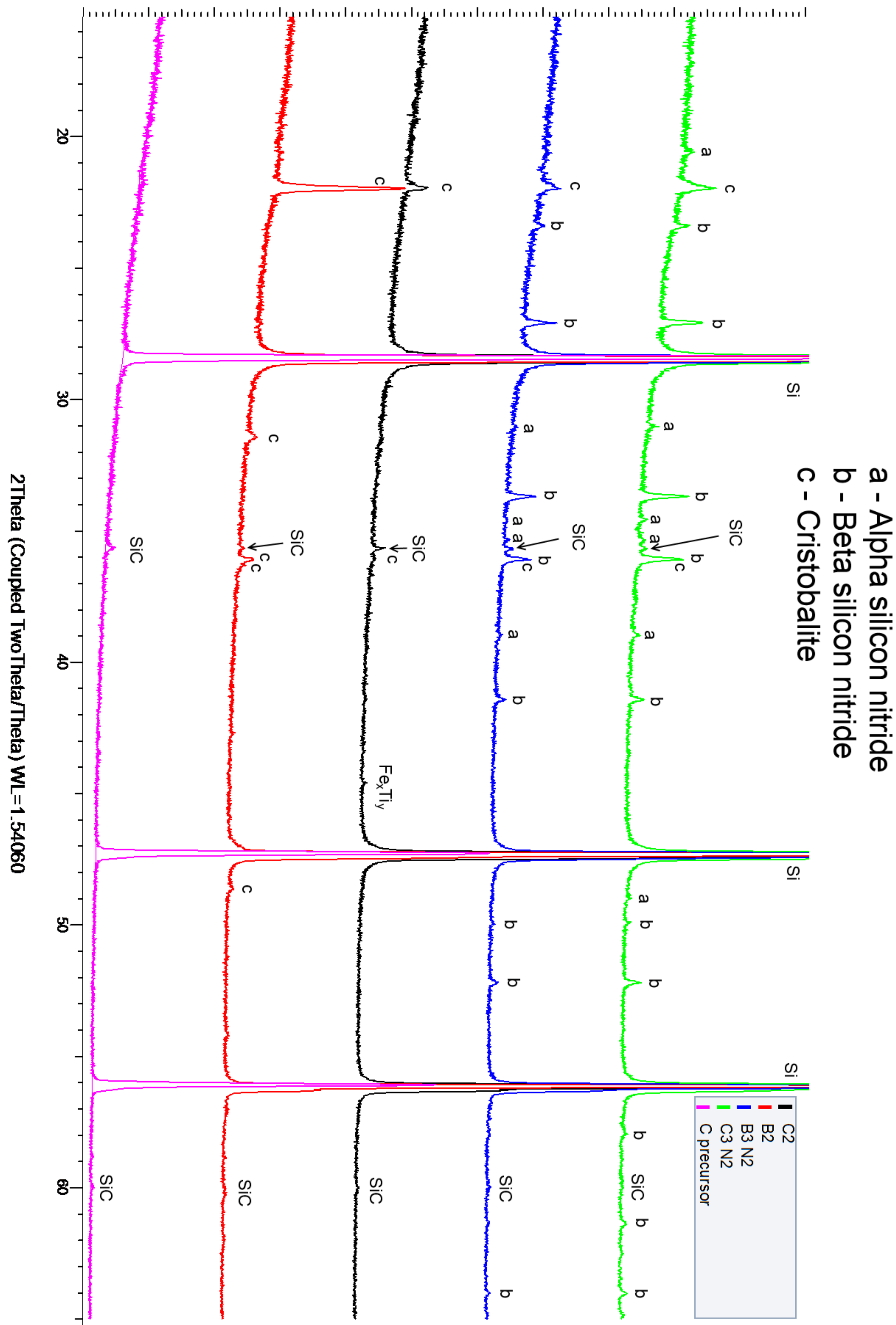

Figure 4.28: XRD plot of the different samples beginning from the C precursor up to sample C3. Note the significant cristobalite counts in sample B2 and no development of neither α- nor β-Si_3N_4 before phase 2. At stage 3 it looks like sample C has converted most of Si, which is in agreement with table 4.1. The amount of SiC from the precursor remains stable throughout the nitridation process.

4.5.3 XRD plot Cu Hi and D

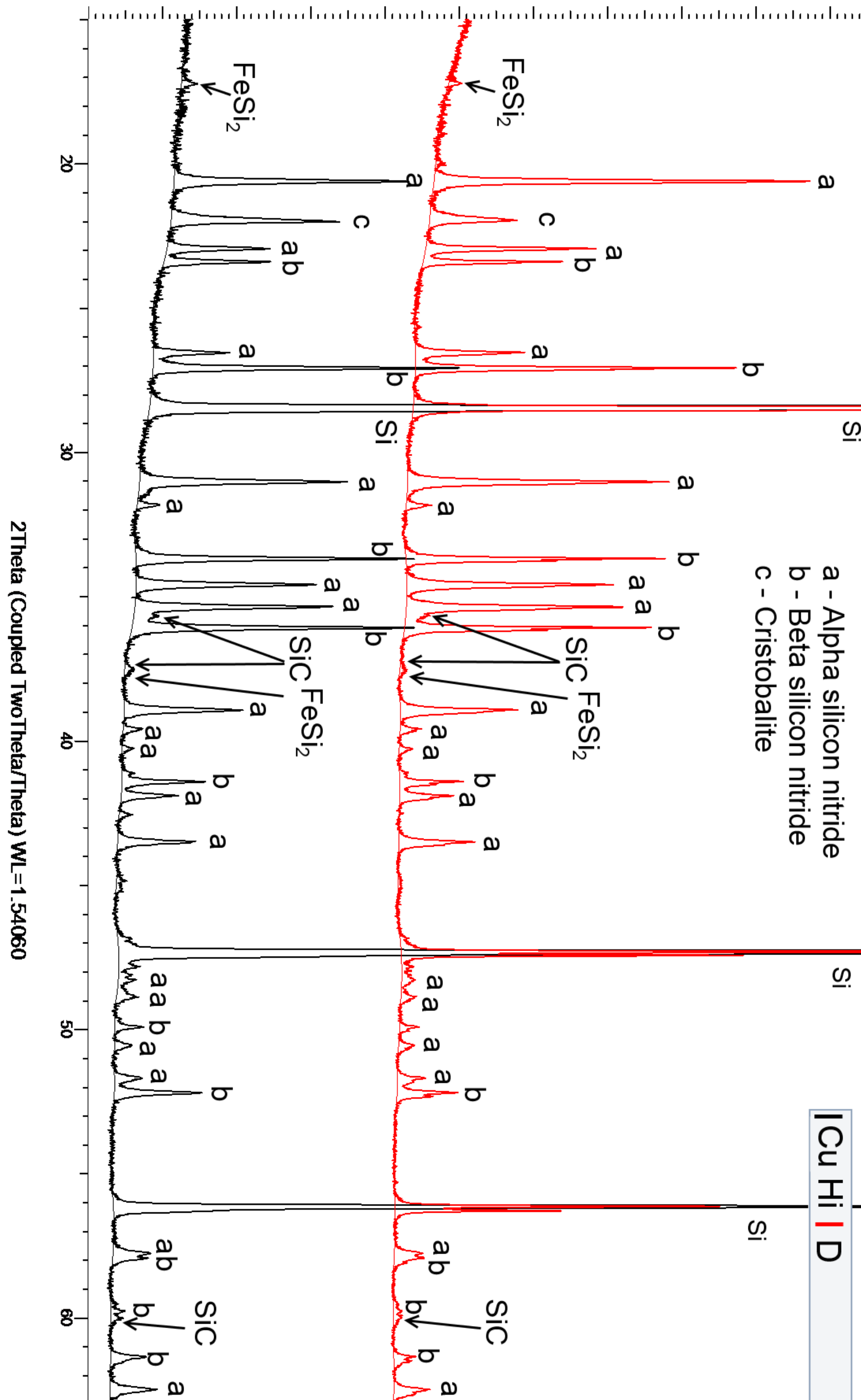

Figure 4.29: XRD plot of sample Cu Hi against sample D made by Hem 2013 [7], which is of the impurity content, but of different PSD.

Sample Cu Hi and sample D made by Hem 2013 [7] are practically identical in phase composition.

4.5.4 Summary

The XRD plots give a good indication of phase distribution in the sample, but will not in this case give an exact composition and the counts should only be used as a guideline.

Figure 4.27 shows a lower amount of silicon nitrides when the top layer has been taken away, and the complete absent of α-Si_3N_4 but no visible change in cristobalite. The presence of $CaSiO_3$ is not present on any other samples.

Summary of Figure 4.27 and Figure 4.28 is presented in table 4.4 below.

Table 4.4: Overview of the XRD plots stage 2 and 3, with sample C as-received as reference.

Sample ID	α-Si3N4	β-Si3N4	Cristobalite	SiC	Other phases
C as-received	n/a	n/a	n/a	-	n/a
B2	n/a	n/a	++++	-	n/a
B3	-	++	++	-	n/a
B3 no top	n/a	+	++	-	Fe_xTi_y + $CaSiO_3$
C2	n/a	n/a	++	-	Fe_xTi_y
C3	+	+++	+++	-	n/a
Cu Hi	+++++	+++++	++++	-	n/a

n/a Not available, too amorphous or too few crystals to be detected.
- Only trace amounts, i.e. barely detectable
+ Easily detectable, but otherwise low amounts
++ Higher amounts
Etc.

The as-received sample B is similar to sample C. Cu Lo is practically identical to Cu Hi.

4.6 Special case

4.6.1 Silica free exposed surface

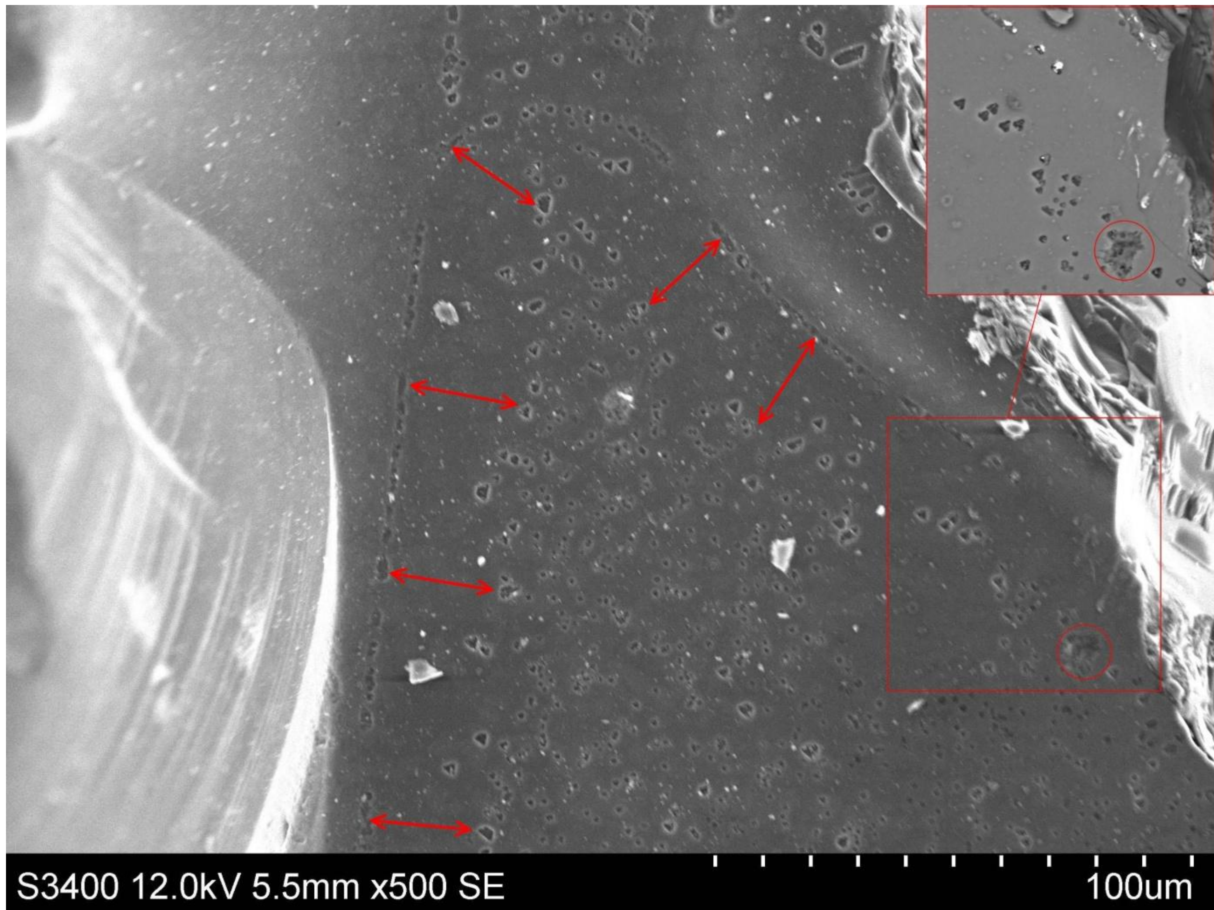

Figure 4.30: Sample B1 at lower magnification. This phenomena was only observed on a single grain of all the grains that were investigated; Triangular formations with the same orientation. The red input image is of the same area at the same magnification, but with BSE to better see the collection of heavier elements, along the crack propagation. The cavity inside the rings is the same kind observed in Figure 4.11. The red arrows mark a depletion layer of roughly 20µm.

This special case is of a grain of sample B1. By the looks of Figure 4.30 a piece of the silicon grain has fallen off during the nitridation program due to stresses caused by a heavy element seen along the crack, and exposed the inner surface to the environment. This (then) silica free surface started immediately to reacted by forming cavities with specific crystal orientation, c.f. section 2.6.6. However, there is a depletion zone, marked by red arrows, which extends roughly 20µm, meaning there were no inter-metallic particles inside this region. EDS of the same area detected no other elements, besides silicon and oxygen, inside the triangular formations. The heavy element seen as bright spots, inside the crack, is iron.

4.6.2 Highly magnified morphologies

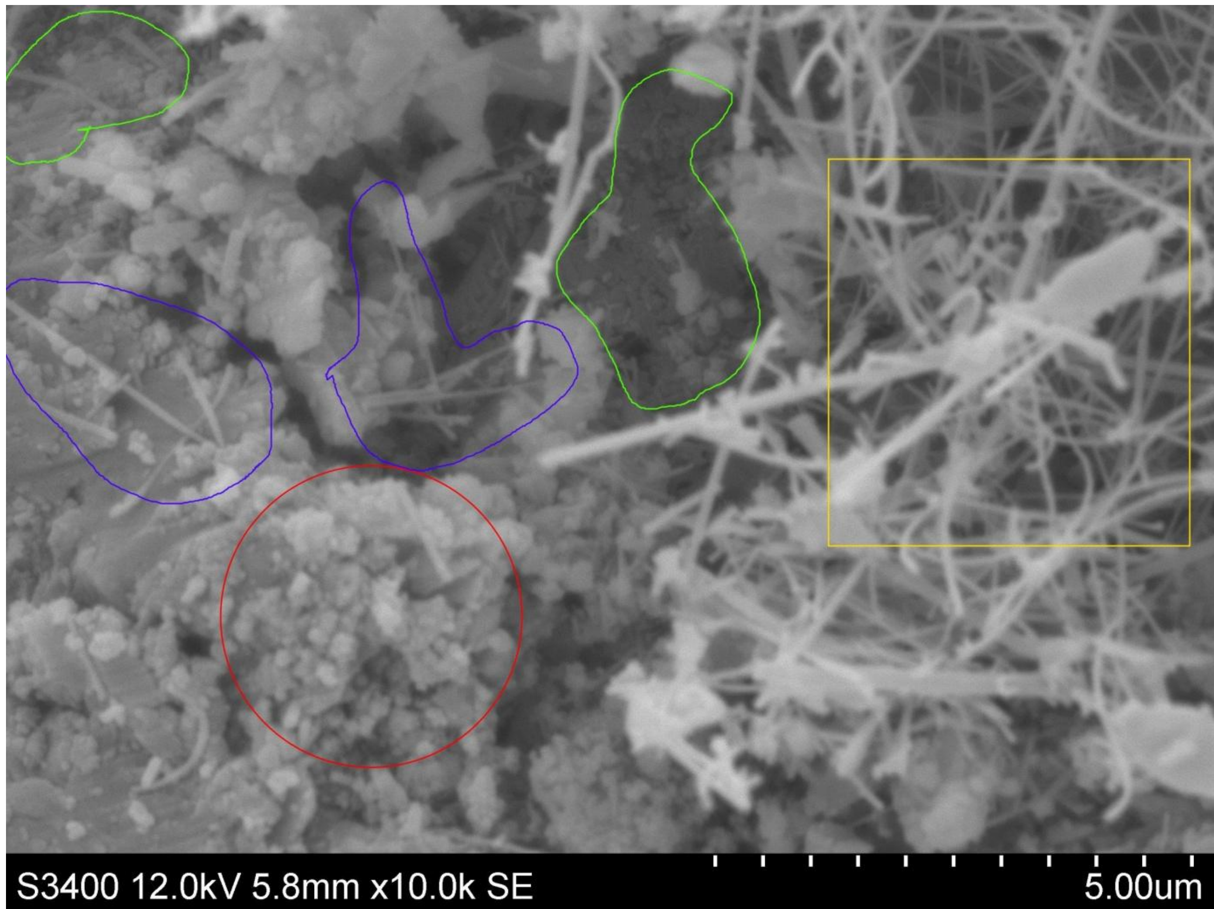

Figure 4.31: Highly magnified sample C3. Red: Formation of α-matte. Blue: Formation of α-needles (whiskers). Green: Formation of β-matte. Yellow: Growth of larger whiskers.

In the magnified image, Figure 4.31 above, there are four different morphologies all together within the space of ca 100μm^2. The phase composition of the thicker whiskers is not known, as EDS apparatus used does not have high enough resolution. The other phases are described in detail in section 2.3.

5 Discussion

In this section the results posted in the previous section will be discussed. Beginning with an explanation of the morphologies and their growth mechanisms before comparing the different samples against each other with respect to the different parameters (impurities, grain size and storage conditions), but first a few remarks regarding the quality of the data.

Especially the data from the TGA must be considered critically; The difference between the curves of the two runs are significant. Possible sources for this error are inhomogeneous sample batches due to small sample sizes or impure gas intake. Most likely it is a contamination inside the reaction chamber, that is; Unwanted elements attached to the crucible holder, which evaporates during heating and causes false weight loss during the background run with empty crucible and this manifests as false weight gain during the actual run. The end mass gain data did, however, match the data from weighing before and after nitridation on a separate weight, listed in table 4.1, which means that whatever parameter change that disturbed the TGA curves also greatly affected the nitridation process overall. The geometry of the crucible is also worth mentioning. The wall of the crucible is relative high to prevent condensation of SiO_x on the inside of the TGA reaction chamber, meaning that the evaporation of silica as SiO(g) will not escape the reaction zone, which is visible in Figure 4.6 were a large portion of the sample's surface is covered in what is most likely SiO_2(s) condensed and grown from the alumina crucible wall. This will give an unwanted bias towards high partial pressures of SiO(g) which is not representative on an industrial scale, and might explain the very low amounts of α-Si_3N_4.

SEM images used are representative for the whole sample if not otherwise stated. Even though each grain is in a way unique, the trend shown in the image still applies on the rest of the grains. Note that this is only true for the topmost layer of the sample, as the lower levels are not exposed to the same parameters (especially partial pressures) as the top layer, c.f. Figure 3.5.

Gathering data from EDS is difficult considering that the surface is not flat and consist of mostly whiskers at later stages making the topography even rougher and not all surfaces are in focus. This, combined with very small morphology structures and deep electron penetration to give stable images, makes it very difficult to determine the precise phase and structure of the material in question. EDS results are therefore only used as a rough guideline to determine what elements are present, given that the concentrations are high enough to see clearly.

The XRD plots seem to be of high quality and very precise. Even with monochromatic waves removing reflections it is still impossible to detect pure amorphous phases. In the case a possible phase is completely amorphous, not estimated by EDS images, seen on SEM images or explained in the theory, it will remain hidden and therefore not discussed in this report. The likelihood of that happening is considered slim.

5.1 Determining the structures

The whiskers seen in many of the SEM images consist of two main branches, called wool-like and straight, based upon their visual appearance.

The first type grows from a seed and seemingly at random out of the surface, Figure 4.12. The seeds are most likely $FeSi_2$ liquid phase droplets that acts as a catalyst in a VLS process described in section 2.3, Figure 2.9.I. The random growth behavior can be explained by the location of the seed is at the surface, and the weight of the whisker and the gradient of reactant gases moves, so the tip of the whisker moves in the most favorable direction, as illustrated in Figure 2.11. This also means that the whisker is non-crystalline and will not show on XRD plots, unless it crystallizes at a later time or higher temperature.

From the EDS images, Figure 4.26, it seems these wool-like whiskers contains both nitrogen and a fair amount of oxygen, in addition to silicon. This would indicate a silicon-oxy-nitride as Si_2ON_2 from the diagrams in Figure 2.17 and Figure 2.18, but from the partial pressure diagram Figure 2.16 the P_{SiO} at 1330°C over SiO_2(s,l) is just 10^{-9} atm, given that the nitrogen gas feed contains 10^{-8} atm oxygen, which is within reason. This is not high enough to stabilize Si_2ON_2, even with the contribution of SiO(g) evaporated from underlying silicon grains. Another argument is the concentration of oxygen is far higher than nitrogen, and given the stoichiometry of the silicon-oxy-nitride it is fair to rule out Si_2ON_2. The final argument is no detection of this phase in the XRD plots, but this might be because the phase is completely amorphous.

An indication of what phase and structure this whisker type consist of is given in Figure 4.19 marked by the red circles: A very tiny and short whisker has its tip covered by a condensed material. This could developed to a fully covered stem, illustrated by the red arrow in the same image. This much thicker whisker would then have covered the whole rigid, crystalline stem, and seem to continue to grow in random directions, just like the wool-like whisker. This might explain the structure and element composition of the whisker; A crystalline α-Si_3N_4 starts to grow from a seed on the surface, but due to high SiO partial pressure, and the lack of available nitrogen as the SiO gas creates a front against the nitrogen (illustrated in Figure 3.5), the vapor to solid growth (Figure 2.9.I) at the tip is retarded and SiO(g) condenses as SiO_2(s) on the VLS growing α-whisker, covering it, and continues to grow outwards. This explains the high oxygen concentration seen in EDS, the nature of the spheres in Figure 4.13 and the difference in whisker stem thickness (α-whisker is much thinner, c.f. section 2.3.1 and Figure 2.10 and results Figure 4.19 and Figure 4.31). The SiO_2(s) is crystallized as cristobalite, c.f. Figure 2.14, and this is detected by a fairly high reading in the XRD plots.

The other whisker type, the longer and straighter, is best seen in Figure 4.14 and Figure 4.20. This does not grow perpendicular outwards from the surface, as the wool-like type does, but more or less along the surface, though not in contact with it. The reason why this type is more straight is explained by the $FeSi_2$ beads at the terminus, seen in Figure 4.21 and the VLS growth again seen in Figure 2.9.II: Since the bead is at the terminus, and not the origin, then the reaction site is moved away from the high P_{SiO} surface. This allows the whisker to continue to grow longer. The occasional branching is explained by deposition of catalyst along the stem, see Figure 2.9.III. The stem is however thicker than that of pure α-whiskers, and also here the SiO condenses and form SiO_2(s) (crystallize as cristobalite) which thickens the whiskers.

The distribution of the two whisker types can be related to the impurities of the samples. This will be discussed more in the next section.

The surface structures in Figure 4.13and Figure 4.14 show massive trench like cavities on the surface. The inset image in the latter shows that the ridges, surrounded by cavities, have a dendritic structure, indicating that it once was liquid. From the BSE and EDS image in Figure 4.25 and Figure 4.26.left, respectively, it is clear that Si_3N_4 is produced in these cavities, and given the liquid nature of the dendrites, it is natural to conclude that these are in fact β-Si_3N_4-matte. This structure is also shown in Figure 4.31, and is similar to Figure 2.5 and the growth mechanisms explained in section 2.2. The XRD plots show that an equal fair amount of β-phase is present in both B and C sample, and given that both samples have the same trench like cavities on the surface, it is safe to conclude that this is indeed the β silicon nitride.

The channels visible in sample B1 in Figure 4.17 are of high interest. The particle density around the openings of the pores on the surface might indicate that they are impurities which originates from deeper within the bulk, but were transported through defects in the silicon crystal to the surface, leaving an open channel for Si(g) to easily migrate through and thus widening the channels.

The channel length of roughly 20μm also coincide with the depletion layer seen in Figure 4.30. This image show the inter-metallic crystal orientation etching effect described in section 2.6.6. The newly exposed silica free surface immediately reacted to the atmosphere, and the particles etched the typical triangular shape for the (111) surface of silicon before they evaporated, as no traces of any element other that Si and O were detected on the surface. This phenomenon was not found on any other grain, and therefore needs more investigation before a good conclusion can be drawn.

The difference between the sample with the top layer included (run 2) and the sample without the top layer (run 1) was emphasized in the XRD plot of Figure 4.27. The sample without the top layer showed no detection of α-Si_3N_4 which is known to form from gaseous phases, while some amounts of β-Si_3N_4 were still detected. This means that the nitrogen must have been transported further down the charge by means of a liquid phase. However, the sample also showed concentrations of $CaSiO_3$ and Fe_xTi_y, which was never detected in any other sample. Combining these two readings it might be possible that the surface layer sealed off the nitrogen from entering and at the same time prevented the evaporation of SiO(g) from escaping. It is still within reason to conclude that the transport of the nitrogen does not penetrate deep into the charge.

Some zones on individual grains have indications of other phases than the ones present here. The main one being Al_2O_3 shown clearly in Figure 4.23and Figure 4.24, but not on any XRD plots and more randomly distributed than homogenously. No AlN phase was detected in XRD nor visual by SEM or EDS, which indicates that the function of Al additives to remove oxygen from the system, but not nitrogen, works perfectly. However, AlN is clearly visible on the whole surface when changing the nitrogen gas flow with pure argon. This is outside the scope of this report, but the results are presented in Appendix D.

5.3 Comparing samples

The images of Figure 4.7 and Figure 4.8 show how the surface changes morphology from start to end. It is evident that the different impurity content between sample B and C affect the growth mechanisms.

The difference is clear already from the as-received samples; Sample B has a smoother surface than sample C, and also containing less inter-metallic impurities on the surface because of the extra chemical treatment. This might be the main reason why the onset of stage 1 varies and is later than compared to sample C. This means the VLS whisker growth right at the melting point of $FeSi_2$ in sample C is not observed in sample B, where the onset of stage 1 is rather marked by the start of cavity growth. This hypothesis is further strengthen by a depletion zone observed in Figure 4.30 and the channels in Figure 4.17, B1 and B2 respectively, and indicate migration of inter-metallic particles. One should not rule out that this migration also occur in the C sample, but is more difficult to observe. In other words; The reaction site for sample B1 is inside the cavities, while the reaction sites for sample C1 is on impurities on the surface.

Between stage 1 and 2 there is a massive surface reaction which covers the entire grain in trench like cavities and whiskers growing out of the surface. This is evident in the rapid mass increase seen in the TGA curve, Figure 4.3. The cavities are essentially similar between the two samples, and the only small difference is that the cavities on the C sample seems to diminish as the dendrites fuse together and closes the pores, seen to the right in Figure 4.14. This is also illustrated in Figure 2.6.C. The slight difference in whisker type distribution between the two samples can be explained by the impurity content: The longer and straighter α-whiskers needs a liquid phase bead at its terminus, while the wool type has a droplet at its origin. The higher iron content in sample C, together with relative much higher impurity content at the surface from the start, might cause better growth conditions for longer whiskers.

The growth of silicon nitride requires the removal of silica from the surface in order for the reactants to combine. As explained in section 2.6.1 iron acts as a catalyst in removing the silica layer, which means that for sample C the growth of whiskers can start immediately after $FeSi_2$ melts, while for sample B the $FeSi_2$ might be located in the surface, rather than on top of the surface, meaning it will begin to develop cavities and β-Si_3N_4 prior to growth of α-Si_3N_4 whiskers. This head-start for sample C is the only visible reason why sample C has a mass increase advantage over sample B in this report.

Why some areas have no whisker growth, observed in Figure 4.7.2 and Figure 4.8.2, might be to because of Al_2O_3 present in the surface, silicon crystal orientation (100-face etc) or grain orientation relative to the surface and nitrogen availability. Further research is required.

The difference between sample B and C at the final stage is mainly the morphology of the whiskers; Sample B has mostly wool-like whiskers, which are much denser than the straight whiskers that dominate sample C. The difference between the two whisker types is previously explained by the location of the liquid phase catalyst, and it seems that sample C, with its higher iron content, mainly produces whiskers with beads at its terminus from stage 2 and onward. On the contrary sample B continues to mainly form whiskers with a droplet at its origin. The dense nature of the wool-like whiskers might also prevent the diffusion of nitrogen to the silicon surface and thereby retarding the nitridation process.

Another, more subtle difference, is seen on the cross section images in Figure 4.18, Figure 4.19 and Figure 4.20; Sample B has only nano scale pores while sample C's pores vary from 1 µm to short of 20 µm containing worm like β-Si_3N_4-matte, which increases pore sizes by Ostwald ripening, c.f. section 2.1. The pores of sample B is on the other hand fused by β-Si_3N_4-rods growing into the silicon crystal, c.f. Figure 2.3 and Figure 2.13.

5.3 Regarding grain sizes

The particle size distribution and the mass gained listed in table 4.1 gives a clear indication that smaller grain sizes have a massive positive effect on mass nitridation of silicon. Even the pure sample A with no additives to enhance nitridation has a huge lead on the coarse samples B and C. As explained in section 2.2, and shown in Figure 2.8, larger grain will have an unreacted core as the nitridation only occurs at the surface of the silicon grain, with a self retarding effect since diffusion through the silicon nitride layer is extremely slow. It is therefore of great importance that the silicon precursor has as large surface to volume ratio as possible.

5.4 Role of storage conditions

Per TGA plot seen in Figure 4.1 it is clear that storage of a pure silicon sample (A) in humid conditions is not favorable in regard to nitridation. The works done by others [44,61] have also investigated nitridation of samples stored in humid conditions but containing iron, which have hidden the real effect of the thickening of the silica layer since iron acts as a catalyst in removing the protective layer, and extra SiO_2(s) might even be favorable because of nitridation of SiO(g) c.f. eq. 20.

5.5 Role of additives and impurities

The role of iron has been explained by forming a liquid phase, $FeSi_2$, above 1212°C, which solves monoatomic nitrogen to form β-Si3N4 or acts as a catalyst in VLS formation of α-Si_3N_4-whiskers. The VLS route have two possibilities: Liquid droplet on the surface or liquid bead at the terminus of the whisker. Both ways are explained in Figure 2.9. The $FeSi_2$ phase is only detected in the Cu samples.

Aluminium is not detected in any phase in the XRD and is either amorphous or has too low crystal counts to be detected. Al_2O_3 is at least seen in EDS images of the surface. The only visible role of Al is to react with free oxygen to hinder the reestablishment of silica layer.

Calcium is only detected by XRD in the B3 sample without the top layer, Figure 4.27. The partial vapor pressure of Ca is very high, and it might have played a role in forming the crystal orientation etched cavities seen in Figure 4.30 before it evaporated and left no traces behind. This is fairly uncertain. In section 2.6.3 it is stated that calcium promotes the α-phase, but since so little α is detected and the quantities of calcium is so low it is not possible to draw any conclusion regarding the role of Ca.

The samples with copper achieved a fairly high mass gain, Figure 4.2, and the two samples were practically identical if not for the complete stop in mass gain of sample Cu Lo minutes before the TGA program finished. The lack of any of the predefined stages in section 3.2.1 but rather a continuously linear growth from ca 850°C can be explained by the liquid Cu_3Si phase at 859°C: At this temperature the kinetics are simply much slower compared to the liquid phase of $FeSi_2$ at 1212°C, which is the definition of the onset of stage 1 by abrupt mass gain. The linear growth might be favorable as it does not apparently seal the reactant off from each other, and the large concentration of α-Si_3N_4 compared to all the other samples gives an indication that this phase continues to grow despite the β-Si_3N_4 favored liquid phases present at higher temperatures.

6 Conclusion

The quality of the data in this report have been sufficient in justifying the arguments in the discussion section of this report. The uncertainties have been pointed out to the reader to make up his or hers own mind.

The main investigation of this report has been between two samples of 0.2-0.8mm in size and different levels of impurities; Sample B with low amounts of impurities and sample C with higher amounts of impurities.

The growth mechanisms investigated in this report are changing during the nitridation program of samples with different properties. The first stage is dominated by the location of the impurities ($FeSi_2$); Impurities *on* the surface gives a wool-like whisker growth, while impurities *inside* the surface gives rise to growth of cavities. The whisker growth at this stage is done by VLS with $FeSi_2$ as a droplet at around 1212°C on the surface, forming α-Si_3N_4.

Because of the high SiO(g) partial pressure the whisker growth is retarded after a short growth and covered by condensed SiO_2(s) which thickens the whisker and gives it the characteristic wool-like structure.

Later stages favors a VLS formation with liquid as a bead at the terminus of the whisker forming straighter and longer whiskers, but this only applies to samples with higher iron content like sample C. Sample B in this report has a lower iron content and continues to mainly form wool-like whiskers throughout the process.

The surface of the samples is rapidly covered in trench like cavities after the $FeSi_2$ forms a liquid phase on the surface. These cavities appear because of surface diffusion and evaporation of Si(g) to reaction sites, where β-Si_3N_4-matte are formed. These cavities might close as the matte develops, sealing off pores beneath the surface. This is especially the case of the C sample where the granules of the matte undergoes an Ostwald ripening. In the B samples the β-matte combines with β-rods and form a denser, almost pore free surface.

Due to the geometry of the crucible and rapid evaporation of SiO(g) the overall nitridation of the coarse samples are very low compared to samples with much smaller grains. Especially the α-Si_3N_4 yield is extremely low, but as expected of a larger grain.

Storage of a sample with fine (<75 µm) grains and very low impurity levels (<20 ppm of Fe, Al, Ca etc) under humid condition retarded the nitridation process significantly. The thickening of the silica layer and no impurity elements to speed up the removal of this protective layer is regarded as the reason to this retardation.

The role of iron as a catalyst in VLS and removal of silica has been confirmed. Aluminium have contributed to oxidize to alumina in order to prevent reestablishing the protective silica layer. The role of calcium remains unconcluded as it's supposed promotion of α-Si_3N_4 was not evident. Copper in the form of Cu_3Si is liquid above 859°C and contributes significantly to nitridation levels at lower temperatures, but causes a significant sintering effect over time.

7 Further work

To be certain of the micro-morphologies it is necessary to investigate the samples in a TEM to achieve higher resolutions since e.g. the α-Si_3N_4 whisker has a size of down to 50nm. Higher resolution of EDS would also give more credit to the results.

Contaminations of samples and reaction chambers are a problem and must be eliminated. One possible, and the easiest way, is to simply run more tests and so the error margin narrows as the average of the samples diverges.

This report did not investigate other temperature programs other than the one established by Øvregård 2013 [61]. As the active liquid phase of Cu and Fe are separated by ca 350°C it will be necessary to attune the temperature program to maximize the effects of each impurity.

As mentioned in the discussion: The flow of nitrogen might be hindered by the presence of dense wool-like whiskers and the cloud of SiO_2(s) condensed on the wall of the crucible. A better suited reaction chamber will eliminate uncertainties and make the data more representable to the industry.

References

1. Deville H, Wöhler F. On the Direct Compound Silicon Nitride. Liebigs Ann. Chem. Pharam. 1859: p. 248-250.

2. Melner H, inventor; Verfahren zür darstellung von Nitriden. Ger patent 88 999. 1896 Sept. 30.

3. Weiss L, Engelhardt T. On Nitrogen Compounds of Silicon. Z. Anorg. Chem. 1910: p. 38-104.

4. Carborundum.Co , inventor; Silicon Nitride Bonded Refractory Articles. US patent 2 618 565. 1952 Nov 18.

5. Riley F. Silicon Nitride and Related Materials. Journal of American Ceramic Society. 2000; 83(2).

6. Jennings HM. On Reactions Between Silicon and Nitrogen. Journal of Materials Science. 1983;: p. 951-967.

7. Hem E. Silicon for silicon nitride based products. Specialization Project. Trondheim: NTNU, Department of Materials Technology; 2013.

8. Atkinson A, Leatt P, Moulson A, Roberts E. A mechanism for the nitridation of silicon powder compacts. Journal of Materials Science. 1974: p. 981-984.

9. Atkinson A, Moulson AJ. Nitridation of High-Purity Silicon. Journal of the American Ceramic Society. 1976;: p. 285-289.

10. Arundale P, Moulson A. Journal of Material Science. 1977: p. 2138.

11. Boyer SM, Moulson AJ. A Mechanism for the Nitridation of Fe-Contaminated Silicon. Journal of Materials Science 13. 1978;: p. 1637-1646.

12. Longland P, Moulson AJ. The growth of alpha- and beta-Si3N4 accompanying the nitriding of silicon powder compacts. Journal of Materials Science 13. 1978;: p. 2279-2280.

13. Moulson AJ. Review Reaction-bonded silicon nitride: its formation and properties. Journal of Materials Science 14. 1979;: p. 1017-1051.

14. Science Wo. Web of Knowledge. [Online].; 2013 [cited 2013 11 22. Available from: http://apps.webofknowledge.com.

15 Leitch S. THE MATERIALS RESEARCH GROUP IN CONDENSED MATTER PHYSICS AT THE U OF S. [Online].; 2005 [cited 2013 August. Available from: http://web.archive.org/web/20060715073014/http://beamteam.usask.ca/alumni.php?m=sam.

16 Pavarajan V. Roles of gas and solid components in the direct nitridation of silicon. ; 2002.

17 duBoulay D, Ishizawa N, Atake T, Streltsov V, Furuya K, Munakata F. Synchrotron X-ray and ab initio studies of beta-Si3N4. Acta Cryst. 2004: p. 388-405.

18 Hardie D, Jack KH. Crystal Structures of Silicon. Nature 180. 1957;: p. 332-333.

19 Winter M. WebElements Periodic Table of the Elements. [Online].; 2014 [cited 2014 June 25. Available from: http://www.webelements.com/silicon/.

20 Carlson ON. The N-Si (Nitrogen-Silicon) System. ; 1990.

21 Hampshire S. Silicon nitride ceramics - review of structure, processing and properties. Jurnal of Achivements in Materials and Manufactoring Engineering. 2007;: p. 43-50.

22 Kijima K, Shirasaki S. Nitrogen Self-diffusion in Silicon Nitride. Journal of Chemical Physics Volume 65. 1976;: p. 2668-2671.

23 Jennings H, Richman M. Structure, formation mechanisms and kinetics of reaction-bonded silicon nitride. Journal of Materials Science. 1976: p. 2087-2098.

24 Krämer M, Hoffmann MJ, Petzow G. Grain Growth of Si3N4 during alpha/beta-transformation. Acta metall. mater. vol 41. 1993;: p. 2939-2947.

25 Krämer M, Wittmüss D, Küppers H, Hoffmann MJ, Petzow G. Relations Between Crystal Structure and Growth Morphology of beta-Si3N4. Journal of Crystal Growth 140. 1994;: p. 157-166.

26 Hojo J, Shoji T, Kato A. Denki Kagaku Oyobi Kogyo Butsuri Kagaku; 1975.

27 Myhre B. Kinetics of the Nitridation of Silicon. Trondheim:; 1989.

28 Messier DR, Riley FL, Brook RJ. The α/β Silicon Nitride Phase Transformation. Journal of Materials Science. 1978;: p. 1199.

29 Grün R. The Crystal Structure of beta-Si3N4; Structural and Stability Considerations

. between alpha-Si3N4 and beta Si3N4. Acta Crystallogr. 1978;: p. 800-804.

30 Kijima K. Effect of iron on nitridating rate of silicon. Ceram. Trans. 1996: p. 149-168.
.

31 Huang J, Huang Z, Yi S, Liu Y, Fang M, Zhang S. Fe-catalyzed growth of one-
. dimensional α-Si3N4 nanostructures and their cathodoluminescence properties. Scientific Reports. 2013 December: p. 1-9.

32 Nie T, Chen Z, Wu Y, Guo Y, Zhang J, Fan Y, et al. Fabrication of crystal alpha-
. Si3N4/Si-SiOx core-shell/Au-SiOx peapod-like axial double heterostructures for optoelectronic applications. IOP Nanotechnology. 2012 July: p. 1-9.

33 Shaw N. The combined effects of Fe and H2 on the nitridation of silicon. Journal of
. Materials Science Letters. 1982: p. 337-340.

34 Evans A, Sharp J. In Thomas G, Fulrath R, Fisher R, editors. Electron Microscopy and
. Structure of Materials. Los Angeles: University of California Press; 1972. p. 1141.

35 Jennings H, Dalgleish B, Pratt , PL. Reactions between silicon and nitrogen. Journal of
. Materials Science. 1988: p. 2573-2583.

36 Wiik K. Kinetics of Reactions Between Silica and Carbon. PhD Thesis. Trondheim: NTH,
. Institutt for Uorganisk Kjemi; 1990. Report No.: ISBN 82-7119-170-5.

37 Heaney P. Structure and Chemestry if the low-pressure Silica Polymorphs. Reviews in
. Mineralogy. 1994; 29.

38 Sosman R. The Phases of Silica New Brunswick, New Jersy: Rutgers University Press;
. 1965.

39 Kunz K, Sarin V, Davis R, Bryan S. Self-diffusion of Silicon-30 and Nitrogen-15 in alpha
. Silicon Nitride. Materials Science and Engineering. 1988: p. 47-54.

40 Voronkov V, Falster R. Nitrogen Diffusion in Silicon: A Multi-Species Process. The
. Electrochemical Society. 2006: p. 113-126.

41 Newman R. Oxygen diffusion and precipitation in Czochralski silicon. Journal of Physics:
. Condensed Matter. 2000 Januar: p. 335-365.

42 Yatsurugi Y, Akiyama N, Edo Y, Nozaki T. Concentration, Solubility, and Equilibrium
. Distribution Coefficient of Nitrogen and Oxygen in Semiconductor Silicon. J. Electrochem. Soc. 1973 July: p. 975-979.

43 Kaiser W, Thurmond C. Nitrogen in Silicon. J. Appl. Phys. 1959 August.
.

44 Nymark A. Trondheim:; 2012.
.

45 Rahman MN, Moulson AJ. The Removal of Surface silica and its Effect on the Nitridation
. of High-Purity Silicon. Journal of Materials Sience. 1984;: p. 189-194.

46 Singhal S. Thermodynamic analysis of the high-temperature stability of silicon nitride and
. silicon carbide. Ceramurgia International. 1976: p. 123-130.

47 Blegen K. In Popper P, editor. Special Ceramics 6. Stoke-on-Trent: British Ceramic
. Research Association; 1976. p. 223.

48 Giridhar R, Rose K. Conditions for Thermal Nitridation of Si in N2-O2 Mixtures. J.
. Electrochem. Soc.: SOLID-STATE SCIENCE AND TECHNOLOGY. 1988 November: p. 2803-2807.

49 Du H, Tressler R, Spear K. Thermodynamics of the Si-N-O System and Kinetic Modeling
. of Oxidation of Si3N4. J. Electrochem. Soc. 1989 November: p. 3210-3215.

50 Honig R, Kramer D. Vapor Pressure Data for the Solid and Liquid Elements. In RCA
. Review 30.; 1969. p. 285-305.

51 Pavarajarn V, Kimura S. Catalytic Effects of Metals on Direct Nitridation of Silicon. J.
. Am. Ceram. Soc. 2001: p. 1669-1674.

52 Shaw N, Zelesnik F. Thermodynamics of Silicon Nitridation: Effect of Hydrogen. Journal
. of American Ceramic Society. 1982; 65(11).

53 Kurokawa K, Yamauchi A. Classification of Oxidation Behavior of Disilicides. Solid
. State Phenomena. 2007 Sep: p. 227-232.

54 University of Montreal CCfRiT. CRCT. [Online]. [cited 2013 December 3. Available
. from: http://www.crct.polymtl.ca/fact/phase_diagram.php?file=Fe-Si.jpg&dir=SGTE.

55 Torre JP, Mocellin A. Some Effects of Al and O2 on the Nitridation of Silicon Compacts.
. Journal of Materials Science. 1976;: p. 1725-1733.

56 University of C. Ellingham Diagrams. [Online].; 2013 [cited 2014 June 25. Available
. from: http://www.doitpoms.ac.uk/tlplib/ellingham_diagrams/images/Ellingham_1.jpg.

57 Pearson J, Ende U. The thermodynamics of metal nitrides and of nitrogen in iron and
. steel. J. Iron Steel Inst. 1953: p. 52-58.

58 Wood C, Zhao H, Cheng YB. Microstructural Development of Calcium alpha-SiAlON
. Ceramics with Elongated Grains. J. Am. Ceram. Soc. 1999: p. 421-428.

59 Sufryd K, Ponweiser N, Riani P, Richter K, Cacciamani G. Experimental investigation of

. the Cu-Si phase diagram at x(Cu)>0.72. Intermetallics. 2011: p. 1479-1488.

60 Wang H, Wu T. A general lithography-free method od microscale/nanoscale fabrication . and patterning on Si and Ge surfaces. Nanoscale Research Letters. 2012: p. 1-7.

61 Øvregård H. Silicone for Silicon Nitride-Based Products. Trondheim:; 2013.
.

62 Mukerji J, Biswas S. Effect of Iron, Titanium, and Hafnium on Second-Stage Nitriding of . Silicon. J. Am. Ceram. Soc. 1981: p. 549-552.

Appendix

A Vapor pressure

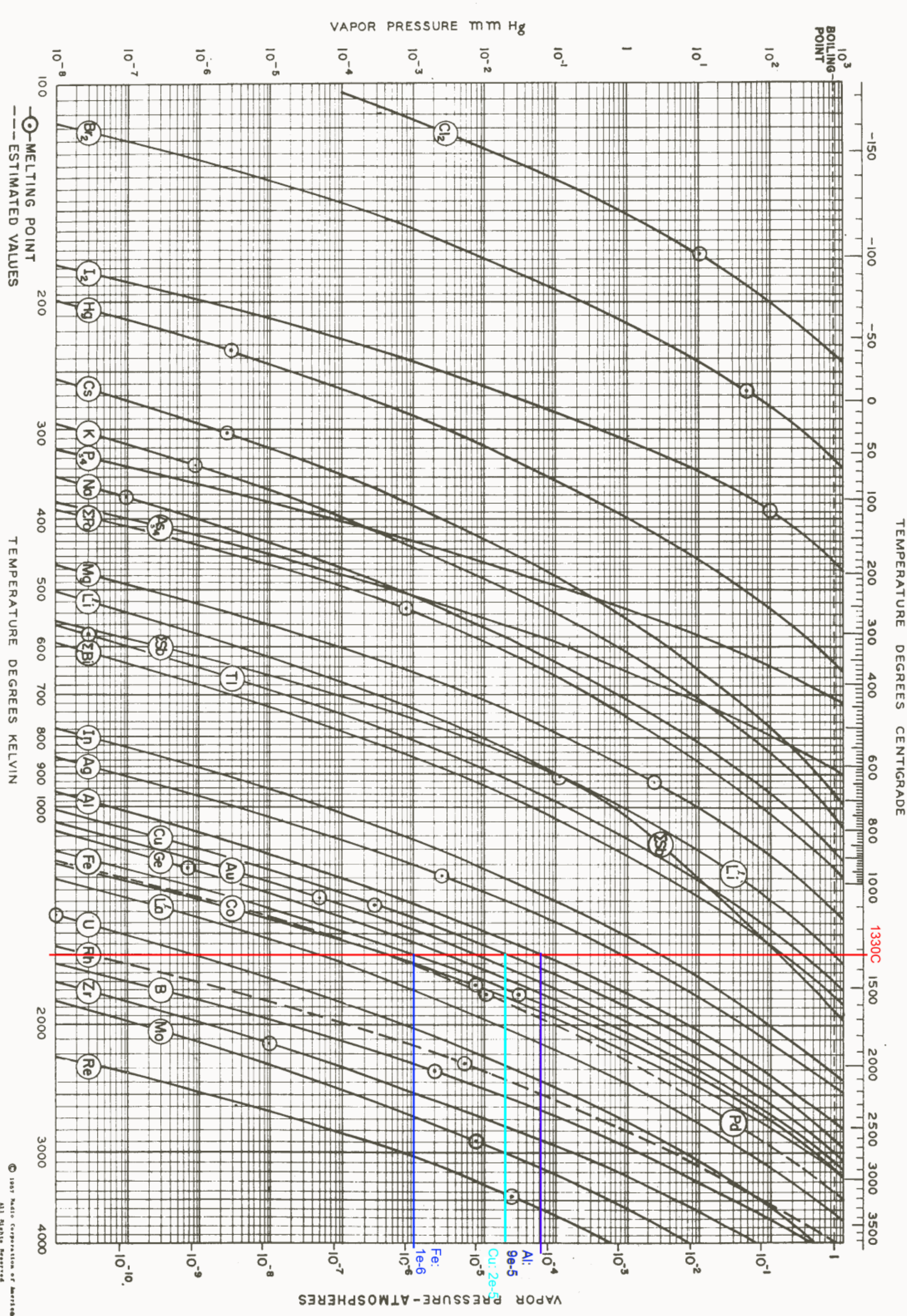

Figure A.1: Vapor pressure diagram of Fe, Cu and Al. Source: [50].

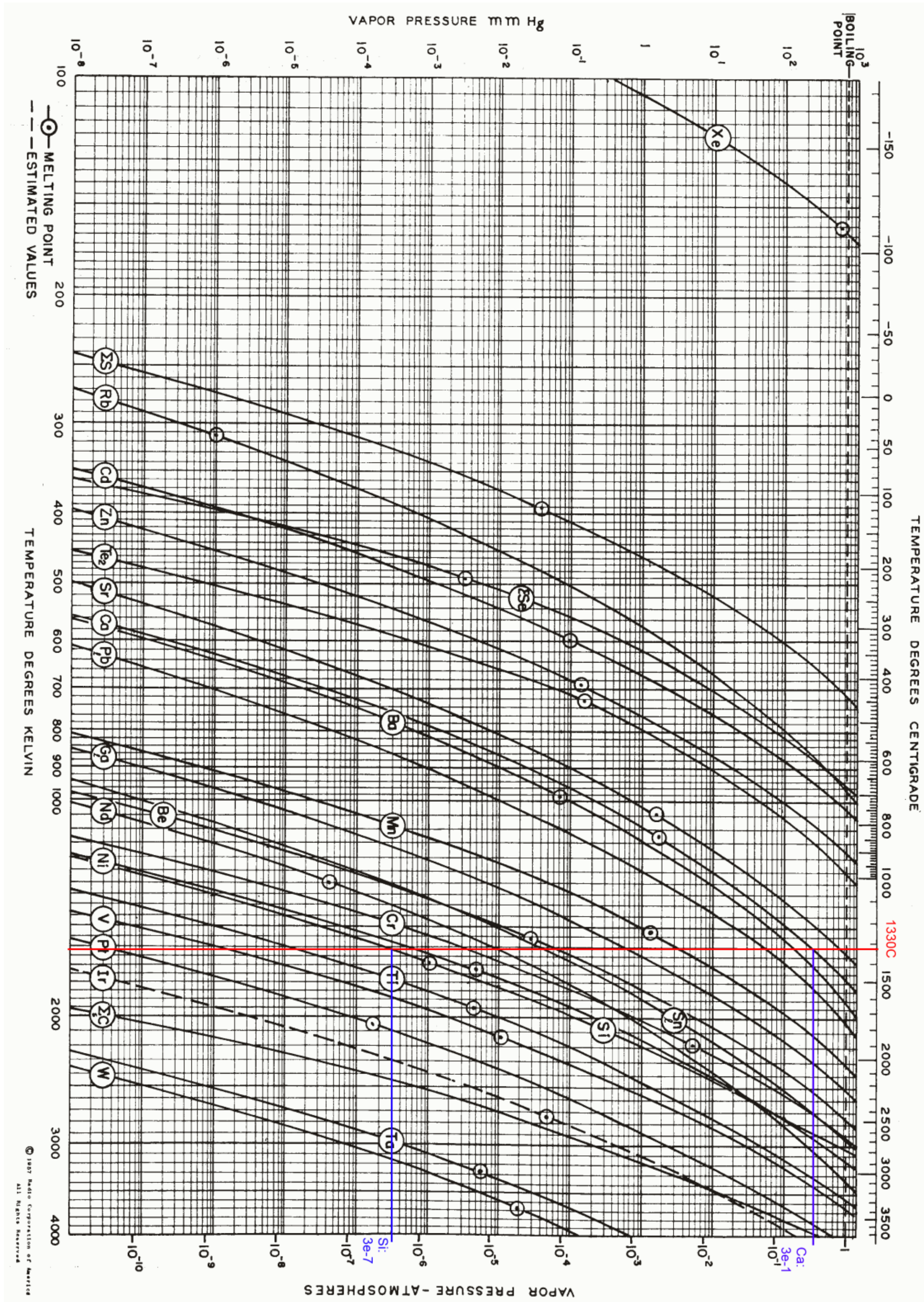

Figure A.2: Vapor pressure diagram of Si and Ca.

B Ellingham diagrams

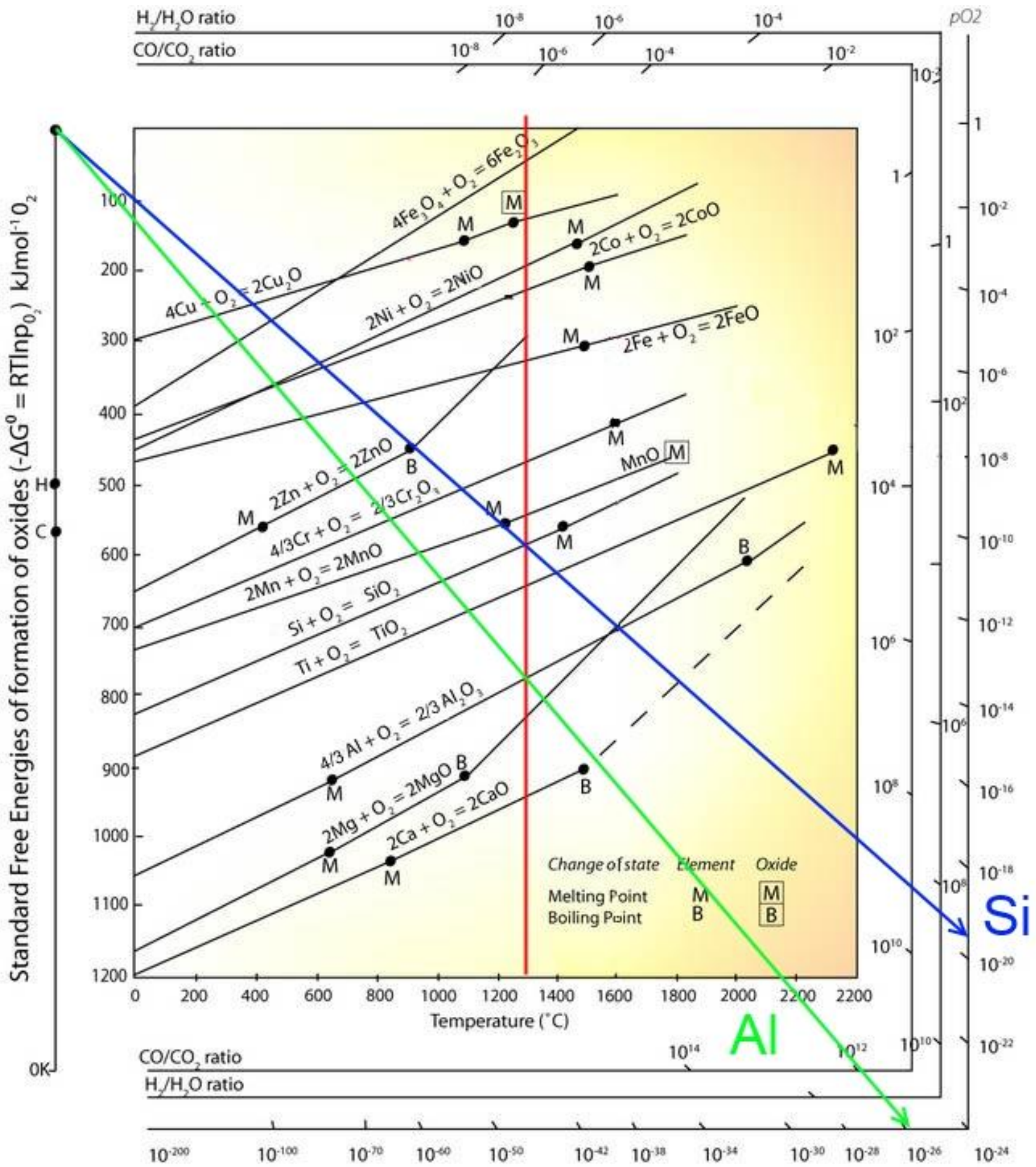

Figure B.1: Ellingham diagram showing the partial pressure of oxygen where the reaction goes to the right at 1330°C. Al_2O_3: $P_{O2}>10^{-26}$ atm and SiO_2: $P_{O2}>10^{-20}$ atm. Source: [56].

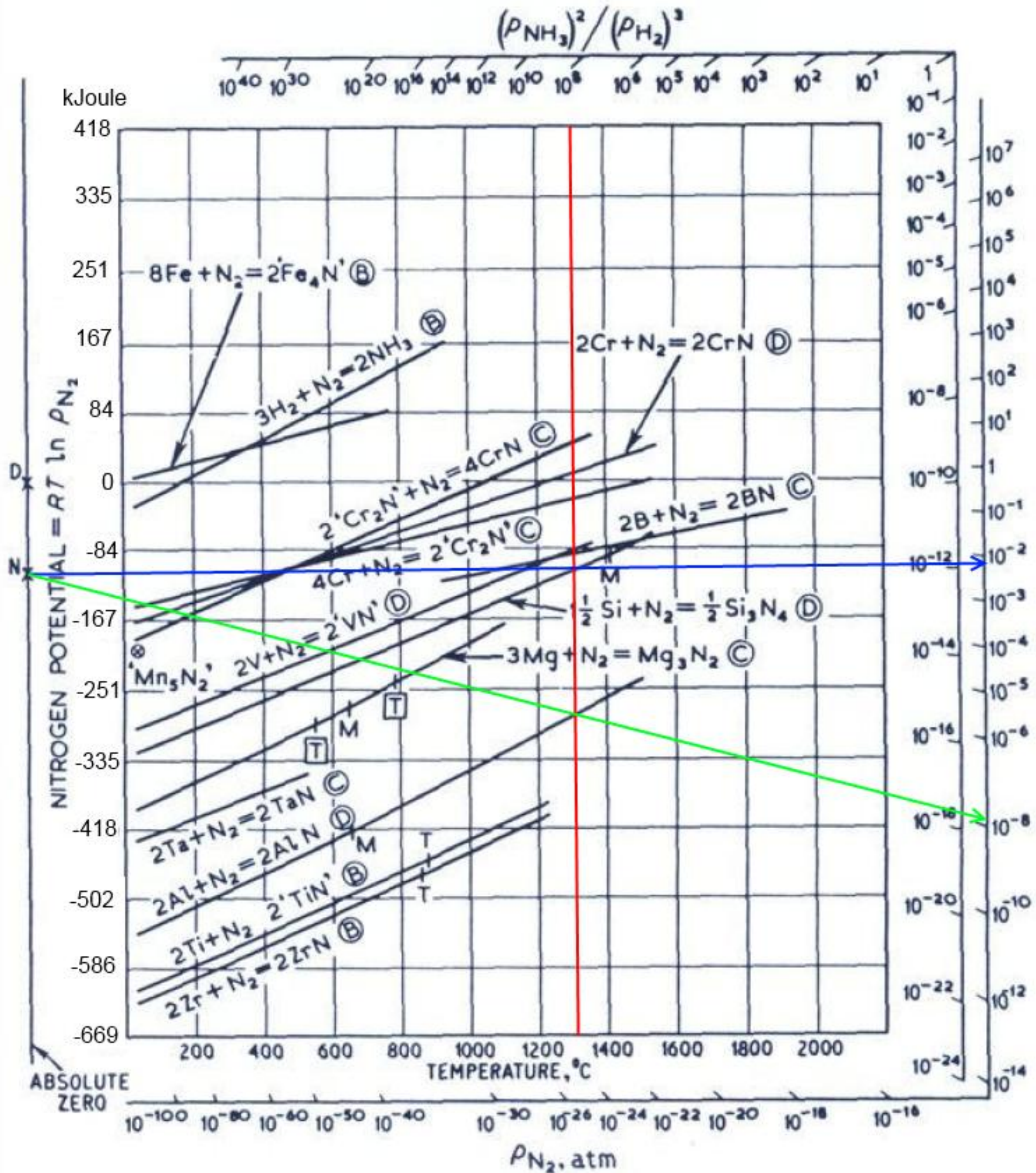

Figure B.2: Ellingham diagram showing the partial pressure of nitrogen where the reaction goes to the right at 1330°C. AlN: $P_{N2}>10^{-8}$ atm and Si_3N_4: $P_{N2}>10^{-2}$ atm. Source: [57].

C XRD plots

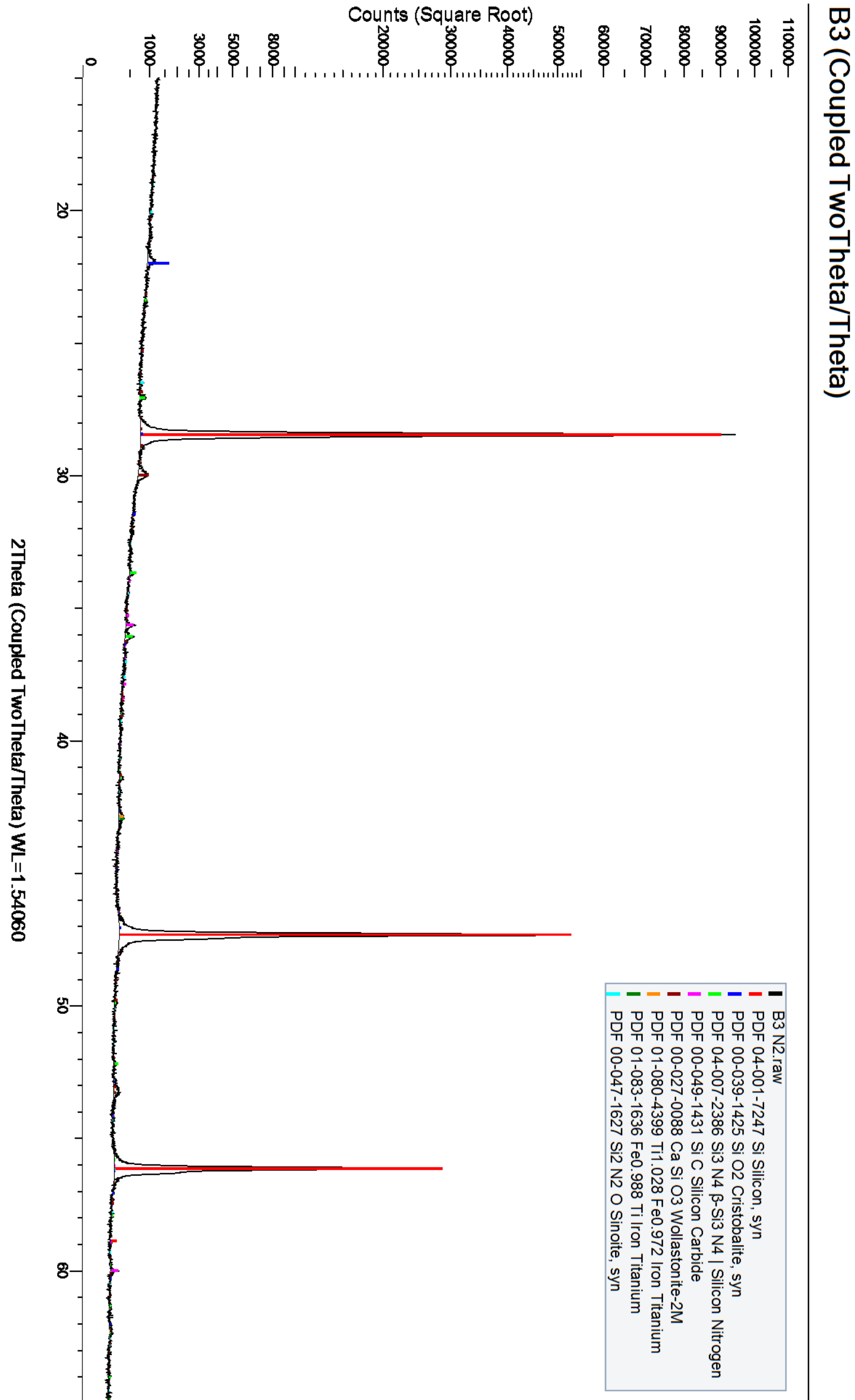

Figure C.1: XRD of sample B3 from run 1 taken with mono chromatic wave. Mark that this sample lack some of the grains from the top of the charge, which had to be used in SEM/EDS imaging. The intensity of $CaSiO_3$ was never recorded in any other sample.

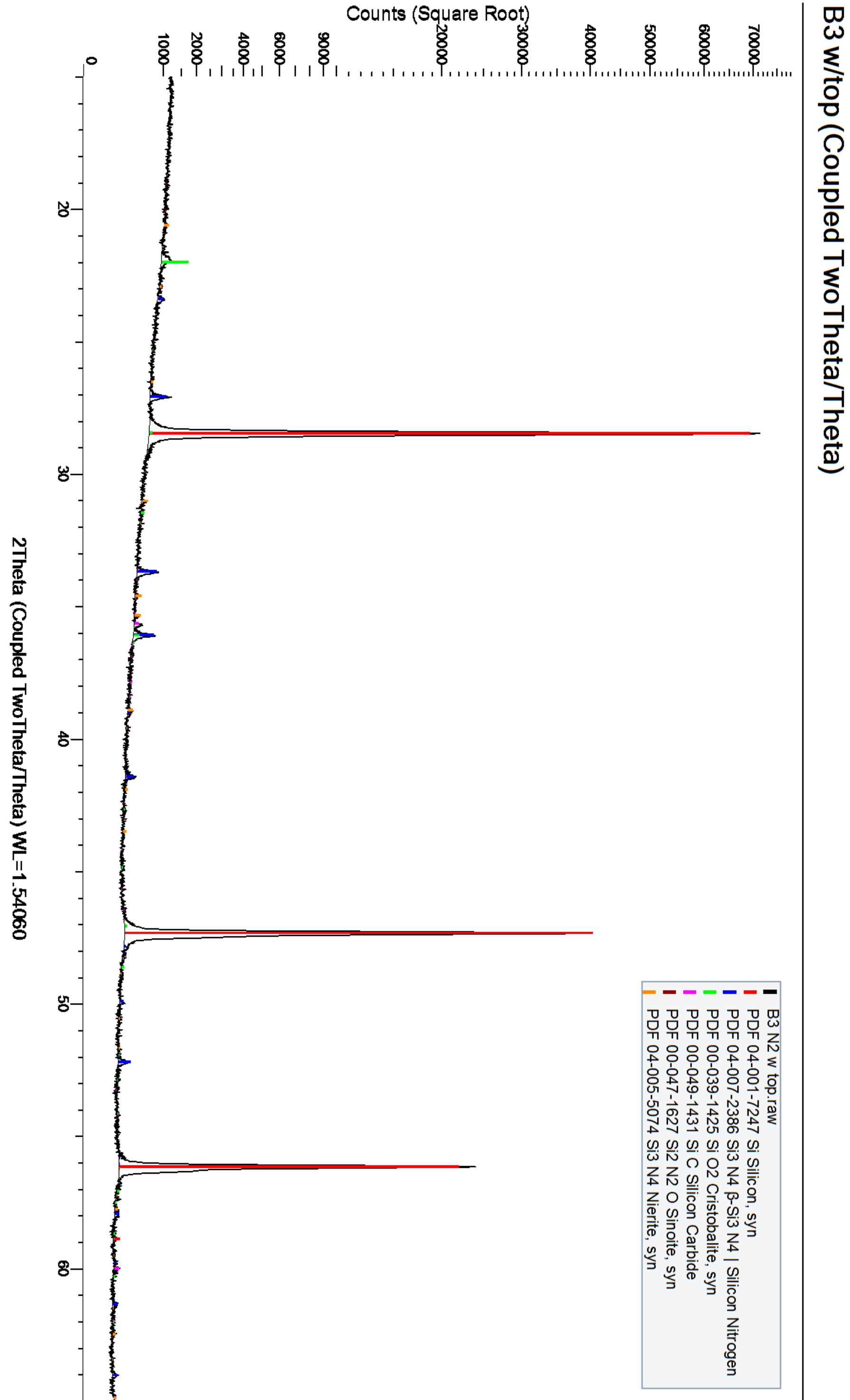

Figure C.2: XRD of sample B3 from run 2 taken with mono chromatic wave.

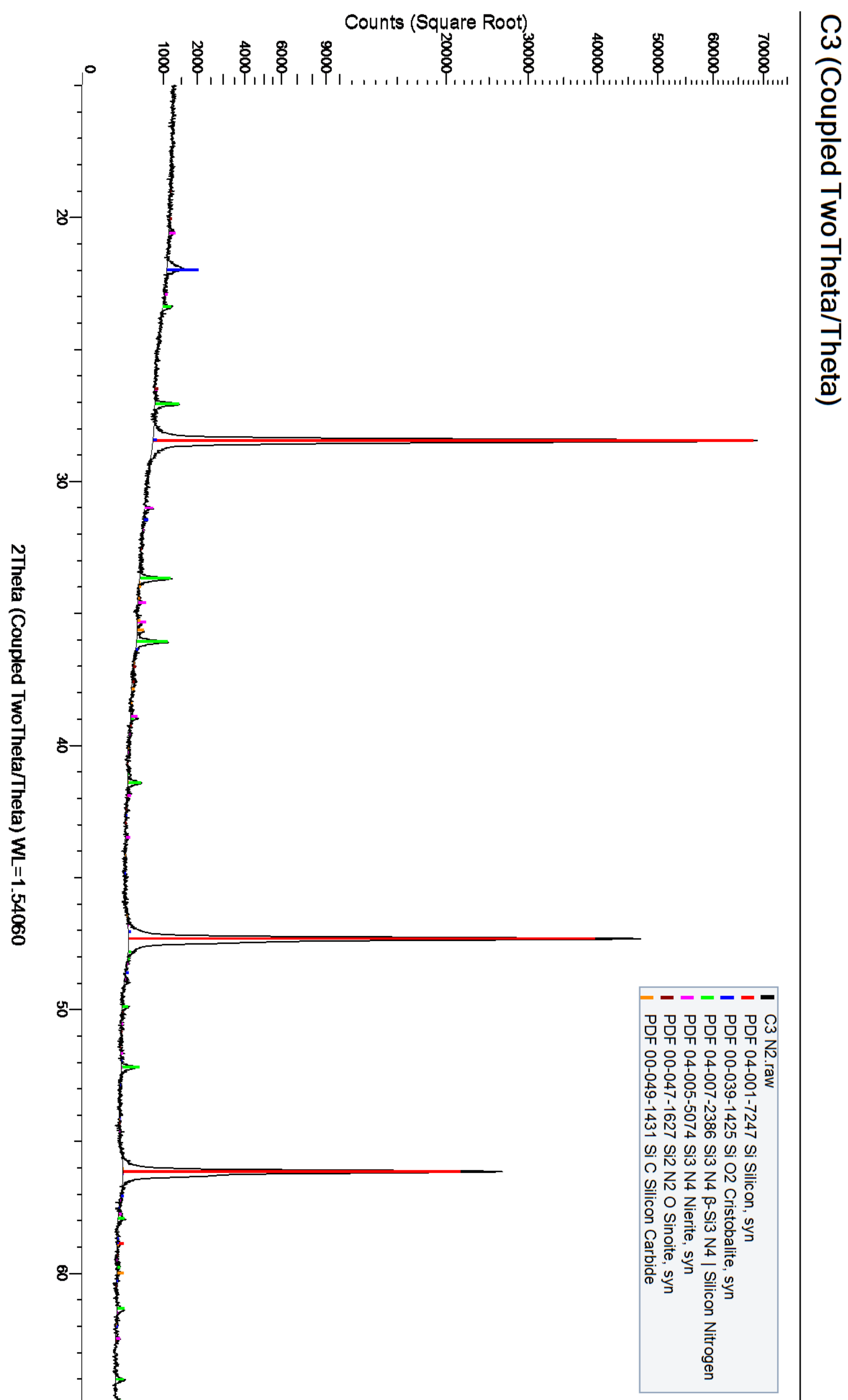

Figure C.3: XRD of sample C3 from run 2 taken with mono chromatic wave.

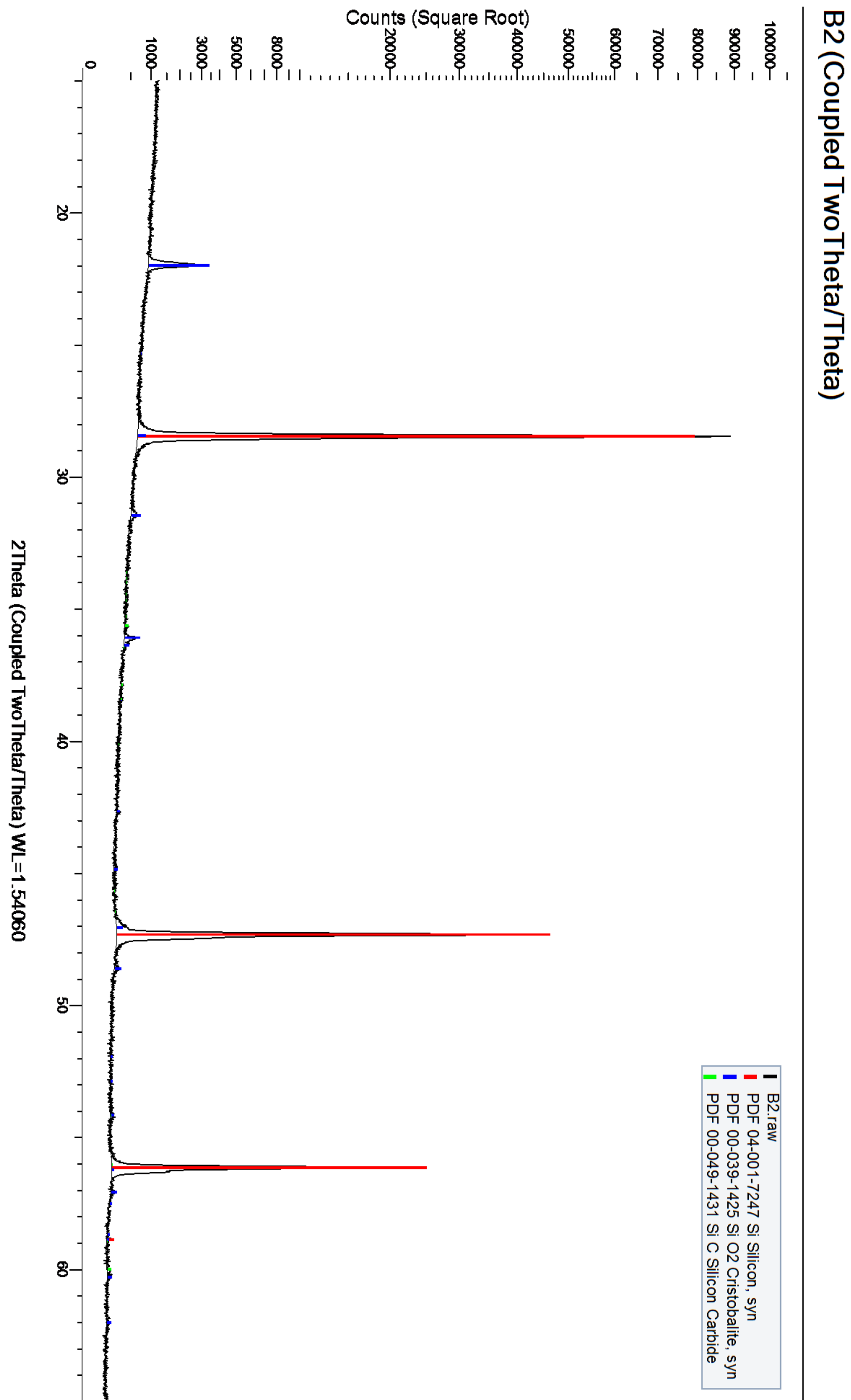

Figure C.4: XRD of sample B2 taken with mono chromatic wave.

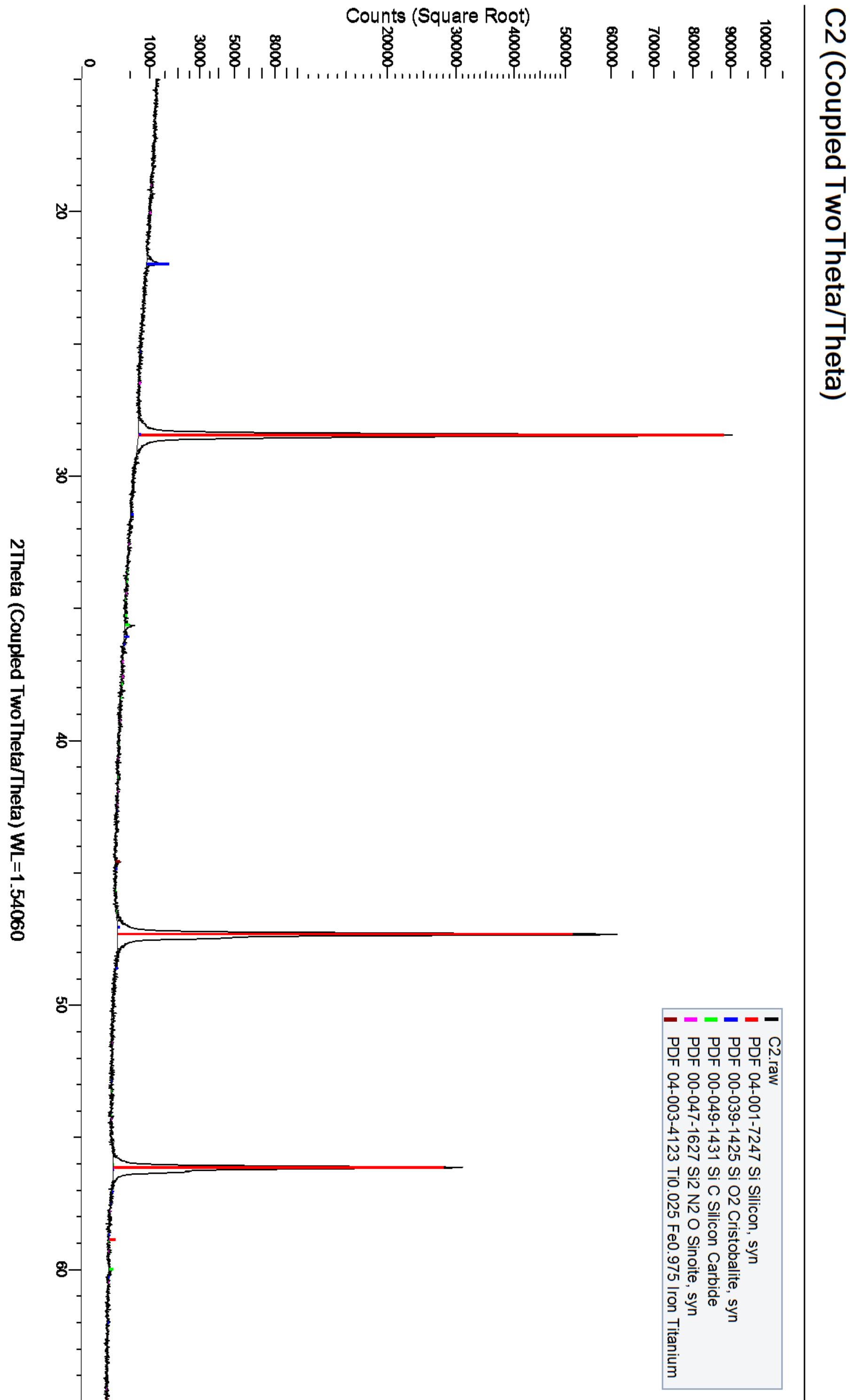

Figure C.5: XRD of sample C2 taken with mono chromatic wave.

D Exchange pure nitrogen gas flow with argon

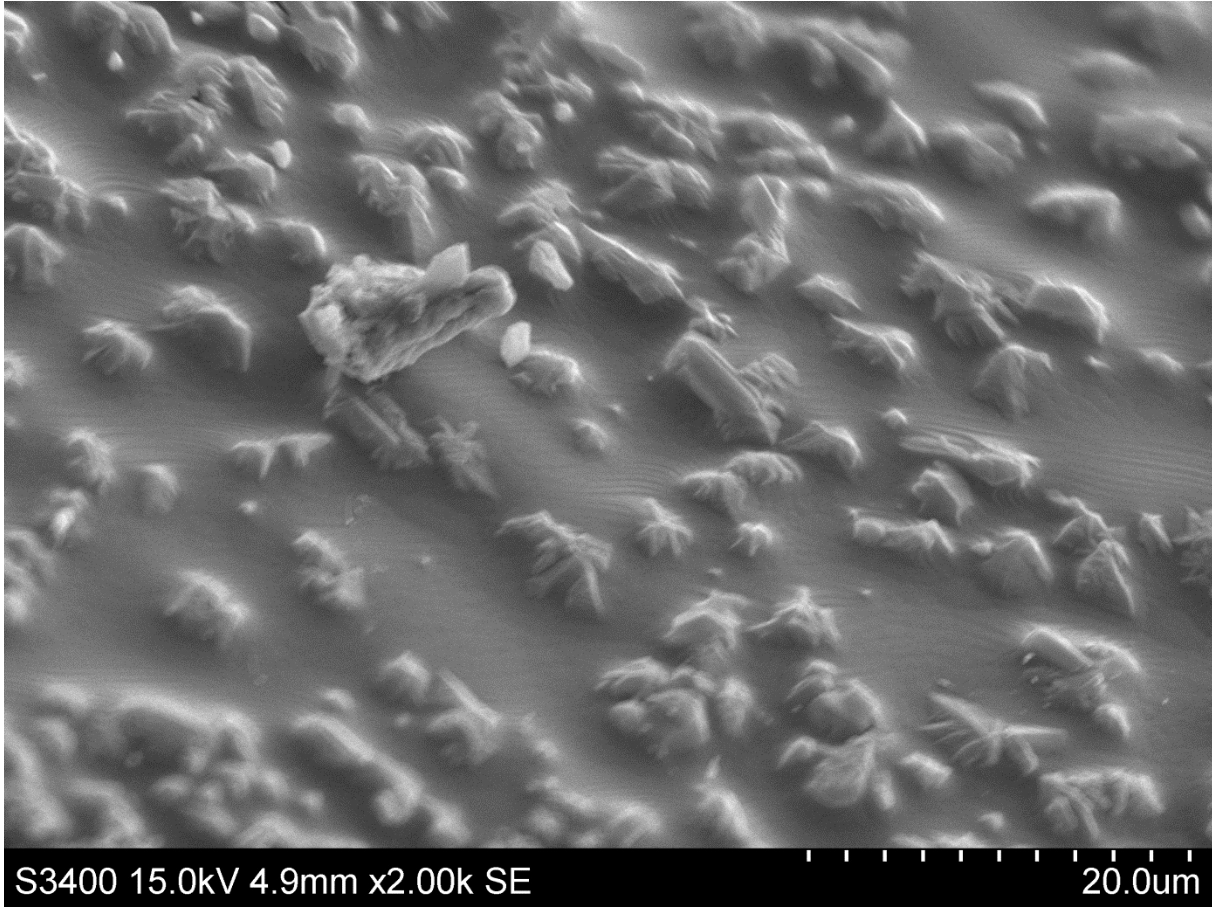

Figure D.1: Sample B3 in pure Ar atmosphere. Visible AlN crystals on a once molten surface.

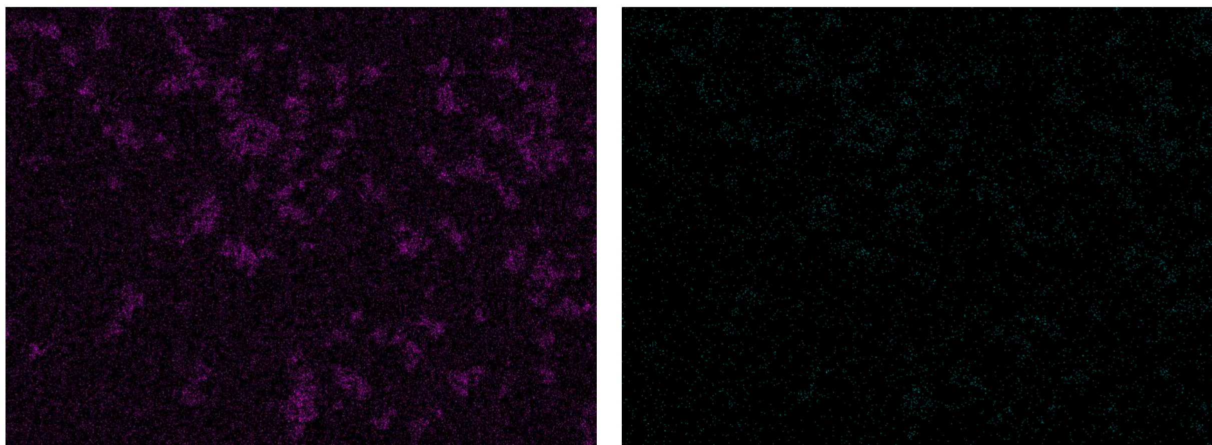

Figure D.2: EDS images of B3 Ar surface: Left) Al concentration, Right) N concentration.

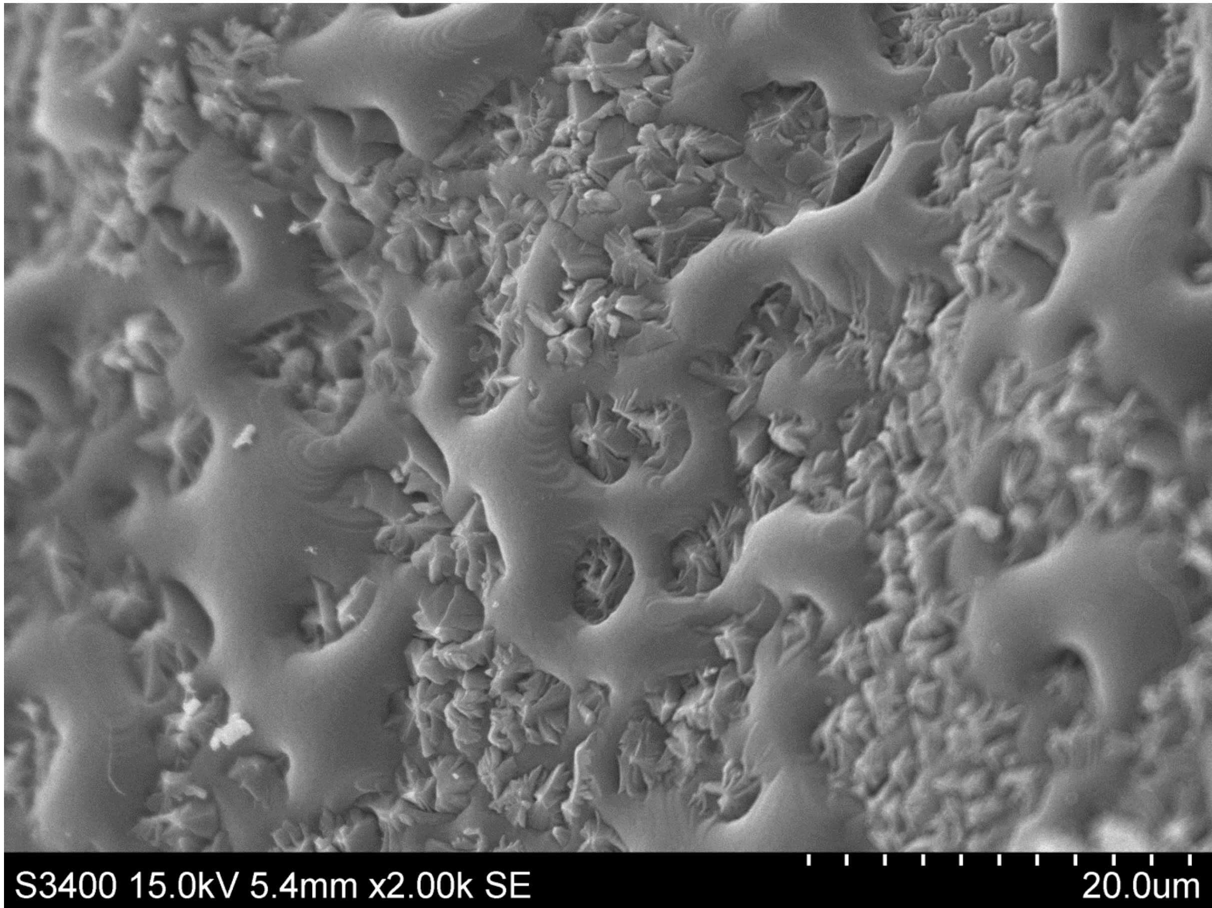

Figure D.3: Sample C3 in pure Ar atmosphere. Visible AlN crystals and solidified Si.

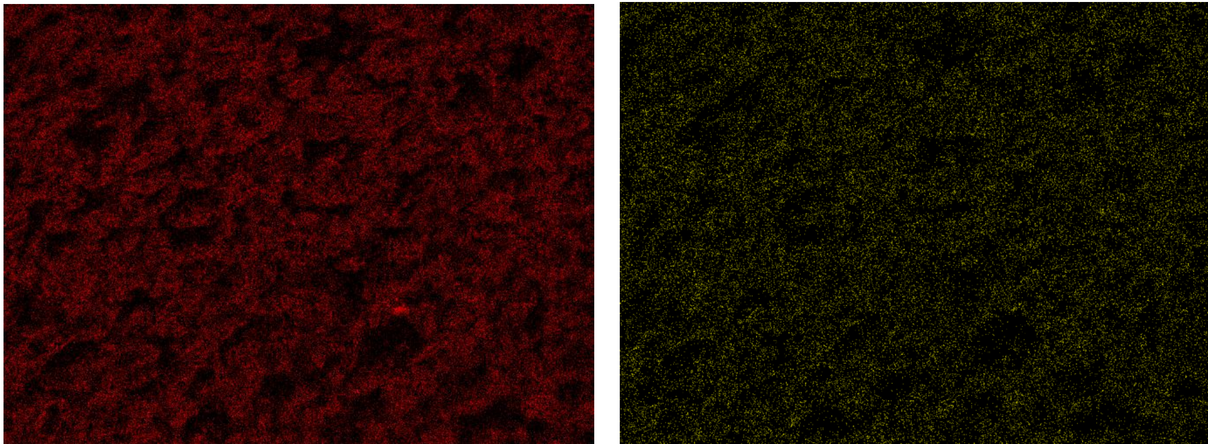

Figure D.4: EDS images of B3 Ar surface: Left) Al concentration, Right) N concentration

The grains are completely covered in the formation shown in Figure D.1 and Figure D.3. The crystals are AlN, and the non crystal surface is pure Si, with the natural nano thick layer of SiO_2. Possible nitrogen source is the argon gas flow. The EDS images are taken from different grains than the ones visible in Figure D.1 and Figure D.3.

E Additional data

All data used in this report is accessible by both links below:

http://tinyurl.com/pfqyeo9

https://www.dropbox.com/sh/4n5r0ayz72yte62/AADGmIlDGZmsKwGteaDvogZ2a